Isotope shift measurements in Ti^+ transitions using laser-ablated and thermalized ions

Messung der Isotopieverschiebung in Ti^+ Übergängen mit laser-ablatierten und thermalisierten Ionen

Zur Erlangung des Grades eines Doktors der Naturwissenschaften (Dr. rer. nat.)
Genehmigte Dissertation von Tim Ratajczyk aus Schwalmstadt
Tag der Einreichung: 13.07.2021, Tag der Prüfung: 20.10.2021

1. Gutachten: Prof. Dr. Wilfried Nörtershäuser
2. Gutachten: Prof. Dr. Joachim Enders
Darmstadt – D 17

TECHNISCHE UNIVERSITÄT DARMSTADT

Physics Department
Institut für Kernphysik
AG Nörterhäuser

Isotope shift measurements in Ti^+ transitions using laser-ablated and thermalized ions
Messung der Isotopieverschiebung in Ti^+ Übergängen mit laser-ablatierten und thermalisierten Ionen

Accepted doctoral thesis by Tim Ratajczyk

1. Review: Prof. Dr. Wilfried Nörtershäuser
2. Review: Prof. Dr. Joachim Enders

Date of submission: 13.07.2021
Date of thesis defense: 20.10.2021

Darmstadt – D 17

Erklärungen laut Promotionsordnung

§8 Abs. 1 lit. c PromO

Ich versichere hiermit, dass die elektronische Version meiner Dissertation mit der schriftlichen Version übereinstimmt.

§8 Abs. 1 lit. d PromO

Ich versichere hiermit, dass zu einem vorherigen Zeitpunkt noch keine Promotion versucht wurde. In diesem Fall sind nähere Angaben über Zeitpunkt, Hochschule, Dissertationsthema und Ergebnis dieses Versuchs mitzuteilen.

§9 Abs. 1 PromO

Ich versichere hiermit, dass die vorliegende Dissertation selbstständig und nur unter Verwendung der angegebenen Quellen verfasst wurde.

§9 Abs. 2 PromO

Die Arbeit hat bisher noch nicht zu Prüfungszwecken gedient.

Darmstadt, 13.07.2021

T. Ratajczyk

Abstract

Collinear laser spectroscopy has been used for many years to investigate atomic and nuclear properties with high precision all over the nuclear chart. It will be increasingly used at in-flight facilities like FRIB and FAIR to study short-lived isotopes of refractory metals and transition metals that have not been investigated so far due to the limited availability at ISOL facilities. In this work a versatile and compact ion source has been developed that is able to produce ions from a wide range of elements and in particular from the transition metals. It will serve for preparatory work on such ion beams and as a source for reference measurements of stable isotopes during on-line campaigns.
Ions are produced by laser ablation inside a buffer gas cell and then extracted through a compact RF-only funnel and an RF+DC buncher into high-vacuum conditions. The new ion source was tested and benchmarked at the Collinear Apparatus for Laser Spectroscopy and Applied Science (COALA) at TU Darmstadt. Its functionality has been demonstrated for calcium, titanium, iron, and copper ions, for which beams with sufficient intensity are produced. Typical average ion currents between 3 and $20\,\mathrm{pA}$ at the optical detection region were established at $100\,\mathrm{Hz}$ ablation rate. However, unexpectedly large amounts of material ejection onto the funnel electrodes limited the operation time for some materials (Ca, Fe) to a few hours, while for others (Cu, Ti) the source operated for several days.
Laser spectroscopy in the D1 transition of Ca^+ ions was used to benchmark the ion source and, a linewidth of about $60\,\mathrm{MHz}$ with an insignificant drift of the center frequency within the ion bunch duration was demonstrated, competitive with surface ion sources and outperforming other laser ablation sources. As a first application of the ion source, collinear laser spectroscopy was performed on three $J \rightarrow J+1$ transitions of the $3d^2(^3\mathrm{F})4s\ ^4F_J \rightarrow$

$3d^2(^3\mathrm{F})4p\ ^4G_{J'}$ fine-structure multiplett in Ti^+ ions for all five stable isotopes. Isotope shifts were extracted with precision between 1 and $2\,\mathrm{MHz}$. Those are required to model lineshapes in astronomical investigations of absorption lines in quasar spectra to search for variations of the fine-structure constant in early times of our universe. Measurements of the hyperfine structure of the stable odd-isotopes proved that the $J = {}^3/_2 \rightarrow J' = {}^5/_2$ transition is the best choice for on-line collinear laser spectroscopy measurements planned at FRIB, since all hyperfine lines are separated. Finally, the mass-shift factor and the field shift factor were extracted, which are crucial for the extraction of nuclear charge radii from online measurements of short lived nuclei.

Zusammenfassung

Die kollineare Laserspektroskopie wird seit Jahrzehnten eingesetzt, um atomare Spektren zu untersuchen und Kerneigenschaften insbesondere kurzlebiger Isotope zu bestimmen. Zukünftig wird die Methode verstärkt an den Anlagen zur sogenannten “in-flight Fragmentation” wie FRIB und FAIR angewendet werden. Diese erlauben das Studium der Isotope vieler Übergangsmetalle, die an konventionellen (ISOL) Anlagen kaum zur Verfügung stehen. In dieser Arbeit wurde eine vielseitige und kompakte neue Ionenquelle entwickelt, die in der Lage ist, solche Ionen für die kollineare Laserspektroskopie in guter Strahlqualität zur Verfügung zu stellen. Sie soll für vorbereitende Untersuchungen aber auch für die Spektroskopie der Referenzisotope während der Strahlzeiten zur Verfügung stehen. Die Ionen werden mittels Laserablation in einer Gaszelle erzeugt, durch einen Radiofrequenz (RF)-Funnel sowie einen (RF+DC) buncher in ein Hochvakuum extrahiert. Die Ionenquelle wurde an der kollinearen Apparatur für Laserspektroskopie und angewandte Physik (KOALA) an der TU Darmstadt getestet und spezifiziert. Ihre Funktionalität wurde durch die Erzeugung von Ionenstrahlen der Elemente Kalzium, Titan, Eisen und Kupfer mit ausreichender Intensität für die kollineare Laserspektroskopie demonstriert. Typische mittlere Ströme von 3-20 pA an der optsichen Nachweisstrecke wurden bei einer Ablationsrate von 100 Hz erzeugt. Allerdings begrenzten unerwartet starke Materialablagerungen an den Funnel-Elektroden die Einsatzdauer für einige Materialien (Ca, Fe) auf wenige Stunden, während die Quelle mit anderen Elementen (Cu, Ti) über mehrere Tage betrieben werden konnte.
Die Spezifikation der Ionenquelle erfolgte mittels Laserspektroskopie auf dem D1 Übergang in Ca^+ Ionen, wobei eine Linienbreite von etwa $60\,\mathrm{MHz}$ (FWHM) und eine vernachlässig-

bare Drift der Zentralfrequenz über den Verlauf des Ionenpulses beobachtet wurde. Dies ist vergleichbar mit Linienbreiten aus Oberflächenionenquellen und eine deutliche Verbesserung gegenüber anderen Ablationsquellen, die bislang zur kollinearen Spektroskopie eingesetzt wurden. Als erste Anwendung wurde die neue Ionenquelle zur kollinearen Laserspektroskopie von drei $J \to J+1$ Übergängen des $3d^2(^3\mathrm{F})4s\ ^4F_J \to 3d^2(^3\mathrm{F})4p\ ^4G_{J'}$ Feintrukturmultipletts in Ti^+ Ionen eingesetzt und alle fünf stabilen Isotope gemessen. Die Isotopieverschiebungen wurden erstmals und mit einer Unsicherheit zwischen 1 und $2\,\mathrm{MHz}$ bestimmt. Die erhaltenen Informationen können zur Modellierung der Linienformen in astronomischen Beobachtungen eingesetzt werden, bei denen man in den Absorptionsspektren der Quasare nach Veränderungen der Feinstrukturkonstante während des frühen Universums sucht. Weiterhin konnte durch die Messung der Hyperfeinstruktur der beiden ungeraden stabilen Titanisotope, der $J = {}^3/_2 \to J = {}^5/_2$ Übergang als beste Wahl für die geplanten Messungen mit kollinearer Laserspektroskopie an FRIB bestimmt werden, da hier alle Hyperfeinlinien aufgelöst werden. Schlussendlich konnten aus den gemessenen Isotopieverschiebungen noch die atomaren Faktoren des Masseneffektes und des Volumeneffektes bestimmt werden, die entscheidend für die Bestimmung der Ladungsradien kurzlebiger Isotope sind.

Contents

1 Introduction

Recently the international system of units (SI) has been revised [1]. The new definition relies only on fundamental physical constants. This should allow to reproduce the units anywhere in the universe by referring to those constants. Atomic transition frequencies are used for the definition of time and can also serve as reference standards for measurements of other observables. There is, for example, a long standing suggestion to use the Doppler shift of atomic transition frequencies for high-voltage measurements [2]. For low voltages, Josephson junctions [3] are using microwave frequencies referenced to a frequency standard to provide a voltage value that relies only on the fundamental constants K_J, the electric charge e and the Planck constant h, but for high voltages ($>1000\,\mathrm{V}$) divider chains of accurate resistors have to be used. Recently, the collinear laser spectroscopy approach, referencing the high voltage to an atomic transition frequency, has been considerably improved [4].

Relying our unit system to fundamental constants requires those to be constant with time. There are, however, different theories that are discussed as extensions of the standard model questioning this assumption. Experiments on a variety of fields are searching for a possible change of our fundamental constants [5]. Dimensionless constants like the fine-structure constant α are particularly interesting in this respect, and a change in α would directly influence atomic transitions. This can be tested by investigating if the fine-structure splitting of an atomic line varies over time as it is directly proportional to α^2 [6]. To have the possibility to study this on larger timescales than a few decades on earth, the high luminosity of quasars can be used to measure light that has been emitted up to

12.9 billion years ago, only about 770 million years after our universe came into being by the the big bang [7].

Observations of the light emitted by quasars show a strong line broadening due to the high velocities and heat of the matter that circles around the black hole in the center of the quasar. To improve the linewidth, the absorption lines of intervening cold clouds of gas along the line of sight are used for analysis rather than the intrinsic emission lines [8]. To further improve this technique, a multitude of lines with different dependencies on α are combined to improve the sensitivity to the α-variation as explained in more detail in [9], [10].

A crucial part to reduce the uncertainties for these measurements is a precise knowledge of transition frequencies from laboratory measurements on earth. Isotope shifts are also important quantities as the distribution of the isotopic lines defines the shape of the observed absorption line from the quasar light and allows even to compare the isotopic abundance in the universe billions of years ago to the abundance we find here on earth [11]. According to [11], some specific transition frequencies and isotope shifts of the atoms and ions of C, O, Na, Mg, Al, Si, S, Ca, Ti, Cr, Mn, Fe, Ni, Zn, and Ge need to be measured to an accuracy of better than 10^{-4} Å, which ranges between 8 and $300\,\mathrm{MHz}$ depending on the transition.

Collinear laser spectroscopy has proven to be a versatile tool over a broad range of stable and short lived isotopes along the nuclear chart [12] providing accuracies better than $200\,\mathrm{kHz}$ [13]. High resolution is provided by the velocity compression during electrostatic acceleration [14] and it allows for the investigation of positive and negative ions as well as atoms. While collinear laser spectroscopy provides more than sufficient accuracy to provide references for the astronomical observations, the versatility of a collinear apparatus is usually limited by the available ion sources. These devices are often equipped with surface ion sources providing ions of alkaline and earth alkaline elements as well as a few other species. At the BECOLA facility of the National Superconducting Cyclotron Laboratory (NSCL) located at the Michigan State University (MSU) a Penning ion source is used to deliver ions of transition metals [15]. Even more versatile is an ion source based on laser ablation. Laser ablation describes processes were a laser pulse hits the

surface of a target and some of its material is released by vaporization. This is performed with different purposes from machining to material analysis. The latter is based on the fact that laser ablation is able to vaporize any constituent of the given target. This is used e.g. in matrix-assisted laser desorption and ionisation (MALDI) time-of-flight mass spectrometry. A technique for which Koichi Tanaka received a Nobel prize in chemistry in 2002 [16], [17]. This technique shows already that not only single ions can be produced but also molecular ions. Another established technique is the inductively-coupled-plasma mass-spectrometry with laser ablation (LA-ICP-MS) which can be applied to any material without restrictions to ionization potential [18]. This advantage makes laser ablation a versatile tool as an ion source for laser spectroscopy. This technique is already in use, often to feed ions into a quadrupole cooler and buncher or a trap [19]–[23]. Sometimes it is used with direct laser ablation inside a vacuum chamber which causes broad spectra [24] or needs to be compensated by fast detection electronics [25]. One goal of this work was to develop a versatile laser ablation based ion source that can deliver a cooled ion beam with a comparable energy spread to an RFQ-cooler and buncher at online facilities like ISCOOL [26] or the LEBIT cooler [27]. To achieve this goal, the laser ablation is taking place in a buffer gas, as also performed in [28], and extracted by an RF-funnel electrode system [29]–[32] which was first combined with an RF-only funnel in [33]. In addition to this version, an additional buncher section is implemented to further improve the extraction of the ions and may allow accumulation of the ions [34] similar to the mentioned RFQ-cooler and buncher. Such an ion source can provide a large variety of elements for high-precision laser spectroscopy to measure isotope shifts required for astronomical observations and provide precise reference values for online measurements of nuclear properties [12].

In this thesis, the design and commissioning of a new ion source based on laser ablation in a buffer gas is described. It allows the generation of ion beams required to study most of the elements for the above described astronomical studies with collinear laser spectroscopy. First commissioning measurements are performed on Ti^+. Here, three transitions from the $3d^2(^3\mathrm{F})4s\,^4F$ ground state to the $3d^2(^3\mathrm{F})4p\,^4G$ excited state were investigated. Titanium $(Z = 22)$ was chosen since it is not only relevant to reference the quasar absorption observations, but is also an interesting element for nuclear structure studies. The five stable isotopes $^{46-50}$Ti are located between the magic neutron numbers

$N = 20$ and $N = 28$, which have drawn a lot of attention recently. At $N = 28$, a strong shell closure indication in form of a kink in the trend of the nuclear charge radii has been observed [35]–[38]. Contrarily, at $N = 20$ only a weak kink was found [39]–[43]. The discussion of these different features is still ongoing. The weaker kink structure might be a residual effect from different monopole core polarizations of the protons for valence neutrons in the sd or $f_{7/2}$ shell [39], [44]. The weak kink structure has been observed in Ar, K, and Ca, which all have their valence protons in the sd shell. Therefore, it is of great interest to study this phenomenon for elements with $Z > 20$ such as Sc and Ti. Ti will be the ideal candidate since its five stable isotopes enable to deduce the mass- and field-shift parameters from a King-Plot [45], which will allow one to determine the charge radii of the short-lived isotopes from isotope shift measurements. So far, collinear laser spectroscopy in Ti was only performed with dye lasers on atoms [46] and ions [47]. In this work, the transitions investigated can be accessed with Titanium:Sapphire lasers, which are preferred in online measurements since they require less maintenance. These transitions are evaluated in terms of suitability for online spectroscopy measurements and the mass- and field shift parameters are deduced. This will pave the way towards online experiments on neutron-deficient Ti to investigate the $N = 20$ shell closure but also for measurements on neutron-rich isotopes. There, evidence for new shell closures at $N = 32$ and $N = 34$ was observed [48], [49] but so far not confirmed by charge radius measurements via collinear laser spectroscopy in Ca and K [36], [50]. Again, measurements in Ti with $Z > 20$ are required to complete the picture.

2 Theory

2.1 Collinear laser spectroscopy

Since its invention in the late 1970s [14], [51], collinear laser spectroscopy has been used in many facilities worldwide to measure nuclear properties (spin, charge radius, magnetic dipole moment, electric quadrupole moment) of stable, and, even more important, short-lived nuclei [12], [52], [53]. The in-flight measurements on fast beams (10-$60\,\mathrm{keV}$) enable spectroscopy on isotopes with a half-life down to a few ms, which cannot be accessed with other techniques that require time-intense cooling procedures. The achievable accuracy of 100 kHz for transition frequencies of several 100 THz [13], [54] make this technique also interesting for metrology applications, e.g., the measurement of high-voltages [2], [4], [55].

2.1.1 Relativistic Doppler shift

According to the principle of special relativity [56] the frequency ν, seen by an observer moving relative towards a light emitter with velocity v under an angle α with respect to the line of sight is shifted to

$$\nu' = \nu \frac{1 + \cos(\alpha)\frac{v}{c}}{\sqrt{1 - \left(\frac{v}{c}\right)^2}}. \tag{2.1}$$

With c being the speed of light, defining

$$\beta = \frac{v}{c} \tag{2.2}$$

and

$$\gamma = \frac{1}{\sqrt{1-\beta^2}}, \tag{2.3}$$

the equation for the frequency seen from the observer can be written as

$$\nu' = \nu\gamma(1 + \beta\cos(\alpha)) \tag{2.4}$$

This equation holds without having an absolute reference frame, but only the relative velocities between the emitter and the observer, which is in this case defined as $\alpha = 0$ as moving towards and $\alpha = \pi$ as moving apart from each other. Concerning the interaction between laser light and moving ions, ν' describes the Doppler-shifted frequency of the photon that is seen by the moving ion in its rest frame while ν is the laser frequency in the laboratory frame. A laser which is aligned collinearly with the ion beam finds the ions moving away from the light source and, hence, is described with the angle $\alpha = \pi$ and the anticollinear configuration with the angle $\alpha = 0$.

2.1.2 Doppler compression

Measuring atomic transitions with high accuracy is limited by the thermal velocity distribution of the ion ensemble, which leads to a broadening of the absortion and emission lines. This is due to the relativistic Doppler shift described in 2.1.1, which depends on the individual velocity of each atom in the ensemble. The effect is known as Doppler broadening, which can be strong enough to prevent resolving hyperfine effects. The FWHM of the Doppler broadening is given by [57]

$$\delta\nu_D = \frac{2\nu_0}{c}\sqrt{\frac{2RT\ln 2}{M}}, \tag{2.5}$$

with the temperature T, the universal gas constant R, the molar mass M, and the transition frequency ν_0. This yields for the $3d^2(^3\mathrm{F})4s\ ^4F_{3/2} \rightarrow 3d^2(^3\mathrm{F})4p\ ^4G_{5/2}$ transition ($338.4\,\mathrm{nm}$)in Ti^+ and a temperature of 300 K of the ion ensemble a Doppler width of $\delta\nu_D \approx 1.6\,\mathrm{GHz}$.

One approach to reduce this velocity spread is by cooling the ions down to low temperature in magneto-optical traps for atoms or in Paul or Penning traps for ions. Magneto-optical traps require atomic transition lines that can be used for laser cooling and the corresponding laser system which makes it a highly efficient system for special cases reaching very low temperatures [58], but makes it inflexible to investigate a huge variety of elements. Penning and Paul traps are universal and can trap all ion species and are used for spectroscopy in several institutes [59], [60] and allow long storing times of the order of month at temperatures of about $4\,\mathrm{K}$ since the system is cooled by liquid helium [20].

A more counter-intuitive way is accelerating the ions to higher velocities which was first described by Kaufman [14]. In the following, the concept of the so-called Doppler compression is introduced in the nonrelativistic approximation. Typical acceleration voltages in collinear laser spectroscopy are of the order of several $10\,\mathrm{kV}$, and the masses range from a few atomic mass units [61] up to several hundred atomic masses [62]. Hence, the velocities of the ions are orders of magnitude below the speed of light and $\beta \ll 1$ is fulfilled. For example, in case of singly charged ^{48}Ti at $14\,\mathrm{kV}$

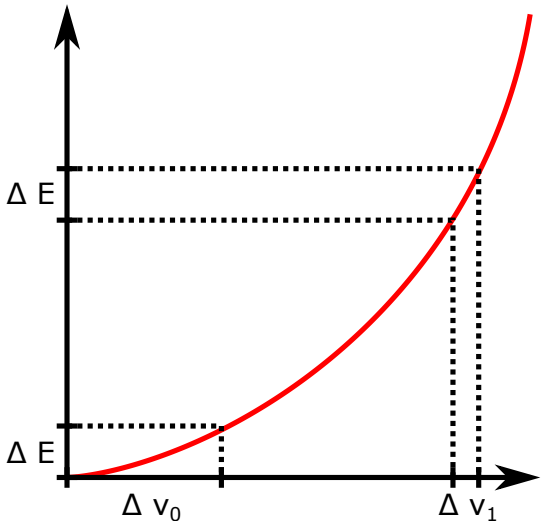

Figure 2.1: Comparison of the velocity spread Δv_0 before acceleration and Δv_1 after acceleration. The energy spread ΔE stays constant.

$$\beta = \sqrt{1 - \frac{1}{1 + \frac{Uq}{mc^2}}} = 0.00058. \tag{2.6}$$

This allows the description to be accurate enough to explain the principle, even though

the data analysis is performed fully relativistic because the precision of the measurements is of the order of 1×10^{-9} and, hence, sensitive to relativistic corrections.

In Fig. 2.1 the kinetic energy is plotted as a function of velocity according to the relation

$$E_{\text{kin}} = \frac{m}{2} v^2. \tag{2.7}$$

The velocity spread Δv_0 of the ensemble of ions corresponds to an energy spread ΔE. If this ensemble of singly charged ions is accelerated by the voltage U, its kinetic energy rises by $q \cdot U$ and, hence,

$$E'_{\text{kin}} = E_{\text{kin0}} + Uq. \tag{2.8}$$

The energy spread ΔE is not effected by this acceleration and stays constant. This is different for the velocity spread as the energy and velocity have a quadratic relation, Δv_1 decreases with higher velocities according to

$$\frac{\partial E}{\partial v} = mv \Rightarrow \Delta v \propto \frac{\Delta E}{mv} \tag{2.9}$$

After an acceleration of $14\,\text{kV}$ this broadening reduces roughly by the factor $\sqrt{E_{\text{th}}/qU}$ [63], where $E_{\text{th}} = k_B T$ is thermal energy of the ions. For the Ti transition this reduces the Doppler broadening nominally to $2.6\,\text{MHz}$ which is about one order of magnitude below the natural line width ($\approx$22 MHz) of this transition.

2.1.3 Basic setup for collinear laser spectroscopy

Collinear laser spectroscopy uses the special case of (2.4) where α is either 0 or π. This is the case if the laser beam and the ion beam are aligned either parallel (collinear direction) or antiparallel (anticollinear direction), and the relation for resonant excitation of the transition frequency ν_0 by the laser frequency ν_L reduces to

$$\nu_L = \nu_0 \gamma (1 \pm \beta). \tag{2.10}$$

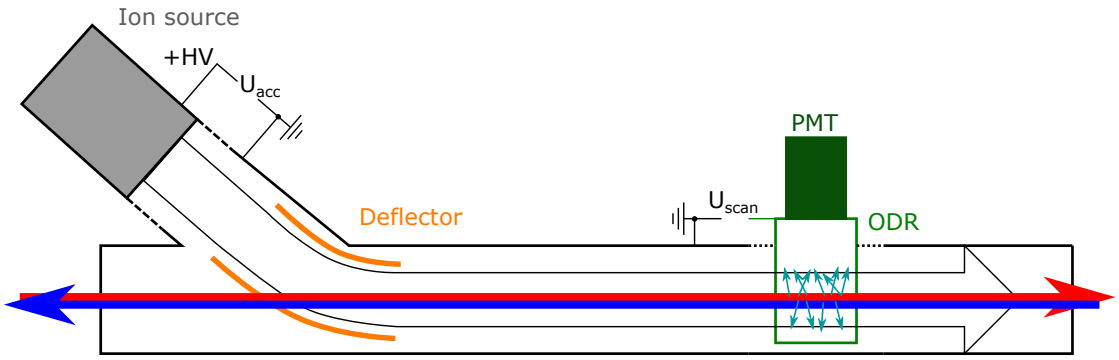

Figure 2.2: Schematic of a typical setup for collinear laser spectroscopy. Ions are produced in an ion source (grey) on a high voltage platform and accelerated towards the beamline which is on ground potential. The electrostatic deflector (orange) bends the ion beam depicted as black framed arrow. The optical detection region (ODR) can be floated with the voltage U_{scan} and reflects the fluorescence photons into the photomultiplier tube (PMT). The laser beams can be send through the beamline collinear (red) or anticollinear (blue).

In Fig. 2.2 the basic layout of such a setup is depicted. The ions are produced in an ion source which is floated on a high-voltage platform with typically 10 - $60\,\text{kV}$ to acclerate the ions electrostatically. The rest of the beamline is connected to ground potential and the beamline is typically evacuated to pressures below $1 \times 10^{-6}\,\text{mbar}$. The ion beam is then superimposed with the laser beam by an electrostatic deflector. The resonance condition from Eq. 2.10 is fulfilled if the laser frequency matches the Doppler-shifted frequency of the ionic transition. Hence, this resonance condition depends solely on the velocity of the ions which is defined by the acceleration voltage, the charge state, and its mass. To restrict the resonant interaction of the ion with the laser beam to the fluorescence detection region, the lather can be floated to an independent voltage. This circumstance can even be used to actively control the resonance condition by the applied voltage.

$$\nu_L = \nu_0 \left[1 + \frac{qU_{\text{tot}}}{mc^2} \left(1 \pm \sqrt{1 + 2\frac{mc^2}{qU_{\text{tot}}}} \right) \right] \tag{2.11}$$

The voltage U_{tot} is the total potential difference between the ion source and the detection region, which is the sum of the acceleration voltage U_a of the ion source platform and the

additional voltage on the detection region U_s. Scanning these voltages is equivalent to scanning the laser across a frequency range corresponding to the varied Doppler shift. This process is called Doppler tuning as it uses the Doppler effect to tune the laser frequency in the rest frame of the ion. The main advantage of this procedure is that scanning the voltage can be processed with high accuracy in a much faster way than scanning the laser.

The fluorescence detection is implemented by a combination of elliptical and parabolic mirrors, which have the ion and laser beam in one focal point to reflect the emitted fluorescence light onto a photomultiplier tube [64]. This photomultiplier can detect single photons and creates a 5-V rectangular pulse that can be counted and processed by computer hardware [65].

2.2 Atomic spectra

Atomic transition lines have played an important role in the foundation of quantum mechanics to discover the structure of the electron shells and the interaction between them and still do. Increasing precision allowed to discover also the interaction between the nucleus and the atomic shells; the so-called hyperfine structure. Nowadays, it is used routinely to reveal properties of the nucleus and improve our understanding of nuclear structure. The isotope shift contains information on the nuclear size and allows us to extract the change in the mean square charge radius along the isotopic chain, and the hyperfine splitting allows the determination of the nuclear magnetic dipole moment and the electric quadrupole moment.

2.2.1 Isotope shift

After discovering that the elements of the periodic table are defined by their number of protons Z in the nucleus, but could be composed by different combinations of neutrons N, the atoms with the same number Z but different N were called isotopes. This was derived from the Greek *isos* (equal) and *topos* (place), referring to the same place in the

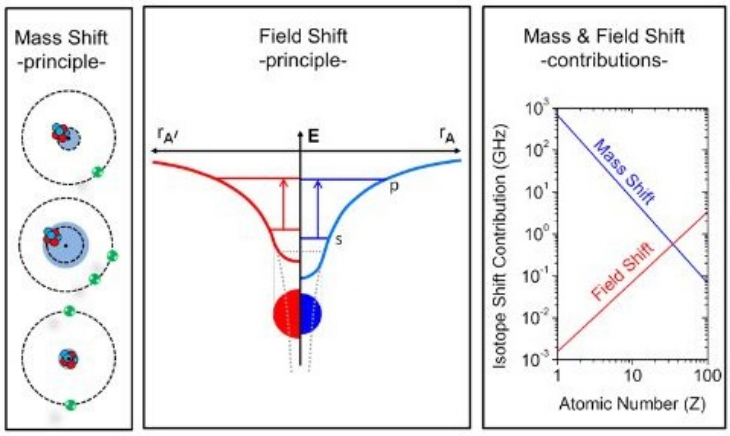

(a) **(b)** **(c)**

Figure 2.3: The different effects on the isotope shift from [66]. a) Graphical representation of the center-of-mass motion of the nucleus and the influence of the correlation of the electrons, which can enhance or reduce this effect. b) Influence of the finite nuclear size on the atomic coulomb potential and how this affects the s- and p-orbitals. c) Contribution of the mass shift and the finite nuclear size effect to the isotope shift as a function of the atomic number Z. Reprinted by permission from Springer Nature: Lecture Notes in Physics 879, "Nuclear Charge Radii of Light Elements and Recent Developments in Collinear Laser Spectroscopy" in The Euroschool on Exotic Beams, Vol. IV, W. Nörtershäuser and C. Geppert, Copyright Springer-Verlag Berlin Heidelberg 2014

periodic table [67]. The proton number and the charge state of the atom define the atomic transition lines. These lines are strongly depending on the electronic configuration and, hence, an excellent fingerprint for each element. Nevertheless, the amount of neutrons inside the nucleus does also have an impact on the transition lines. It introduces a shift between the transition frequencies of two isotopes,

$$\delta\nu^{AA'} = \nu^{A'} - \nu^{A} \tag{2.12}$$

and is called the isotope shift between the isotope A' and the reference isotope A.

This isotope shift is mainly caused by two effects (compare [66]). One effect correlates

with the change in mass of the nucleus (M) by adding or subtracting one neutron, called the mass shift (MS). The other effect correlates with the change in size of the nucleus or more precisely the change in the mean square charge radius and is called field shift (FS). Hence, the isotope shift can be expressed as

$$\delta\nu_{\mathrm{IS}}^{AA'} = \delta\nu_{\mathrm{MS}}^{AA'} + \delta\nu_{\mathrm{FS}}^{AA'} \tag{2.13}$$

The mass shift itself is again composed of two terms, the so-called normal mass shift (NMS), which is caused by the change in center of mass motion between the active electron in the transition, and the nucleus, which is depicted in the top of Fig. 2.3 a. The other term is the so-called specific mass shift (SMS) that is caused by the correlation with other electrons. In Fig. 2.3 a this is represented for two extreme constellations, with enhanced and cancelled nuclear motion, in the middle and lower part respectively. This can be summarized as

$$\delta\nu_{\mathrm{MS}}^{AA'} = \frac{M_{A'} - M_A}{M_A M_{A'}}(K_{\mathrm{NMS}} + K_{\mathrm{SMS}}) \tag{2.14}$$

The field shift originates from the finite size of the nucleus. The spatial charge distribution of the nucleus changes the attractive potential inside the nucleus from the pure Coulomb potential of point-like charge (see Fig. 2.3 b. This change affects especially electrons in the s-orbital as they have the highest probability of being inside of the nucleus. The probability density of an electron in the p-orbital at the nucleus is close to zero. For this reason, a transition from an s to a p-orbital is a tool to investigate the influence of the field shift in different isotopes. The isotopic field shift depends on the atomic number Z and the change of the electron density at the nucleus $\Delta|\Psi_0|^2$ for each transition as well as the difference in the mean square charge radius $\langle r_c^2\rangle$ between the isotopes A and A' [66]

$$\begin{aligned}\delta\nu_{\mathrm{FS}}^{AA'} &= \frac{Ze^2}{6h\epsilon_0}\Delta|\Psi_0|^2(\langle r_c^2\rangle^{A'} - \langle r_c^2\rangle^{A}) \\ &= \frac{Ze^2}{6h\epsilon_0}\Delta|\Psi_0|^2\delta\langle r_c^2\rangle^{AA'} = F\delta\langle r_c^2\rangle^{AA'}.\end{aligned} \tag{2.15}$$

The atomic number Z and the natural constants are the same for all isotopes and the

mass-dependence of $\Delta|\Psi_0|^2$ is very weak and can be neglected in most cases. Hence, the electronic part in Eq. 2.15 is usually summarized in the field-shift constant F. For small atomic numbers, adding a neutron leads to large relative changes of the mass and therefore a significant mass effect, which decreases roughly proportional to $1/M^2$. Contrary, the field shift dominates in heavier nuclei since it increases with Z^2 as shown in Fig. 2.3 c.

Combining Eq. 2.14 and Eq. 2.15 results in the total isotope shift expressed as

$$\delta\nu_{\mathrm{IS}}^{AA'} = \frac{M_{A'} - M_A}{M_A M_{A'}}(K_{\mathrm{NMS}} + K_{\mathrm{SMS}}) + F\delta\langle r_c^2\rangle^{AA'}. \tag{2.16}$$

2.2.2 King-Plot analysis

The nuclear masses M are usually sufficiently well known [68] and can be summarized to the mass scaling factor

$$\mu_M = \frac{M_{A'} - M_A}{M_A M_{A'}}. \tag{2.17}$$

Dividing Eq. 2.16 by μ_M and combining the two mass-shift factors to one $K_{\mathrm{NMS}} + K_{\mathrm{SMS}} = K_{\mathrm{MS}}$ this results in

$$\begin{aligned} \frac{\delta\nu_{\mathrm{IS}}^{AA'}}{\mu_M} &= K_{\mathrm{MS}} + F\frac{\delta\langle r_c^2\rangle^{AA'}}{\mu_M} \\ \widetilde{\delta\nu}_{\mathrm{IS}}^{AA'} &= K_{\mathrm{MS}} + F\widetilde{\delta\langle r_c^2\rangle}^{AA'}. \end{aligned} \tag{2.18}$$

This modified isotope shift $\widetilde{\delta\nu}_{\mathrm{IS}}^{AA'}$ will allow to separate the mass shift factor K_{MS} and the field shift factor F as offset and inclination of a straight line fit along the modified charge radius $\widetilde{\delta\langle r_c^2\rangle}^{AA'}$, respectively. This technique is known as a "King-Plot". If at least three charge radii are known from , e.g., electron scattering or muonic spectroscopy, the isotope shift measurement can be used in combination with the King-Plot technique to determine the differential mean square charge radius of the unknown isotopes. If the isotope shift is measured with higher precision than the charge radii, the King-Plot can also improve the values of existing differential charge radii. From the physical constraint

that all isotopes have to fit onto the line, the differential mean square charge radii data points of the King-Plot can be projected onto the fitted straight. To reduce the correlation between F and K, the parameter α can be introduced as described in [69]. This leads to

$$\widetilde{\delta\nu}_{\mathrm{IS}}^{AA'} = K_\alpha + F\left(\widetilde{\delta\langle r_c^2\rangle}^{AA'} - \alpha\right) \tag{2.19}$$

where K_α has no longer the physical meaning of the mass shift factor K_{MS}.

The King-Plot technique can also be used in another variant where the modified isotope shifts of two transitions are plotted against each other [45]. Here, the circumstance is used that the differential charge radius $\delta\langle r_c^2\rangle^{AA'}$ is independent of the measured transition and can be equated with the differential mean square charge radius of another transition. The relation for each isotope pair results again in a straight line equation

$$\widetilde{\delta\nu}_{\mathrm{IS2}}^{AA'} = \frac{F_2}{F_1}\widetilde{\delta\nu}_{\mathrm{IS1}}^{AA'} + K_{\mathrm{MS2}} - K_{\mathrm{MS1}}\frac{F_2}{F_1} \tag{2.20}$$

This technique allows to compare the isotope shifts in different transitions and yields an excellent consistency check. It has been proposed to search for deviations from the linear behaviour as an indication for new physics [70]. Moreover, the field-shift ratio F2/F1 can be used as a benchmark for atomic theory [13], [54], [71].

2.2.3 Hyperfine structure and nuclear observables in atomic spectra

According to the Schrödinger equation for hydrogen, all levels can be characterized by the main quantum number n, the orbital angular momentum l, and the magnetic quantum number m_l. Adding the electron spin S and its orientation m_s as additional degrees of freedom and the interaction between the magnetic field of the orbital motion and the electrons magnetic moment leads to the fine structure. It introduces an additional splitting of the electronic levels, and the arising new terms are characterized by the total angular momentum $\vec{J}$. This is depicted in Fig. 2.4 for the relevant transitions in titanium (compare [72]).

Additionally, hyperfine splitting occurs if the nucleus has an unpaired neutron or proton. In this case the nuclear spin I gives rise to a magnetic moment

$$\vec{\mu_I} = g_I \frac{\mu_N}{\hbar} \vec{I} \tag{2.21}$$

with the nuclear magneton μ_N and the nuclear$g$ factor g_I which is different for each isotope and can be measured by nuclear magnetic resonance, but also be extracted from the optical hyperfine structure.

The energy shift ΔE_D, from the magnetic dipol moment, for each level is shifted by the scalar product of the nuclear magnetic moment $\vec{\mu}_I$ and the magnetic field created by the electron with coupled angular momentum $\vec{J}$ at the nucleus

$$\begin{aligned} \Delta E_D &= -\vec{\mu}_I \cdot \vec{B}_J \\ &= -|\mu_I| \cdot B_J \cdot \cos(\measuredangle(\vec{J}, \vec{I})). \end{aligned} \tag{2.22}$$

Introducing the total angular momentum of the atom $\vec{F} = \vec{J} + \vec{I}$, $\vec{J} = \vec{l} + \vec{s}$ and $\vec{J} \cdot \vec{I} = 1/2(\vec{F}^2 - \vec{J}^2 - \vec{I}^2)$, the cosine of the angle between the electronic angular momentum $\vec{J}$ and the nuclear spin $\vec{I}$ can be written as

$$\begin{aligned} \cos(\measuredangle(\vec{J}, \vec{I})) &= -\frac{\vec{J} \cdot \vec{I}}{|\vec{J}| \cdot |\vec{I}|} \\ &= \frac{1}{2} \frac{F(F+1) - J(J+1) - I(I+1)}{\sqrt{J(J+1) \cdot I(I+1)}}. \end{aligned} \tag{2.23}$$

Adding the hyperfine energy according to Eq. 2.22 to the fine structure energy with the quantum numbers n, l, j, the energy of the level with quantum number F can be written in first order

$$E_{\mathrm{HFS}}(F) = E_{n,l,j} + \frac{A}{2}[F(F+1) - J(J+1) - I(I+1)], \tag{2.24}$$

where A is the hyperfine constant

$$A = \frac{g_I \mu_N B_J}{\sqrt{J(J+1)}}. \tag{2.25}$$

With known values for μ_I [73] for two isotopes, the ratio of the A values of the same electronic state in different isotopes can be calculated

$$\frac{A}{A'} = \frac{g_I \mu_N B_J}{\sqrt{J(J+1)}} \frac{\sqrt{J(J+1)}}{g'_I \mu'_N B_J} = \frac{\mu_I I'}{\mu'_I I} \tag{2.26}$$

with $g_I \mu_N = \mu_I \hbar / I$. If the magnetic moment is known for only one isotope, this relation can be used to determine the unknown nuclear magnetic moment from the observed hyperfine splitting. Moreover, the fact that the ratio of the A values has to be constant provides a crucial test for the correctness of the nuclear spin that has been used in the analysis of the hyperfine splitting.

For nuclei with nuclear spin $I > 1/2$ and $J > 1/2$ the deformation of the nucleus can lead to an additional measurable shift of the energy levels due to its spectrsocopic nuclear quadrupole moment Q. This shift is proportional to the electric field gradient at the nucleus $V_{zz} = \langle \partial^2 V / \partial x^2 \rangle$ [74] and can be expressed as

$$\Delta E_Q = B \cdot \frac{\frac{3}{4} C(C+1) - I(I+1)J(J+1)}{2I(2I-1)J(2J-1)}, \tag{2.27}$$

with the B value

$$B = eQV_{zz} \tag{2.28}$$

and the Casimir-factor $C = F(F+1) - J(J+1) - I(I+1)$. It has to be added to the magnetic dipole-moment shift [74], to obtain the total shift with respect to the undisturbed

Table 2.1: Properties of the different stable isotopes of titanium with the nuclear abundance from [75], masses from [68] and nuclear spin I, μ_I and Q from [73] and $\langle r^2 \rangle$ extracted from [76].

isotope	abun. [%]	mass [amu]	I	μ_I	Q	$\delta\langle r^2\rangle^{48,A}$ (fm^2)
^{46}Ti	8.25(3)	45.95262686 (18)	0			0.1034(25)
^{47}Ti	7.44(2)	46.95175775(12)	5/2	-0.78848(1)	0.29(1)	0.0264(24)
^{48}Ti	73.72(3)	47.94794 (93)	0			0
^{49}Ti	5.41(2)	48.94786463 (12)	7/2	-1.10417(1)	-0.177(8)	-0.131(25)
^{50}Ti	5.18(2)	49.94478584 (13)	0			-0.153(24)

fine-structure energy

$$\begin{aligned}\Delta E_{\text{tot}} &= \Delta E_D + \Delta E_Q \\ &= \frac{A}{2}C + B \cdot \frac{\frac{3}{4}C(C+1) - I(I+1)J(J+1)}{2I(2I-1)J(2J-1)}.\end{aligned} \tag{2.29}$$

Analyzing the hyperfine spectrum of a certain transition can reveal information about the nuclear spin I and the nuclear magnetic moments and quadrupole moments, which can be extracted from the A and B values by comparing them to a reference isotope with known nuclear moments. The isotope shift is determined from the center of gravity of the hyperfine splitting. This way the odd isotopes can be used in a King-Plot analysis as well to determine the nuclear charge radius.

2.3 Titanium

Titanium is the second-lightest element of the transition metals which are the metals with a partially filled d shell. Since it is lighter than iron, it can be produced during the nuclear fusion in stars which makes it an element that is abundant already in the first generation of stars [77]. This makes it an interesting candidate for nuclear astrophysics as mentioned in Sec. 1. There exist five stable isotopes listed in Tab. 2.1 with their natural abundances [75] and their nuclear spin.

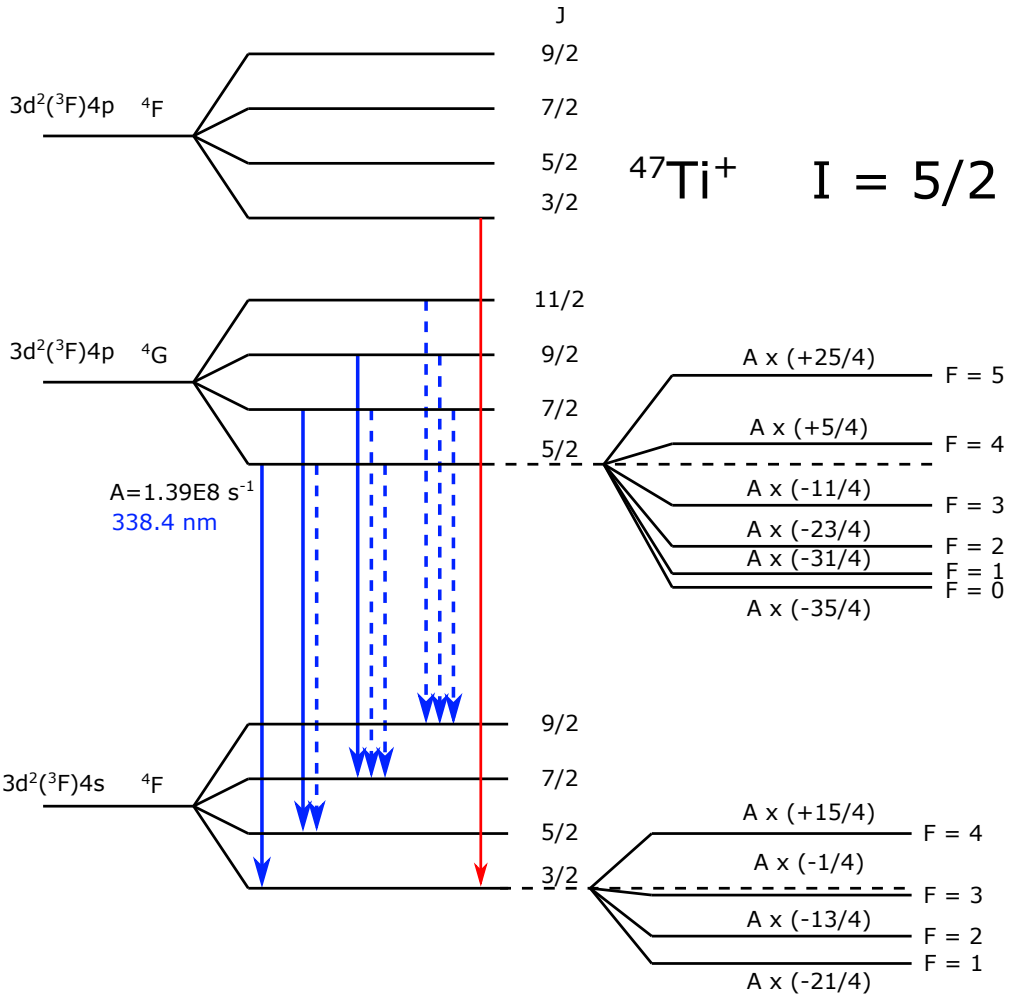

Figure 2.4: The relevant levels of Ti^+ for this work, represented for the case of $^{47}Ti^+$. The ground state is the $3d^2(^3\mathrm{F})4s\ ^4F$ state that splits into four fine structure levels which can further split into hyperfine levels, shown for the $J = 3/2$ level. The upper level used in this work is the $3d^2(^3\mathrm{F})4p\ ^4G$ state which also splits into four four fine structure levels and the hyperfine levels are shown for the case of $J = 5/2$. All possible transitions in the fine structure are shown in blue, while the ones measured in this work are shown in solid blue. The $3d^2(^3\mathrm{F})4p\ ^4G_{3/2}$ transition to the lowest line is the transition used by [47] and marked in red.

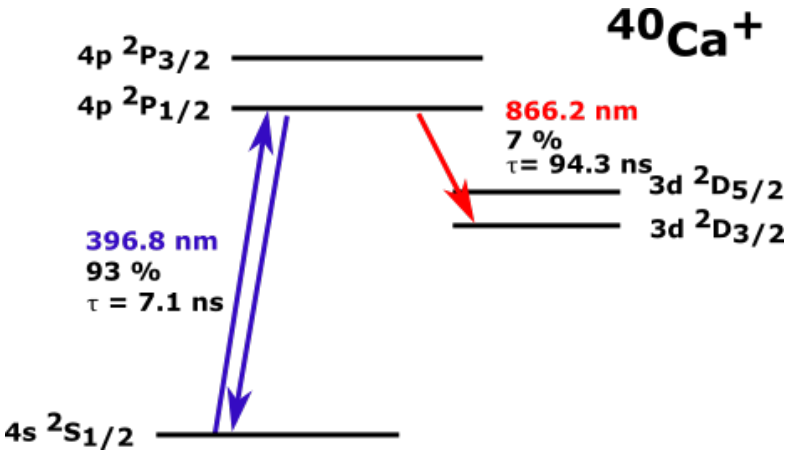

Figure 2.5: Relevant energy levels of Ca^+ for the spectroscopy measurements. In this work the D1 transition at $396.8\,\mathrm{nm}$ was used. The $4p\,^2P_{1/2}$ state has a probability of 93% to decay back into the $4s\,^2S_{1/2}$ ground state, and a probability of 7% to decay into the meta-stable $3d\,^2P_{3/2}$ state.

In Fig. 2.4 three different levels of the titanium ion are depicted. The lowest level is the $4s$ state which is the ground state of the ion. The $4p$ states are grouped by their total orbital angular momentum $L = 4\,(G)$ and $L = 3\,(F)$. According to the spin $S = 3/2$ of the two d and the p electron, all three levels can split into four fine-structure levels with the total angular momentum $J = L - S, ..., L + S$. The fine-structure splitting within the quadruplet is of the order of THz. In blue, all possible fine structure transitions are marked while the solid lines mark the transitions that have been measured in this work. The transition used by Gangrsky et al. [47] to measure all stable isotopes and ^{44,45}Ti online is additionally shown in red.

The hyperfine splitting that is of the order of a few $100\,\mathrm{MHz}$ is shown for the $3d^2(^3\mathrm{F})4s\,^4F_{3/2} \rightarrow 3d^2(^3\mathrm{F})4p\,^4G_{5/2}$ transition in the isotope ^{47}Ti. This transition splits into 12 hyperfine lines, the other two measured transitions split into 15 hyperfine lines.

2.4 Calcium

The transitions to the fine-structure doublet of the Ca^+ ion lead from the $4s\,^2S_{1/2}$ ground state to the $4p\,^2P_{1/2}$ and $4p\,^2P_{3/2}$ levels. Both transition wavelengths can be produced by lasers with sufficient power for spectroscopy. In this work, the $4s\,^2S_{1/2} \rightarrow 4p\,^2P_{1/2}$ transition shown in Fig. 2.5 was used for spectroscopy. The upper level can decay with a probability of 7% into the meta-stable state $3d\,^2D_{3/2}$ which can be considered stable during the interaction time of the order of µs. The lifetime of the $4s\,^2S_{1/2} \rightarrow 4p\,^2P_{1/2}$ transition of $7.1\,\mathrm{ns}$ corresponds to a natural line width of $22.4\,\mathrm{MHz}$. In this work only the most abundant isotope ^{40}Ca was measured.

2.5 Laser ablation

Laser ablation describes the process of material removal of a target. This can be used from art restoration [78] to cutting and engraving materials. When the photons from the laser pulse hit the target material the electromagnetic wave energy is transferred into heat on the target surface [79]. For low laser fluence the laser pulse that hits the target mainly vaporizes some material on the surface. For higher fluence $\approx 1 \times 10^9\,\mathrm{W\,cm^{-2}}$ excitation and ionization of the vaporized atoms occurs and a plasma is formed [80].

The laser pulses used for laser ablation, range from fs pulses up to µs pulses. Often ns Nd:YAG lasers are used because they are comparably cheap-, tabletop instruments and can provide a large fluence. With increasing use in industry, fs lasers are becoming a competitive alternative nowadays. Referring to the ablation process the main discrepancy between fs and ns laser ablation is that the fs laser pulse is shorter than the heat transfer time within the material. This has great advantages as there is no heat influence on the material and no melting for the fs laser pulse leading to a cleaner ablation hole. For ns laser pulses the target material melts, and overheating can lead to phase explosion [81], [82]. In this case also larger droplets and macroscopic parts of the material are ejected from the target. The longer pulse duration has the advantage that the tail of the laser

pulse can interact with the ablation plume via inverse Bremsstrahlung and photionization. Nanosecond lasers might therefore produce a better ion to neutral ratio as stated in [83].

The ablation plume produced by the laser ablation contains mirco-particles, atoms and ions with a temperature of the order of tens of thousands of centigrade [84], [85]. Together with effects like coulomb explosion [86], ions with the kinetic energy of up to several hundred eV can be created [87], [88]. To confine the size of the plume, which is nicely depicted in [89], and cool down the ions, a buffergas e.g. helium, is used [90].

2.6 Buffer gas cooling and extraction

The high temperatures created during ablation and the expansion of the ablation plume lead to a broad energy spectrum of the ions combined with a large divergence. To reduce the temperature of the ions, they can be produced in the presence of an inert gas. The ions will undergo collisions with the buffer gas and exchange momentum by elastic collisions. This will lead to a thermal equilibrium which is at about the temperature of the buffer gas and the surrounding chamber. For simple setups this can be used to cool ions down to ambient temperature, but with more effort in cryogenic systems this technique can be used for cooling ions or atoms to a few Kelvin. It is often used to reduce the energy of beams like at SHIPTRAP [91], [92] or IGISOL [93], [94]. Another area is stopping and extracting ions from active targets [32], [95] or laser ablation [28] like in this work. To extract the ions from these gas cells, RF funnels or RF carpets are frequently used in combination with DC gradients. After extraction , the ions are often further cooled with buffer-gas filled radio-frequency quadrupole ion guides. These ion guides can have segmented sections allowing to add a DC gradient which can be used as an ion trap to accumulate ions and release them as short bunches as demonstrated in [26], [96]–[100].

In contrast, an extraction driven just by the gas flow without DC fields is proposed in [34], [102], developed on computer simulations based on full Navier-Stokes equations described in [103] for the gas flow, combined with ion trajectory simulations in SIMION. Here the transport of the ions depends on the velocity of the gas flow. For this reason a

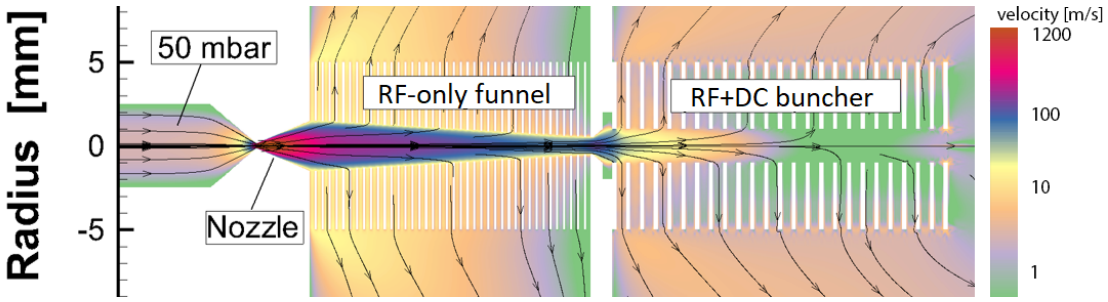

Figure 2.6: Grafical depiction of the RF-only funnel, the RF+DC buncher and the gas velocities [101].

small stopping gas cell (of the order of a few mm) is required to reduce the extraction time and minimize the collisions with buffer gas impurities which are leading to charge exchange or molecule formation. The extraction through a supersonic nozzle forms a high velocity gas jet that is able to carry the ions into the next differential pumping stage as shown in Fig. 2.6. The buffer gas is reduced by pumping after exiting the funnel through the gaps between the electrodes. The fast alternating RF voltages on the electrodes form a repulsive pseudo potential for the ions [104]

$$V_{\text{max}} = \frac{qV_{RF}^2}{4\pi m d^2 f^2} \tag{2.30}$$

with the RF voltage amplitude V_{RF}, the ion charge q, the ion mass m, the electrode distance d, and the applied RF frequency f. The RF-funnel technique is also often used in mass spectrometers and more information about it can be found in [105]–[108]. The RF-only system was demonstrated in [29], [30] with Xenon gas and a combination of laser ablation and an RF-only funnel was investigated in [33].

For less gas flow, a DC gradient is necessary for ion transport through the RF ion guide. Similar to the RFQ cooler and buncher described in [26], [97]–[100], this gradient can be combined with a potential barrier at the end to form a potential well as depicted in Fig. 2.7. Within this potential well, the ions can still collide with the remaining buffer gas and cool down further. This also allows accumulating ions for a certain time and release them as a short intense ion bunch by switching down the potential barrier.

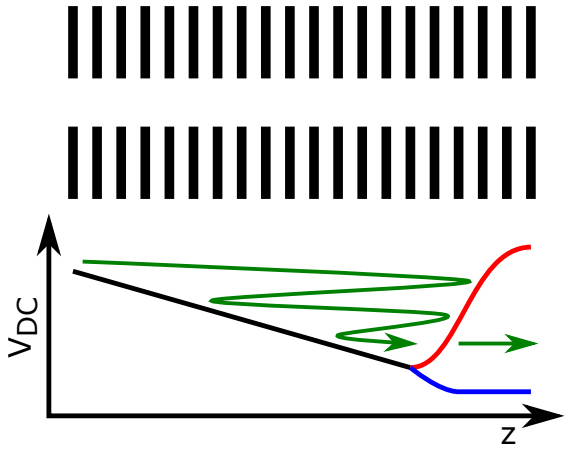

Figure 2.7: DC potential along the z-axis of the RF+DC buncher. For bunching it is possible to switch the potential of the last electrodes between a blocking mode (red) and a transmission mode (blue). In green the path of the ions during accumulation and cooling is depicted.

3 Setup

The design, construction and realization of the **T**hermalized-**I**on **M**ulti-purpose **S**ource (TIMS) has been a central part of this work. Its technical layout and adaption to the collinear apparatus for laser spectroscopy and applied sciences (COALA) that was used for first laser spectroscopy measurements on ion beams from this laser-ablation source is presented in this chapter. The design of the source was inspired by Victor Varentsov's simulations as exemplary shown in Fig. 3.1. All gas dynamic simulations presented in this work were performed by him and communicated privately.

3.1 Overview

The ion source consists of three stages as they are schematically shown in Fig. 3.1: First, the ion production, which takes place in the high-pressure ($50\,\mathrm{mbar}$) ablation stage and is realized with a short and intense laser pulse that releases material from a target surface. A hot plasma is formed, but the expansion of the ablation plume is stopped by the surrounding gas. Generated ions are cooled by collisions and transported within the gas stream through a supersonic nozzle that connects the ablation stage with the funnel stage which operates at a pressure of slightly less than $1\,\mathrm{mbar}$. Here, the ions are guided through an RF-only funnel and the diameter of the ion cloud is narrowed down to a diameter of 1 mm. Finally, the ions, still dragged by the gas flow, pass the second nozzle into the third stage. Here, at a pressure of $1 \times 10^{-4}\,\mathrm{mbar}$, the DC gradient from an RF-DC ion guide takes over. Besides pure transport, the RF-DC ion guide is designed to allow

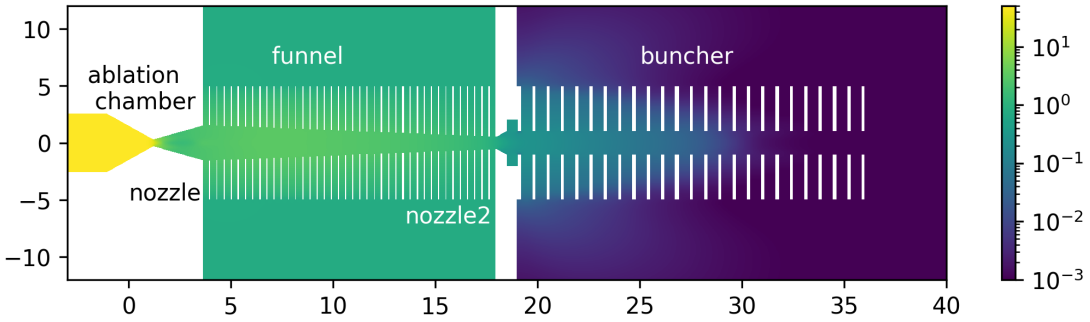

Figure 3.1: Result of a gasdynamic simulation with the 0.6-mm nozzle [101]. The pressure in the ablation chamber (left) is $50\,\mathrm{mbar}$, which than lowers to about $1\,\mathrm{mbar}$ at the funnel chamber and below $10^{-3}\,\mathrm{mbar}$ after the buncher. The gas expansion behind the second nozzle is clearly visible. The ions are confined by the bunchers RF field.

for the preparation of a bunched beam. Hence, the stage is named buncher stage. As a last differential pumping barrier, a skimmer is installed at the transition to the ultra-high vacuum beam line. The technical layout of the individual sections is described below, including the gas regulation system required to maintain the pressure relation between the different stages.

3.2 Gas regulation system

The gas regulation system is crucial for maintaining the pressures relevant for ion cooling and transport. Particularly, it must maintain a constant pressure at the laser-ablation target as it is required to stop the plume expansion and to extract the ions through the subsequent chambers into a vacuum beamline at pressures much less than $10^{-4}\,\mathrm{mbar}$. High-purity helium gas (99.999 mol %) is required to mitigate neutralization or molecule formation processes of the produced ions. In Fig. 3.2 the main components of the gas supply and vacuum system are shown. At the gas bottle, the pressure is reduced to about $1.5\,\mathrm{bar}$ absolute pressure, hence about $0.5\,\mathrm{bar}$ above atmospheric pressure in the laboratory. The gas is transported via a stainless steel tube connected with Swagelok

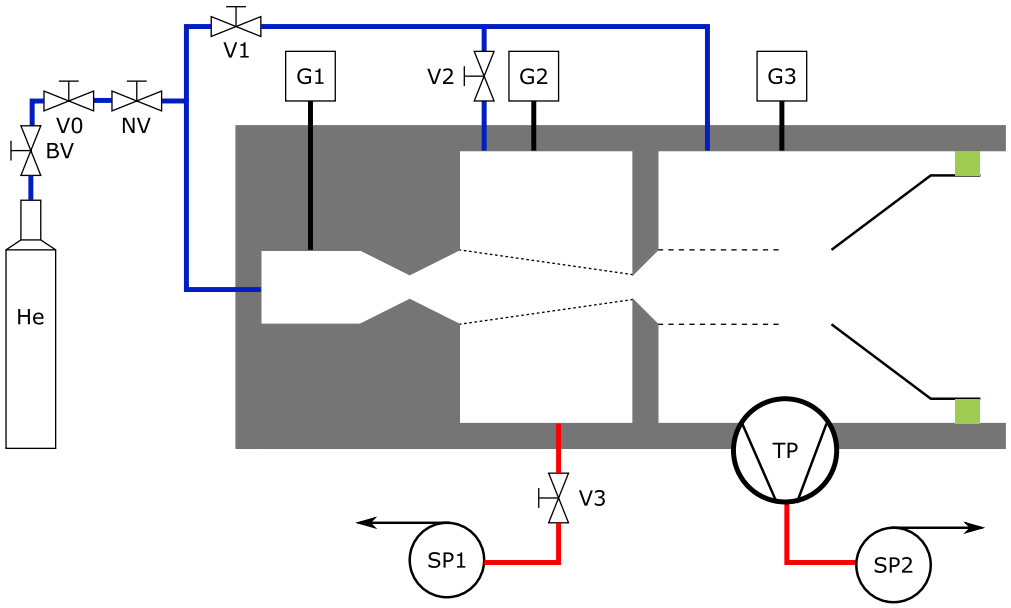

Figure 3.2: Vacuum schematics of the ions source including the gas valves and pressure gauges. The gas inlet system is depicted in blue and the outlets in red. NV is the needle valve to fine-adjust the gas flow into the system and BV the valve of the bottle. V0-V3 are pneumatic valves to open or block the gas flow. G1-G3 are the pressure gauges from Pfeiffer Vacuum (G1: PCR 280, G2: CMR 362, G3: PKR 360). TP is the turbomolecular pump (Ebara: EMT900M) and SP1 (Leybold: ECODRY 40 plus) and SP2 (Edwards: nXDS20i) are the dry scroll pumps. In green the insulators are depicted holding the skimmer in place and disconnecting it from the high-voltage of the ion source platform. The skimmer is the last differential pumping barrier before the spectroscopy beamline.

connectors to an all-metal gas-dosing valve. The 0.5-bar over-pressure in the tube ensures that tiny leakages in the connections will cause helium leaking to the outside instead of other gases diffusing into the He line. After exchanging the He bottle it is even possible to bake the steel tube while pumping through the gas dosing valve to reduce the amount of contaminants evaporating from the tube walls. The gas-dosing valve (NV) feeds the helium into the first chamber of the ion source, where the ablation takes place. The pressure in this first chamber can be actively stabilized by using the pressure signal from vacuum gauge G1 as an input for the regulation of the dosing valve. As the pressure was sufficiently stable within $\pm 5\,\%$ without active regulation, the pressure was once adjusted

manually and then valve V0 was used to turn the gas flow on and off. The gas introduced in this chamber flows through a replaceable super sonic nozzle with currently available throat diameters of $0.6\,\mathrm{mm}$ and $0.8\,\mathrm{mm}$ into the next chamber. Here, an oil-free scroll pump with a throughput of 40 l/s is used to reduce the pressure to $0.77\,\mathrm{mbar}$ at gauge G2 with the 0.6-mm nozzle in place and 50-mbar helium-pressure in the first chamber. The remaining gas enters the third chamber via the second nozzle which has a fixed diameter of $1\,\mathrm{mm}$. Here a 1000-l/s turbomolecular pump is used to reduce the pressure to about $10^{-4}\,\mathrm{mbar}$ (gauge G3) under the mentioned conditions. The turbomolecular pump is backed by another dry scroll pump.

All components inside the source are either made from metal or PEEK [1]to be bakeable to at least $100°$C to reduce the amount of contaminants evaporating from the surfaces in the chambers. Efficient pumping of the first two chambers during the baking process is ensured by opening the valves V1 and V2 to bypass the two nozzles and closing V3 to avoid back-streaming from the scroll pump. To monitor pressure during baking, only gauge G3 can be used, since G1 (10 - $1000\,\mathrm{mbar}$ useful range for He) and G2 (1×10^{-2} - $50\,\mathrm{mbar}$) are designed for operation in different pressure regimes. G1 is a combined diaphragm and Pirani gauge with the diaphragm calibrated for the range between 0.1 and $1000\,\mathrm{mbar}$ but uses a combined value for the range between 0.1 and $10\,\mathrm{mbar}$ which is inaccurate for He. The Pirani part will not give a useful reading in this pressure range and is only used for pressures below $0.1\,\mathrm{mbar}$ to recognize larger leaks. G2 is a pure diaphragm pressure gauge calibrated for the range between 1×10^{-2} and $100\,\mathrm{mbar}$ to monitor the pressure in the second chamber during operation. Both diaphragm gauges measure the total pressure and are gas-type independent under standard operating conditions. This is different for gauge G3 which is a full-range gauge consisting of a Pirani and a cold cathode sensor. This combination allows measuring pressures from atmospheric pressure down to $10^{-9}\,\mathrm{mbar}$ for air like gas compositions. This way we can monitor the whole baking process when the system was flooded with air before. However, in a helium-filled system it has no calibration at pressures above $1 \times 10^{-5}\,\mathrm{mbar}$. Below this pressure, the reading has a constant correction factor of 5.9 for helium. As the reading of G3 is about

[1]Polyether ether ketone

$3 \times 10^{-5}\,\mathrm{mbar}$ under standard operation conditions of the ion source and, thus, slightly above the calibration point, it should be considered to be affected with a larger uncertainty than the $\pm 30\,\%$ stated by the manufacturer.

3.3 Ion source design

The ion source consists of three main stages, which are the ablation stage, the RF-funnel stage, and the buncher stage. Figure 3.3 provides an overview of its mechanical assembly. The laser ablation and funnel construction is mounted to one arm of a vacuum cross with 160 mm tube diameter noted as part **N**. The helium gas is fed into the ablation stage via a gas-dosing valve connected to Flange **A**. This flange is removable to access the target chamber **B** which is the core part of the ablation stage. This stage consists of one single flange that has an axial center bore to contain the ablation chamber and two bores in transversal direction to allow for laser access **D** to the target and rotational access to the target holder **E**. To focus the laser onto the target, a lens can be placed in front of the view port visible on top of bore **D** with the possibility to be moved along its symmetry axis. Placing the lens outside the entrance window allows optimization of the focus by adjusting the distance to the target and testing its impact on the ion production process. The drawback is that the minimal spot size of the laser focus is larger for a larger focal length. A focal length $f = 175\,\mathrm{mm}$ was used in the configuration with the lens outside of the window leading to a focal-spot size of $400\,\mu\mathrm{m}$ diameter. To decrease the focal-spot size, a lens with a focal length of f = 36 mm was later placed directly above the ablation chamber **B**. This lens could not be adjusted after its implementation and produced a focal-spot size of about $100\,\mu\mathrm{m}$ in diameter. It was used in all measurements described in this work. The target is placed on a holder that can be rotated with a motor outside the vacuum through a rotary feedthrough (**E**) to prevent hole burning at a fixed position.

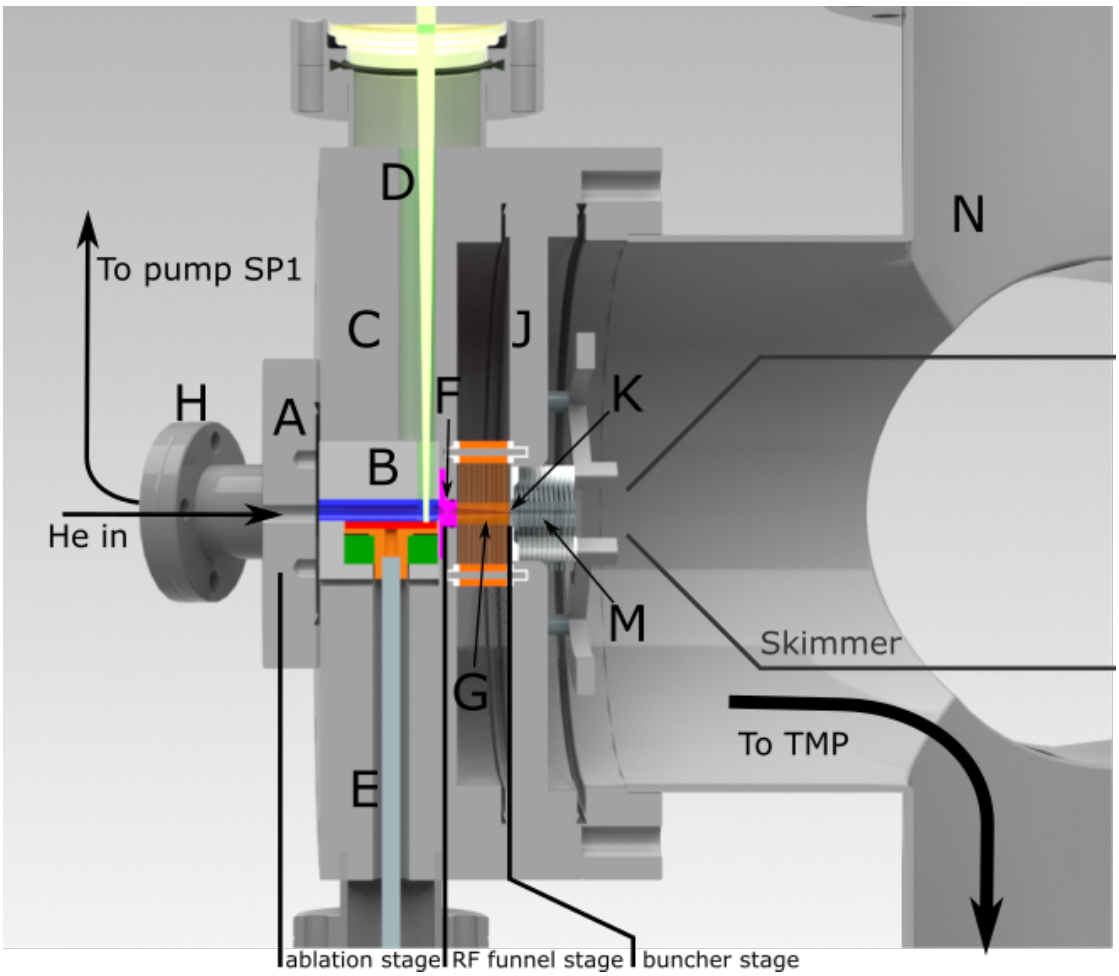

Figure 3.3: Assembly drawing of the ion source. The helium inlet is connected to flange **A** with the gas flowing into the ablation stage which mainly consists of the ablation unit **B** and is integrated into the main flange **C**. Through a window flange and a bore hole the ablation laser beam **D** reaches the target. From below a shaft **E** is connected to the target to allow rotation during operation. The ablation chamber is separated from the RF-funnel stage by the first nozzle **F**. The second stage chamber houses the RF-funnel **G** and is evacuated through the gas outlet **H** which leads to the sroll pump SP1. Gas flow and ion transport to the buncher stage is provided by a second nozzle **K** milled into in the center of flange **J**. On the right side the buncher **M** is mounted. The flanges **C** and **J** are mounted onto a vacuum cross **N** and on the bottom of this cross the turbomolecular pump is mounted. The whole source is connected to the high voltage supply and the ions are extracted to ground potential by a skimmer that is illustrated in grey. This skimmer also acts as differential pumping barrier to the spectroscopy beamline.

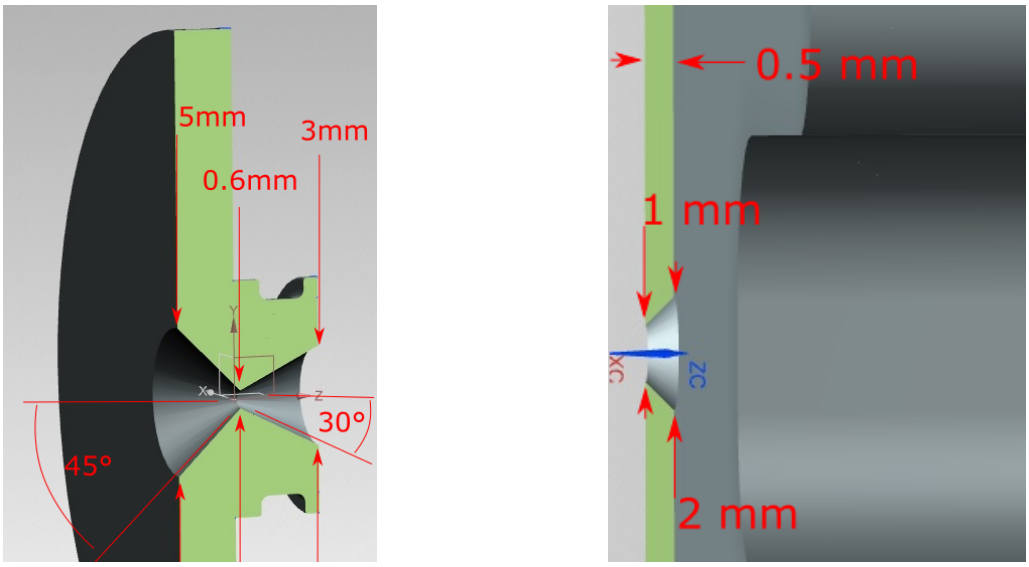

(a) **(b)**

Figure 3.4: The two nozzles of the ion source.
a) The first nozzle has been designed as exchangeable separate part with a converging diverging cross-section machined by electrical discharge machining with the displayed geometry. Here, the 0.6-mm throat diameter is displayed.
b) The second nozzle is a diverging nozzle machined into flange **J** (see Fig. 3.3).

The connection between the ablation stage and the RF-only funnel stage is the supersonic nozzle **F** shown in Fig. 3.4 a. The nozzle is made from stainless steel and its cones where produced by electrical discharge machining to achieve a precisely formed nozzle throat. The nozzle is placed into the designated space between the ablation stage and the funnel stage. This allows to vary the size and shape of the nozzle by exchanging the nozzle plate without changing the overall setup.

In this main flange **C**, there is an additional bore (not shown in the picture) behind the nozzle, where the pressure gauge G2 is connected to monitor the funnel-stage pressure. Another bore connects the scroll pump SP1 with this chamber through flange **H**.

The RF-only funnel is mounted onto flange **J** that is separating the funnel stage from the buncher stage. This flange has the second nozzle with 1-mm throat diameter directly

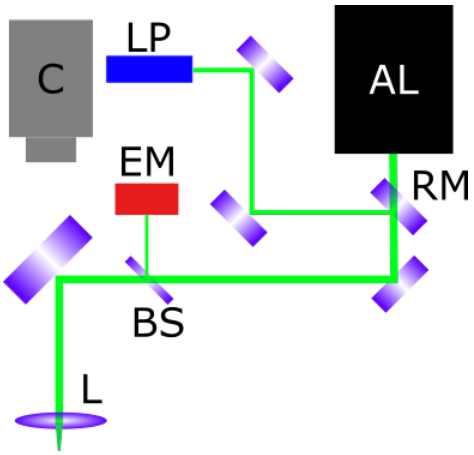

(a)

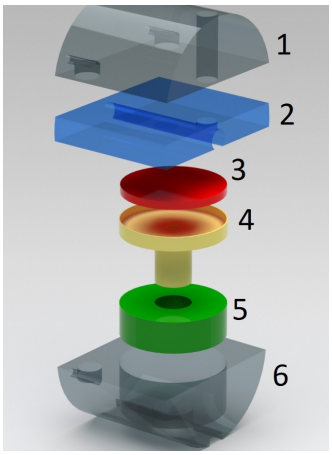

(b)

Figure 3.5: Detailed layout of the ablation unit.
a) Schematic drawing of the ablation laser setup: (AL) ablation laser, (LP) laser pointer, (C) camera, (EM) energy meter, (RM) removable mirror, (BS) beam splitter, (L) lens. b) Exploded view of the ablation unit: (1) top part with laser bore, (2) middle part with 5-mm ablation chamber, (3) 1-inch sputter target, (4) target holder, (5) ceramic bearing, (6) bottom part

machined into its center and is also the mount of the buncher electrode stack.

Both flanges **C** and **J** are then together mounted onto the main vacuum cross **N** on which the turbomolecular pump (TMP) is mounted from the bottom. Into this cross also a skimmer electrode is mounted to accelerate the ions into the subsequent experimental beamline.

3.3.1 Ablation stage

The laser[2] used for ablation is a frequency-doubled, diode-pumped, Q-switched Nd:YAG laser with up to $25\,\mathrm{mJ}$ at $532\,\mathrm{nm}$, 13.9-ns pulse length and a repetition rate of up to 100 Hz. The output energy can be controlled via an on-board attenuator from $0\,\mathrm{mJ}$ to $25\,\mathrm{mJ}$. The

[2] Lumibird Centurion+

laser beam is then widened by a telescope to about 6 mm. For test measurements the laser was focused by a 175-mm lens onto the target surface. The size of the ablation crater was measured by a microscope to be $400\,\mu\mathrm{m}$ in diameter. To facilitate alignment of the ablation laser onto the target, the pulsed beam is superimposed with a green laser beam from a commercial laser pointer as schematically shown in Fig. 3.5 a. The target can be illuminated by a ring of LEDs through the laser-entrance window flange. This allows us to observe the beam spot on the target and to adjust the beam position by a camera, positioned behind the last mirror used to steer the laser beam into the chamber. During measurement the camera is equipped with a 532-nm absorption filter to monitor the visible degradation of the target without being damaged by the intense laser light.

The mechanical part of the ablation stage shown in Fig. 3.5 b is designed to fit into the 40-mm diameter bore hole in the center of the main flange marked as **B** in Fig. 3.3 and consists of 6 parts. The top part (1) has a vertical bore for the laser beam with a diameter of $5\,\mathrm{mm}$ close to the extraction side of the stage. The flow-tube (2) defines the size of the cylindrical buffer-gas cell to 5-mm diameter with the extension of the laser-access bore from the top flange. Increasing the height of this part will allow to enlarge the buffer-gas cell diameter or modify its shape. The ions are produced inside this tube and with the correct buffer-gas pressure they are stopped before they hit the walls. The continuous gas-flow from this tube into the next chamber extracts the ions from the gas cell without any electric fields.

Part (3) is the target in the shape of a 2-mm thick and 25.4-mm diameter sputter target that is available in high purity for many elements. It is placed inside the target holder (4) that is manufactured to enclose the target with a tight fit and has a depth of $2.1\,\mathrm{mm}$ to keep the target from scrubbing against the flow tube part. On the bottom side the target holder has a slit to connect the shaft from the rotary feedthrough. This part is placed into a ceramic bearing (5) to minimize friction during operation. This bearing itself is placed in the bottom part (6) which has an indention milled at the lowest point to speed up the evacuation of the shaft section. The rotary feedthrough is connected to a remotely controlled stepper motor outside of the vacuum, allowing permanent rotation of the target and additional angle tracking.

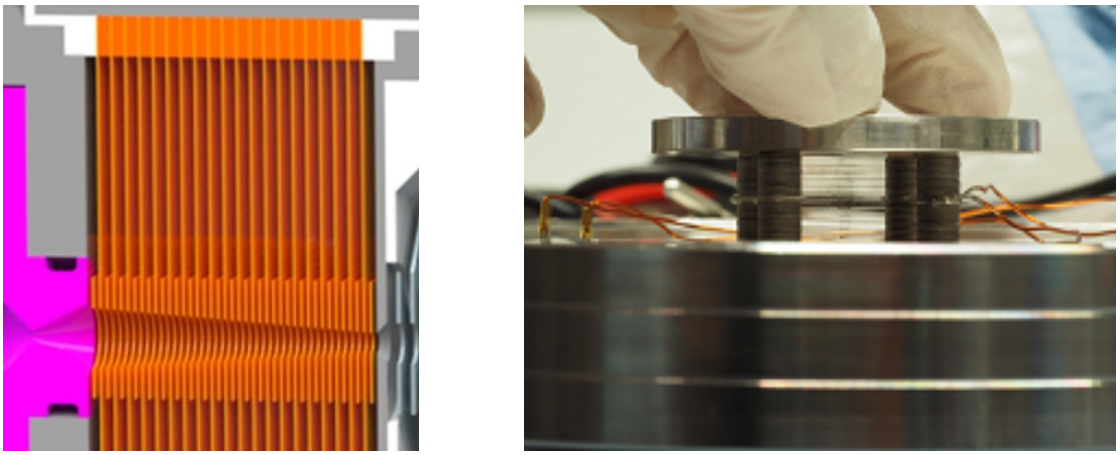

(a) (b)

Figure 3.6: Illustrations of the funnel.
a) CAD model with the first nozzle in magenta, the funnel electrodes in orange and the second nozzle in grey.
b) Picture of the funnel mounted in the flange **J** with finger tips for size comparison.

3.3.2 RF-only funnel stage

The gas transporting the ablated ions enters the RF-only funnel stage through the nozzle throat, reaching supersonic velocities. The high gas-flow velocity slows down during the expansion into the funnel chamber (compare Fig. 3.1). As a constant pressure of $0.75\,\mathrm{mbar}$ is maintained by the scroll pump at the border of the chamber, the helium exits the funnel side slits towards the outer wall. The ions, on the other hand, are pushed towards the center axis of the funnel by the fast alternating RF voltages that produce a pseudo potential with the lowest point on the center axis. The gas density along the funnel axis is still sufficiently high to ensure ion transport through gas collisions. This is advantageous since it eliminates additional requirements of electrode wiring to establish a DC field gradient along the funnel. The space required for such connections would also cause a non-negligible impact on the gas flow.

The RF funnel shown in orange in Fig. 3.6 a has a length of of $14.3\,\mathrm{mm}$ and consists of

41 electrodes which have centred holes decreasing from 3 mm in electrode #1 down to $1\,\mathrm{mm}$ in electrode #41. The electrodes are made of stainless steel sheets of 0.1-mm thickness and are manufactured by laser cutting. Each has a distance of 0.25 mm to the next electrode. Along the funnel, neighbouring electrodes are insulated but every other electrode has to be connected to the same RF-signal to establish the guiding field for the ions. This is achieved by building two stacks of electrodes where the electrodes are separated by a 0.6-mm spacer and mounted on different rods with a relative spacing of 0.3 mm to each other as depicted in Fig. 3.6 a and b. This way, the spacer and the rods can be built of a conducting material like steel and all electrodes of the same phase are fed by a single connection. The rods where the electrodes are stacked on are attached to the separation flange **J** with insulators made of PEEK. These insulators have to differ exactly 0.3 mm in height to allow the correct distancing between the two electrode stacks. Hence, the allowed tolerance of this central piece is less than $0.1\,\mathrm{mm}$. The distance of the shorter insulator to the flange face should be 0.25 mm to have approximately the same spacing as between the electrodes. When assembling the funnel structure, the rods have to be placed into the insulators and the electrodes have to be applied to their position sequentially with increasing hole diameter. To ensure the electrodes are in the correct spatial order, a position number was engraved during production. The central spacers of both electrode stacks have an elongation on one side to connect Kapton-insulated copper wires that lead the RF signal into the stack. After all electrodes are in place, the end of the holding rods are also insulated by PEEK insulators as on the other side. To keep the funnel structure in place for assembly of the source, a 60-mm ring, shown below the finger tips in Fig. 3.6 b, that has holes for the insulators is placed on top which can be fastened by M4 screws. This fastening ensures the equal spacing of the electrodes to avoid short-circuits between the electrodes carrying opposite phases while the source is still disassembled. The ring is also tightened strong enough so that there is no displacement during assembly. Due to additional space calculated for possible longer size of the whole funnel stack arising from the tolerances of the thickness of 41 electrodes and spacers and the use of copper gaskets, the distance between the first electrode and the exit of the nozzle is larger than 0.25 mm and ranges from 0.6 to 1 mm depending on the depth to which the cutting edge of the flange is driven into the copper gasket. Simulations show that the loss caused by this gap

is of the order of 10 % and should be reduced in a next design version.

Measurements with the system showed that the narrow spacing together with the considerable neutral material ablation at the target led to growth of coating layers around the edges of the funnel holes that produced short circuits after some time which will be discussed in more detail in Sec. 3.5.6. The speed of growth of those coatings strongly depends on the target material and usable operation times ranged from a few hours for calcium up to a few days for titanium. Copper, on the other hand, only produced a thin coating that was just barely visible as a copper-red layer surrounding the holes even after several days of operation.

Doubling the spacing distance between the electrodes increased the operation time until a short circuit appeared. However, iron generated thin metal threads between the electrodes that lead to a short circuit within hours of operation. The extraction efficiency with the doubled spacing was still comparable with only about 10 % higher RF-voltages and was used for the final titanium measurements as reported in Sec. 4.2.

3.3.3 The buncher stage

The buncher stage is serving two purposes. One is lowering the transversal emittance by keeping the ions confined at the central axis while the expanding gas after the second nozzle still interacts with the ions. The second is trapping and accumulating the ions to produce short intense bunches. As the length of the second nozzle is $0.5\,\mathrm{mm}$, the buncher electrodes have to be placed behind a stainless-steel wall of 0.5-mm thickness, which is realized by a milled recess in the separating flange (**J** in Fig. 3.3), shown in green in Fig. 3.7 a. To lock the buncher into position, the mount is realized with a 100-mm ring (purple,d) outside the funnel where the flange wall thickness allows threaded blind holes. In contrast to the funnel, a DC gradient is required along the buncher to drag the ions towards its exit, since the gas flow is getting too dilute. Every one of the 25 buncher electrodes is on a different potential and insulated from all other electrodes and the vacuum chamber to realize a DC gradient of -0.064 V/electrode. According to gas dynamic simulations, the gap between the second nozzle exit and the first buncher electrode needs

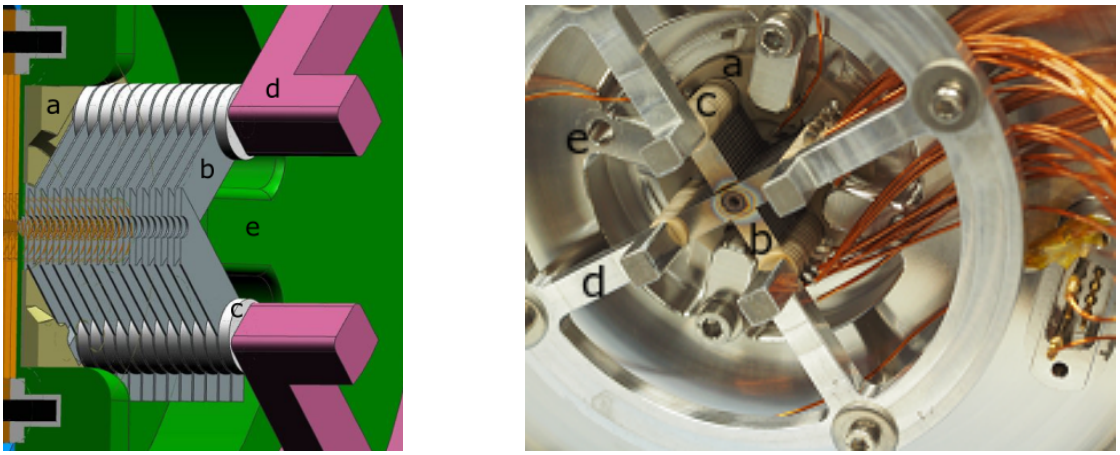

(a) **(b)**

Figure 3.7: Illustrations of the buncher:
a) CAD model showing the base-plate insulator (a), the electrodes (b), the insulation spacer (c), the buncher holder (d), and the mounting flange (**J** in Fig. 3.3) marked as (e).
b) A picture of the buncher with the same parts marked as in a) and the whole wiring attached.

to be enclosed by an insulator to built a gas-filled pocket and prohibit ions and helium to expand before entering the RF-fields. For these reasons, the four holding rods are made of PEEK and mounted on a specially designed PEEK platform (a) shown in beige in Fig. 3.7 a and b. This platform insulates the buncher from the vacuum chamber, ensures the axial and rotational position, and provides the correct spacing of the first electrodes. In this case, the electrodes are made of 0.2-mm stainless steel sheets and have a spacing of $0.5\,\mathrm{mm}$ with a constant hole diameter of $2\,\mathrm{mm}$ in the center. As all electrodes need be connected separately, they are stacked like the funnel in x-shape to spread out the wiring connections which can be seen in the closeup picture shown in Fig. 3.7 b. To provide the correct spacing between the electrodes, PEEK-spacers of $1.2\,\mathrm{mm}$ are placed between the electrodes on each rod. The last electrodes are topped with a final PEEK spacer and locked in place by a holding structure.

The wire connections are realized by including a small extension to the electrodes that

allow to crimp or solder a wire to it. Since the helium gas is permanently flowing away from the center of the buncher, potentially outgasing contaminants from those connections should not diffuse towards the ion beam. Hence, the electrodes are soldered to a flat ribbon cable[3] with 25 Kapton-insulated and PEEK interwoven copper wires to connect them with the feedthrough for the RF and DC signals.

3.4 RF-design and electronics

Besides the laser ablation, the ion extraction by RF guides is a key element of this ion source design. Other implementations of an RF-only funnel [33] show that there is a correlation between the transport efficiency and RF-frequency as well as RF-Amplitude for different masses. For this reason, the RF-system is designed to work with different frequencies and allow amplitudes up to $50\,\mathrm{V_{pp}}$. Simulations suggest testing frequencies between 1 and 10 MHz and amplitudes between 5 and $20\,\mathrm{V_{pp}}$ on the RF only funnel and up to $50\,\mathrm{V_{pp}}$ on the buncher.

3.4.1 Balun

The signals for the two phases of the funnel are sinusoidal signals with the same frequency and amplitude but with a phase shift of $180°$. This kind of signal is called a balanced signal which is illustrated in Fig. 3.8 with the two phases colored in red and blue. Typical frequency generators and amplifiers are built for so-called unbalanced signals where coaxial cables are connected with a signal transported on the copper core and the second conductor, the screen is permanently grounded. To transform this unbalenced signal into the balanced signal, required for the funnel operation, a transformer with a center-tap in the scondary winding can be used. Such a transformer is called a balun (short for balanced to unbalanced -transformer) and can be built as an isolation transformer or an autotransformer. The autotransformer type, as applied in this work and depicted in

[3] Vacom: KAP-SUBD-25-AWG22

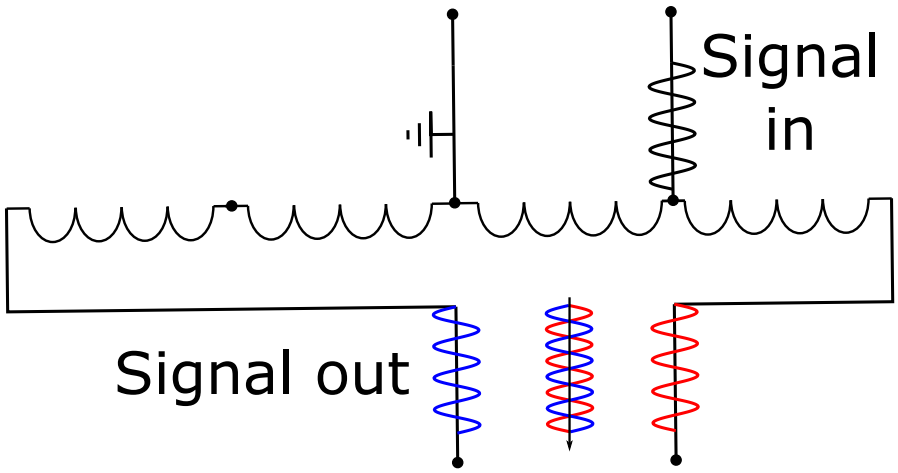

Figure 3.8: Balun autotransformer. The unbalanced signal is fed into the system illustrated as black sinus curve. The ground is connected with the center of the main coil and the output signal is illustrated in red and blue.

Fig. 3.8 uses the same coil as primary and secondary coil and, hence, has the same ground potential on both sides of the transformer [109]. The schematic in Fig. 3.8 shows the unbalanced signal on top in black and the balanced signal in blue and red on the bottom. The transformation ratio of the balun transformer can be chosen to be different from 1:1 to enhance the voltage at the electrodes. By choosing that the input signal uses only 1/4 of the main coil, a transformation ratio of 1:4 was set which was sufficient to achieve the required RF-amplitudes of $50\,\mathrm{V_{pp}}$. To reduce reflections back into the amplifier, the whole transformer with the connected electrical circuit should exhibit an input resistance equivalent close to $50\,\Omega$. For the currents I and the voltages U the transformation ratio a is

$$a = \frac{U_1}{U_2} = \frac{I_2}{I_1}. \tag{3.1}$$

With Ohms law $Z = {}^{U}/_{I}$ this leads to the ratio for the impedances

$$\frac{Z_1}{Z_2} = \frac{U_1}{I_1} \cdot \frac{I_2}{U_2} = a^2. \tag{3.2}$$

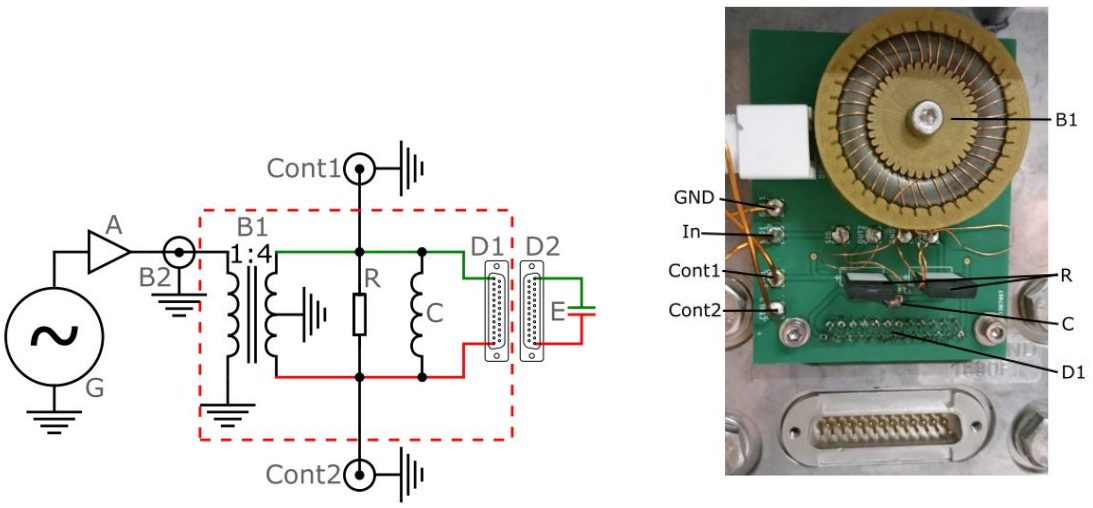

(a) **(b)**

Figure 3.9: Schematic and picture of the RF-system:
a) shows the schematic of the whole system with the RF-generator **G**, the amplifier **A**, the BNC connector for the input signal **B2**, the balun transformer **B1** with a transformation ratio of 1:4 and a GND connection at the center of the second coil, the power resistor **R**, the resonance coil **C**, the two control connectors **Cont1, Cont2**, the D-Sub connector **D1**, the vacuum feedthrough connection **D2**, and the funnel electrodes which mainly act as capacity **E**.
b) shows the actual PCB board with the corresponding components from inside the red-dashed rectangle, but rotated by 90 degree clockwise compared to the schematic.

The transformer used in this work has an impedance transformation of 1:16. Hence, requires an impedance of $800\,\Omega$ to obtain the $50\,\Omega$ input resistance in front of the transformer.

3.4.2 Electric circuit of the funnel

For the funnel electrodes the electric circuit shown in Fig. 3.9 a was realized to produce the RF signal. To generate the frequency and remotely change its parameters, an arbitrary

function generator[4] **G** was used. It can produce sinusoidal signals from below $1\,\mathrm{Hz}$ up to $100\,\mathrm{MHz}$ and amplitudes of up to $10\,V_{pp}$. The output power needs to be amplified to produce signals of up to $50\,V_{pp}$ at the funnel electrodes. For this purpose, an amplifier for amateur radio operators **A** for 2 - $50\,\mathrm{MHz}$ and with $50\,\mathrm{W}$ output power is connected behind the RF generator. The signal from the amplifier is an unbalanced signal that is transformed by a balun transformer (**B1**) with the ratio 1:4 to a balanced signal indicated in green and red for the two opposite phases. The impedance matching is done by two power resistors **R** that can be seen in the photograph Fig. 3.9 b which have a joint resistance of $800\,\Omega$. At the ends of the resistor (**R**) two coaxial connections (**Cont1, Cont2)** are soldered as control outputs which can be connected to an oscilloscope to monitor the time resolved signal and a circuit that can monitor and log the RF amplitude. The coil **C** with inductivity $L = 3.3\,\mu\mathrm{H}$, together with the capacity of the funnel electrodes **E** and the connected coaxial cables, forms an LC circuit with resonance frequency

$$f_r = \frac{1}{2\pi\sqrt{LC}} = \frac{\omega_r}{2\pi}. \tag{3.3}$$

The resonance frequency with all cables connected was $(5.5 \pm 0.2)\,\mathrm{MHz}$ which yields a capacity of the electrodes and the cables of $(254 \pm 20)\,\mathrm{pF}$. When the signal fed into the circuit is at the resonance frequency f_r, the resistance of the LC circuit grows towards infinity. The real resistance of the coil, which is about $1\,\Omega$, limits the resonance resistance to the order of $1 \times 10^{16}\,\Omega$, which can be treated as infinity in this context and also the minor offset effect on the resonance frequency is neglected. Since the resistor **R** and the LC circuit are connected in parallel, the resistance seen from the balun is dominated by the resistance **R**. The balun transforms the $800\,\Omega$ into $50\,\Omega$ seen from the RF-amplifier and back reflections are kept low. The balanced signal is connected to a D-sub connector that fits the electrical feed through of the vacuum flange. Inside the vacuum chamber the signal is guided by Kapton-insulated wires to the funnel. Measurements with a probe directly at the funnel electrodes indicated that the signal monitored by the control outputs represents the signal at the electrodes within 5 % uncertainty.

[4] Tektronix AFG 3102

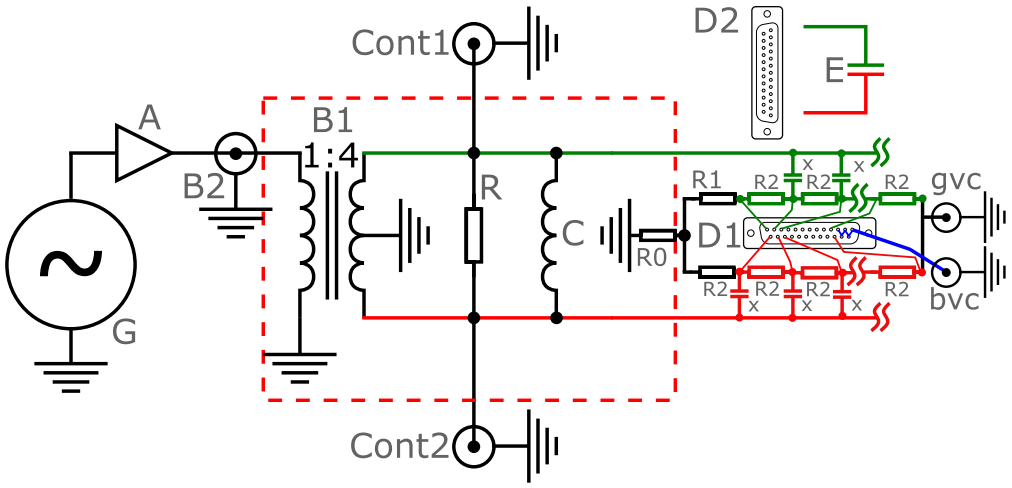

Figure 3.10: Buncher circuit. From the generator **G** to the coil **C** the system is equivalent to the one of the funnel. Additionally, a resistor chain with resistors **R0**, **R1**, and **R2** is added which is fed by the DC gradient voltage connector **gvc**. The last five electrodes are connected to the closing voltage connector **bvc**. The RF is coupled into the resistor chain by the capacitors **X**.

3.4.3 Electric circuit of the buncher

The signal for the buncher is produced in a similar way as the funnel. It uses an identical balun transformer **B1**, resistor **R**, and resonance circuit formed by the coil **C** with the connected cables and the electrodes **E**. In contrast to the funnel, the buncher needs a DC gradient additionally to the RF signal and the possibility to quickly switch the voltage of the last electrodes between a blocking voltage and a release voltage. The DC gradient is created between ground and $-3.2\,\mathrm{V}$ applied to the gradient voltage connector **gvc**. The voltages are defined by a resistor chain of $20\,\mathrm{k\Omega}$ resistors **R2** after an initial resistor **R0** of $120\,\mathrm{k\Omega}$ producing a gradient ranging from $-1.6\,\mathrm{V}$ down to $-3.2\,\mathrm{V}$ in steps of $-0.064\,\mathrm{V}$ per electrode. The first resistor of the green phase **R1** has a resistance of $10\,\mathrm{k\Omega}$ to produce a constant gradient along the buncher. The RF signal is coupled into the connection to the electrodes via 220-pF capacitors **X**. The first electrode of the buncher and the last five electrodes, which will be used to close the longitudinal trap of the buncher, are not connected to the RF signal. Instead, the last five electrodes are directly connected to the

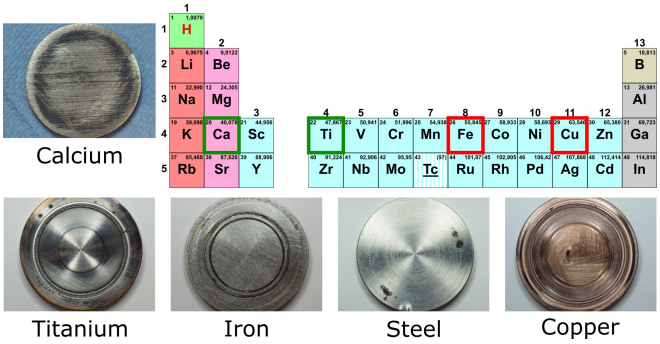

(a)

(b)

Figure 3.11: Targets and ablation plumes:
a) Targets of the elements of interest and the periodic table. The elements that have been used for spectroscopy are marked in green, while those where only ion beam production has been shown are marked in red.
b) The black and white picture shows an ablation plasma as a bright withe spot in the middle. In the inset a blue shining plasma sphere ignited in air is depicted.

blocking voltage connector **bvc**. In non bunching operation these electrodes will be set to the same voltage of $-3.2\,\mathrm{V}$ as the gradient voltage connector **gvc**. All 25 signals for the 25 electrodes are fed through a D-sub 25 pin connector **D1** integrated into the vacuum flange. There they are connected to the electrodes **E** via a flat ribbon cable as described in Sec. 3.3.3.

3.5 Laser ablation and funnel characteristics

Before the ion source was used for laser spectroscopy its working parameters were optimized and its operation behaviour investigated. Results are presented in the following section.

3.5.1 Selection of target materials

Laser ablation is a process that can vaporize and ionize a huge variety of elements (see Sec. 2.5). To test the ion source with different materials, four elements and one alloy were chosen as target material, which are depicted in Fig. 3.11 a. Calcium was chosen to specify the presented laser ablation source since several measurements were performed with Ca already at the COALA beamline with different ion sources [4], [24], [54], [55], [110]. It will allow to compare the characteristics of this ion source with other models. Titanium and iron are two elements that are of interest for astrophysical research [11] and nuclear structure investigations as explained in Sec. 1 and where the relevant transitions are accessible with the COALA laser system. Those two metals as well as copper are transition metals that cannot be efficiently ionized in surface ionization sources due to their relatively high ionization potentials with respect to the work function of the ion-source material. Steel is an alloy of several transition metals and can give an insight into the production capabilities of this ion source. Using alloys can be key to expand the production to elements that can not be shaped into a solid target.

3.5.2 Size of the ion cloud

The pictures in Fig. 3.11 b show laser generated plasmas. In the top left corner one can see a blue sphere that was formed by focusing a laser pulse in air. The plasma expands in all directions equally until the expansion is stopped by the surrounding gas. The bright white and blue light is a sign of very high temperatures created inside the plasma. The black and white picture was taken at an early test setup with a triggered video camera[5], looking through a viewport onto a steel target inside a vacuum chamber. The camera was triggered by the Q-switch of the ablation laser and recorded one frame. One can see a tested steel target inside of a vacuum chamber through a viewport. Depending on the background pressure inside the chamber, the visible plume changes in size. Additionally, the plume-size varies with the change of the ablation laser pulse energy. Varying the pulse energy between 2 and $26\,\mathrm{mJ}$ and the background pressure between 15 and $400\,\mathrm{mbar}$ leads

[5] Allied Vision Prosilica GC655

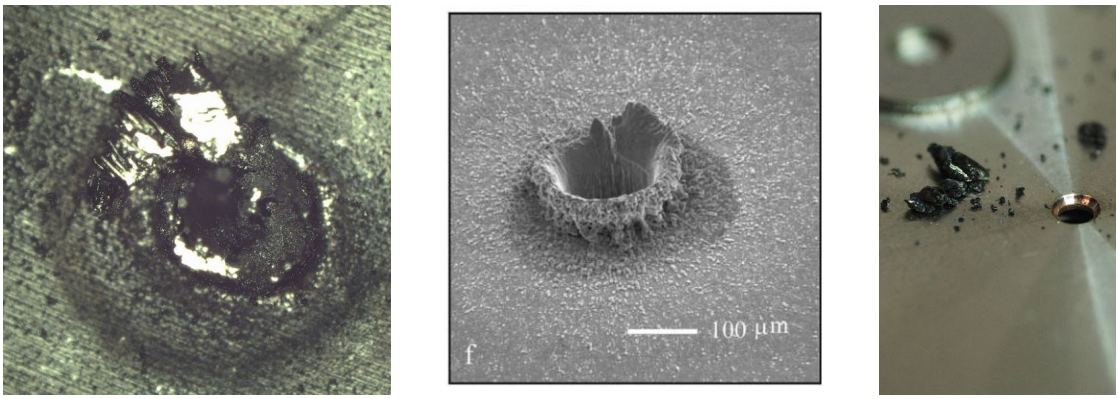

(a) (b) (c)

Figure 3.12: Traces of ablation processes:
a) Microscope picture of an ablation crater-rim from the steel target. The white surface is material that scraped against the middle part of the ablation chamber. b) Scanning electron microscope picture of an ablation rim structure from [113]*.
c) Material from the ablation process that clogged the second nozzle which can be seen next to it with a $1\,\mathrm{mm}$ diameter.
(b) reprinted from Optics & Laser Technology, vol. 33, L. Tunna, A. Kearns, W. O'Neill, and C. Sutcliff, Micromachining of copper using Nd:YAG laser radiation at 1064, 532, and 355 nm wavelength, page 141, Copyright (2001) Elsevier Science Ltd, with permission from Elsevier.

to a variation of the visible plume size from a few mm up to about $10\,\mathrm{mm}$ in diameter [111]. Measurements with different laser-pulse energies at the ablation chamber of this source showed that an optimal plume size for this pulse-energy range was reached at $50\,\mathrm{mbar}$ [112].

3.5.3 Ablation process

Using ns laser pulses introduces a significant amount of heat into the material during the ablation process as discussed in Sec. 2.5. In Fig. 3.12 a this can be seen by the effect of molten steel building a crater-rim like structure around the created hole. One can see an area around the hole in the target which has a slightly changed color to the unmodified

(a) (b) (c)

Figure 3.13: Measurements of the laser focus:
a) Microscope image of a whitened spot on a burn paper after illumination through the 36-mm lens in the lens target distance. The lines indicate the horizontal width for the larger grey spot and the smaller beige spot. The uncertainty is in all cases $\pm 10\,\mu\mathrm{m}$.
b) The red arrows mark the width of the channel burned into the target surface by the 175-mm lens.
c) The small black line is the channel burned into the target by the 36-mm lens.

target surface, which is the heat-effected zone. The shiny part of the picture is the molten steel that was tossed up during the phase explosion of the liquid metal and solidified in this position (compare Sec. 2.5). This effect can be seen more detailed in the SEM picture in Fig. 3.12 b taken from [113]. The height of this structure is of macroscopic size as the shiny flat top implys. While the whole formation has an irregular shape the flat top shows that the crater rim has grown up to a height where the top scratches along the surface of the ablation chambers middle part. This illustrates the amount of material that has been ejected during the ablation process.

3.5.4 Laser spot size

As described in Sec. 3.3 two different lens positions were used. The position outside of the vacuum chamber required a focal length of $175\,\mathrm{mm}$ while inside the vacuum chamber a lens with a shorter focal length of $36\,\mathrm{mm}$ was used. For the latter case the laser spot

size was measured with burn paper[6] shown in Fig. 3.13 a with one laser shot at 15-mJ pulse energy. The burn paper shows a circle with two shadings. This gives a very rough representation of the energy distribution along the beam radius. The outer diameter is measured to be $180\,\mu\mathrm{m}$ while the inner diameter is between 90 and $100\,\mu\mathrm{m}$. On the target the permanent rotation during the ablation forms a channel on the surface. The width of the surface channels of both laser foci was measured by a calibrated microscope with the results shown in Fig. 3.13 b (175 mm) and c (36 mm). The diameter of the beige burn paper circle from the 36-mm lens fits well with measured channel width on the target. Both measurements are not exactly representing the nominal focus diameter but can give a good estimate and agree well in the result. The channel measurement with the larger beam diameter results in a width of about $400\,\mu\mathrm{m}$. Hence, the spot diameter could be decreased by a factor of 4 by using the shorter focal length. For the energy density that gives an enhancement by a factor of 16, hence, by more than an order of magnitude higher.

The results from [83] showed that the ion to neutral ratio produced by the laser ablation process increases with increasing power density at the focal spot. There, lowering the power density was done by enlarging the spot area of the focus while keeping the pulse energy constant. The number of neutrals produced did not change significantly with the change of the focus diameter but the number of ions was decreased by half an order of magnitude. This leads to the conclusion that a high power density is more important for producing large amounts of ions via laser ablation than a large illuminated area. This is supported by the experiences in this work where the deposition of ejected material (see below) was less for the smaller focal spot than for the larger one without noticeable reduction in the ion output.

3.5.5 Ion current stability

After the installation of the ion source at the COALA beamline which will be described in more detail in Sec. 3.6, the produced ions could be tuned through the beamline. The

[6] ZAP-IT Laser Alignment Paper

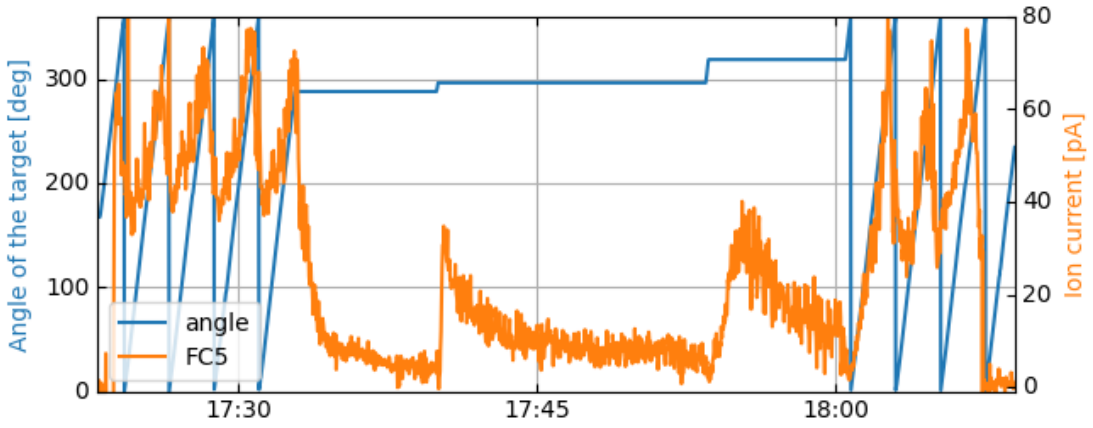

Figure 3.14: Ion current fluctuations during source operation. In orange, one can see the ion current measured at FC5 in the COALA beamline behind the extraction from the ion source. In blue, the rotation position of the target is shown (modulo $360°$), clearly correlated with the ion current. When the rotation is turned off, a fast decay of the signal can be seen.

amount of produced ions was most of the time monitored by Faraday cups connected to a pico-amperemeter[7]. This device measures an average current over several ion bunches produced by the laser ablation ion source over a time frame of about $1\,\mathrm{s}$. In Fig. 3.14 the ion current detected at FC5, placed $5\,\mathrm{m}$ downstream the beamline, directly behind the optical detection region where laser spectroscopy will take place, is depicted.

In Fig. 3.14 the rotation angle of the target is shown in blue and the measured ion current in orange. The laser had a repetition rate of $50\,\mathrm{Hz}$ and the target was rotated with one step per laser pulse. The amount of ablated ions was fluctuating over a range of up to 50% of the total signal when the target was rotated as one can see in the graph before 17:30. Besides those short-term (minutes) fluctuations also long-term drifts have been observed. One long-term change is the decrease of the ion signal due to crater creation on the target. This effect was tested between 17:30 and 18:00 for three fixed target positions. It shows a very strong decrease in the signal in the first 5 minutes and stabilizes into a

[7] KEITHLEY 6485 PICOAMMETER

slow linear decrease after corresponding 15000 shots. The remaining ion current is about one order of magnitude lower, which is too low for efficient reference measurements of stable isotopes. For this reason, it is recommended to move the target by one step after each ablation pulse. This keeps the ion production on a higher rate, but fluctuations that are clearly correlated with the target rotation are still observed. The signal varies between $50\,\%$ and $100\,\%$ during one evolution of the target which took 2 minutes and 6 seconds. For the spectroscopy measurements which are typically performed on a time scale of a few minutes this can lead to significant asymmetries in the line shape due to the varying signal intensity. These strong fluctuations were considerably reduced by a less stiff connection between the rotary feedthrough and the target holder and the influence on the spectra finally diminished by a sufficiently long signal integration time with many rapid scans in alternating directions across the resonance signal.

Furthermore, the ablation process itself has an intrinsic variation as it is a chaotic process. Even if the target position is held constant the signal varies. This can be seen between 17:45 and 17:50 when the laser hits always the same spot. Those fluctuations are on the timescale of seconds and even out statistically during a measurement but still lead to increased scatter and statistical uncertainty in the laser spectroscopy measurements.

Another possible source of fluctuations is the periodically changing ablation-laser pulse energy that shows a period of minutes. This does, however, only appear when the repetition rate is much lower than the maximum repetition rate of $100\,\mathrm{Hz}$. At repetition rates between 50 and $100\,\mathrm{Hz}$ the effect is negligible.

3.5.6 Material deposition at the funnel

The extrusion of macroscopic amounts of material in the laser ablation process as witnessed in Fig. 3.12, strongly affects the long-term operation of the funnel. How the material is deposited on the funnel electrodes turned out to depend strongly on the target material. Ablating a copper target led to an evenly distributed fine coating around the center holes of the electrodes. Calcium created cone-shaped walls around the center hole of the electrodes that grew until they filled the gap between neighbouring electrodes which can be seen in

Fig. 3.15 a and b. At first, this changes the gap size for the helium leaving the funnel, but finally, the material creates a short circuit between the two RF phases, switching off the RF-fields. At this point the delivered ion current from the source decreases instantly.

Ablating iron produces a less even growth of material on the electrodes but more filigrane structures sometimes like fibers shown in Fig. 3.15 c. Those structures do not clog the gas flow but establish even faster short circuits between the electrodes. Titanium also grows cone-shaped walls like calcium but at a much slower rate. Nevertheless, titanium sometimes tosses larger droplets or pieces into the funnel clogging all transmission trough the second nozzle like in Fig. 3.15 d.

3.5.7 Buncher accumulation tests

Measurements using only the last electrode of the buncher to block the ions from leaving through the exit hole showed that even for blocking-voltages up to $100\,\mathrm{V}$ the ions could not be blocked completely. SIMION simulations indicated that this could origin from the HV extraction field reaching into the space inside the last 3-4 electrodes. After connecting the last five electrodes directly to the blocking voltage connector, all ions could be stopped from leaving the buncher through the exit electrode with a blocking voltage of $+9\,\mathrm{V}$. Tests to measure ions after using the last electrodes to close the buncher for $1\,\mathrm{ms}$ and $2\,\mathrm{ms}$ accumulation time did not show any signal increase after reopening the funnel. This could be caused either by loosing the ions inside the buncher completely or by a storing capability of a small number of ions, which can not be resolved by the used detection system. Accumulating the ions to shorter bunches offers a significant increase in the signal-to-noise ratio for collinear laser spectroscopy and should therefore be investigated further in the future. A magnetof detector, capable of detecting even single ions, is in preparation but could not be used during this work.

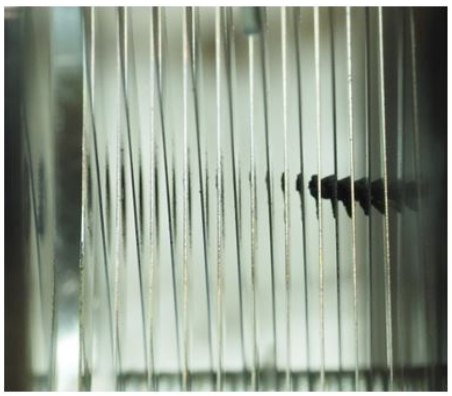

(a)

(b)

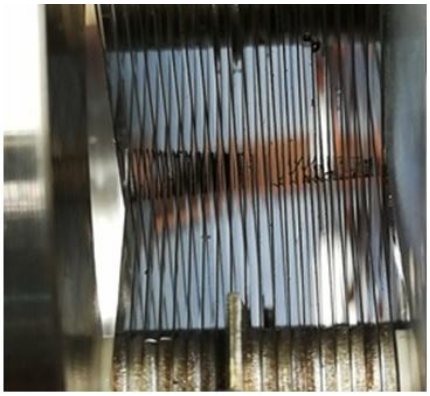

(c)

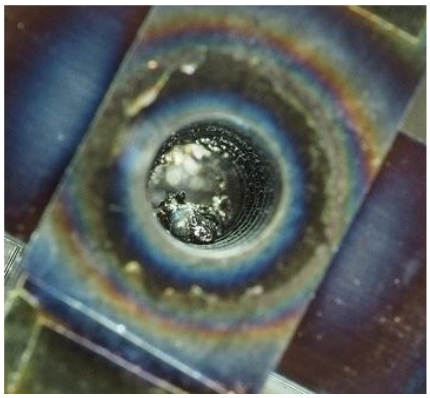

(d)

Figure 3.15: Material deposition inside of the funnel for different materials. a) shows the crater-rim like structures building around the central hole of the funnel which are shown in detail on a single electrode in b). c) shows the wire like depositions that caused short circuits using an iron target. d) shows the large lumps of titanium inside of he funnel

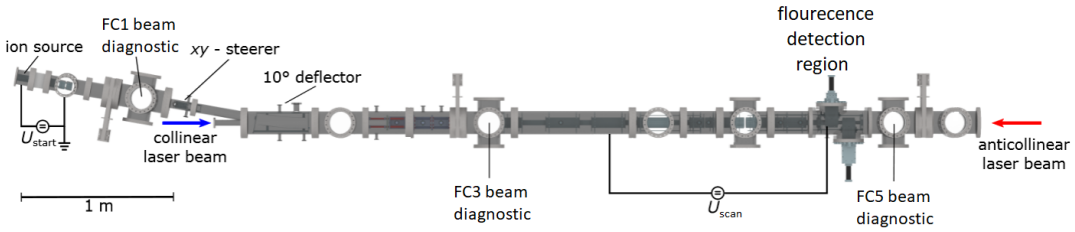

Figure 3.16: Schematical layout of the COALA beamline. The ions are created at the ions source and accelerated into the beamline. The different diagnostic stations are equipped with the named Faraday cup (FC). The $10°$ deflector superimposes the ions with the laser beam. The fluorescence detection region can be floated with the scan voltage and can be equipped with two PMTs.

3.6 COALA

The TIMS ion source described above is designed to work as a versatile ion source for collinear laser spectroscopy. To perform first measurements with the ion source and to characterize its properties, it was connected to the Collinear Apparatus for Laser Spectroscopy and Applied Science (COALA) at TU Darmstadt[110].

3.6.1 Beamline and ion transport

The COALA beamline shown in Fig. 3.16 is instrument for collinear laser spectroscopy experiments at the Institute for Nuclear Physics at TU Darmstadt. It is 7 meters in length and can provide vacuum conditions down to 10^{-9} mbar. In Fig. 3.16, the ion source is placed at the top left end of the beamline and is positioned in a high voltage cage. An insulating transformer provides electricity to all devices located at the ion source while the whole ion source can be floated on a high voltage potential of up to $20\,\mathrm{kV}$ wheras the beamline is on ground potential. The ions are extracted by a skimmer cone and directly afterwards collimated by an einzel lens. At three positions along the beamline diagnostic stations are positioned which are shown in Fig. 3.17. These stations are equipped with a phosphor screen, a Faraday cup, and an iris. The phosphor screen is designed for

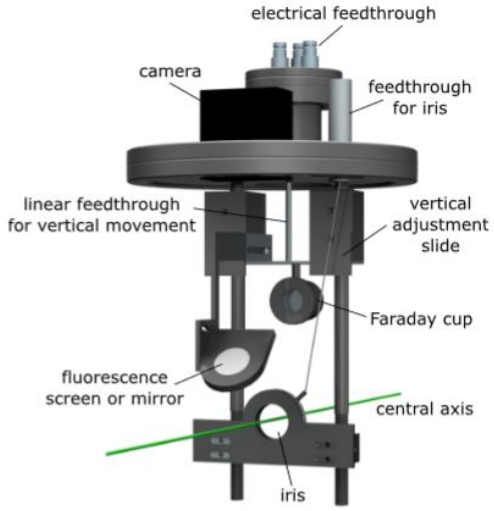

Figure 3.17: Beam diagnostic station with iris, Faraday cup, and phosphor screen. The iris defines the central axis of the ion beam and the laser beam and can be changed in diameter from outside the vacuum chamber. The Faraday cup and the phosphor screen are mounted on a vertical translation stage to be moved into the beam. The cup is used to measure the ion current that is transmitted through the iris and the phosphor screen can be used to monitor the ion beam shape via a viewport with a camera.

continuous ion beams of at least several nA ion current and was not sensitive enough to display the pulsed ion beam from the laser ablation source. The Faraday cup signal on the other hand could be amplified by a transimpedance amplifier and measured time resolved with an USB oscilloscope[8]. After the first diagnostic station, the ion beam can be corrected in vertical and horizontal direction with an electrostatic xy-steerer. An electrostatic 10° deflector is used to bent the ion beam onto the central axis of the spectroscopy beamline where it can be further adjusted in direction and shape by another xy-steerer pair followed by a quadrupole doublet. The irises of the second and third beam diagnostic stations define the axis for the ion and the laser beam. The distance between the two irises is $2.6\,\mathrm{m}$ reducing the uncertainty of angular misalignment of the order of mrad and below, depending on the beam quality. The laser beam can enter via two slightly tilted windows at the beginning and the end of the spectroscopy part of the beamline. This enables laser spectroscopy both in collinear and anti collinear direction simultaneously. The fluorescence detection is placed between the two diagnostic stations. It can be floated by a small variable voltage which allows to perform Doppler tuning (see Sec. 2.1.3) to scan across the resonance frequency. In this case, fluorescence light is emitted from the excited

[8] Picoscope 6000

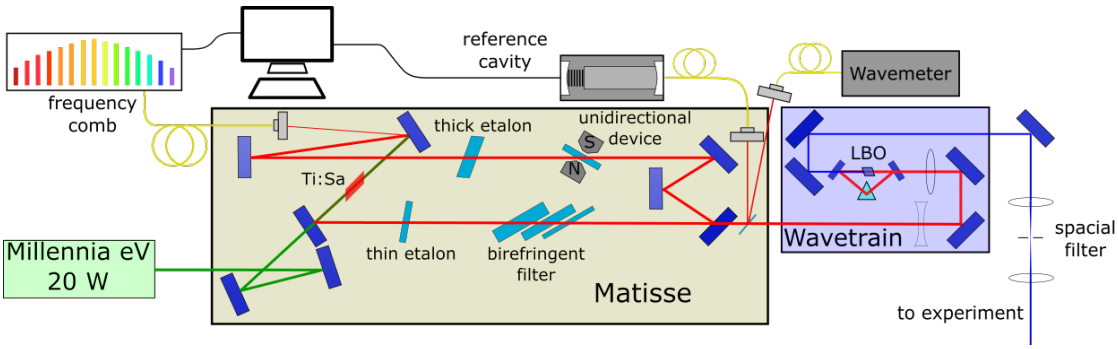

Figure 3.18: Laser sytem used at the COALA laser lab. The Matisse Ti:Sa is pumped by a 20 W Nd:YAG laser and some light is coupled out for stabilization to the frequency comb, the reference cavity and the wavemeter. The main part of the light is frequency doubled in a wavetrain and then guided through a spatial filter towards the experiment.

ions, which is collected with mirrors and guided to photomultiplier tubes (PMTs) [64]. The Doppler tuning and data acquisition is performed with the program TILDA, described in detail in [65].

As the high voltage used to accelerate the ions has a direct influence on the measured transition frequency, it is recorded by a high-voltage divider calibrated to a precision of 3 ppm. The high voltage is generated by a high-voltage supply[9] that needs several hours to stabilize after restart. Therefore, voltage variations caused by the high-voltage supply are counteracted by an additional regulated 5-V supply located below the high voltage platform.

3.7 Laser System for Collinear Laser Spectroscopy

The laser system used at COALA is shown in fig. 3.18. A titanium sapphire (Ti:Sa) ring laser[10] (Matisse) produces laser light from 662 to 1050 nm with several W output power depending on the wavelength. It is pumped by a frequency-doubled Nd:YAG Laser[11] with

[9] Heinzinger PNChp 20000-10 po
[10] Sirah Lasertechnik: Matisse 2 TS
[11] Spectra-Physics: Millennia eV 20 W

up to $20\,\mathrm{W}$ output power at 532 nm. The wavelength of the Matisse is selected by several optical elements. The first wavelength selection is done by the mirror coatings used in the ring cavity. A birefringent filter, a thin etalon, and a thick etalon restrict the laser to single-mode operation. The laser frequency is stabilized by side-of-fringe locking to an external cavity. Frequency fluctuations are compensated by adjusting the path length of the Matisse ring cavity through adpting the position of one mirror with a fast piezo. For long-term stabilization of the frequency either a wavelength meter[12] with relative frequency stabilization of several $100\,\mathrm{kHz}$ but with an absolute uncertainty limited to several MHz or a frequency comb[13] for high-precision absolute stabilization can be used.

To generate laser light also at shorter wavelengths, second harmonic generation is employed in a cavity-based frequency doubler[14] is placed behind the Matisse. Here the laser light is coupled into an enhancement cavity with a focus inside of a non-linear crystal. The frequency-doubled light after the wavetrain is a Gaussian beam with fringes from the doubling process. Therefore, a spatial filter is placed behind the wavetrain to remove the fringes and generate a TEM00-mode beam. Alternatively, a single-mode fiber can be used as long as the laser wavelength is not too short for efficient fiber transport. Both methods were applied for the measurments described in this work.

Production of 338-nm light

Producing light to drive the 338-nm transition in Ti^+ is challenging for the Matisse laser system. It is right at the edge of the specified range of the Ti:Sa ($676\,\mathrm{nm}$) resulting in a low efficiency. Hence, the 676-nm mode is not that significantly enhanced compared to modes at longer wavelengths that are suppressed by the optical elements inside the cavity. To reduce the chance of multimode operation, one mirror ('Slow Piezo Mirror') was exchanged from a Ti:Sa mirror to a dye laser mirror (MOS 4) which inhibits wavelengths larger than $676\,\mathrm{nm}$ due to its coating which is optimized for wavelengths between 550 and $660\,\mathrm{nm}$.

[12] HighFinesse: WSU-30
[13] MenloSystems: FC1500-250-WG
[14] Sirah Lasertechnik: Wavetrain 2

4 Results

After the first tests described in the previous chapter, ion beams generated with TIMS where used for collinear laser spectroscopy. First experiments were performed to characterize the ion source and compare it to other sources that were previously operated at COALA. Therefore, calcium was the ideal element since Ca^+ ions offer a fast transition from the ground state at a wavelength of 393 nm, which is easily produced by second-harmonic generation of the Ti:Sa laser light. Moreover, there is considerable experience with this transition from other experiments at COALA [4], [24], [54], [110] allowing for a direct comparison with the characteristics of various other ion sources. The frequency spectrum and the time structure of the collinear laser spectroscopy signal is analyzed. The frequency spectrum revealed a strong effect of RF-heating on the velocity distribution of the ions, which was eliminated by an adaption of the bunches electrode structure. The results are compared to laser-ablation sources which were operated previously at COALA without buffer-gas cooling, to analyze the influence and performance of the cooling process and how far it can compete with surface ionization sources that can deliver ion beams of excellent quality.

The second part focuses on laser spectroscopy of titanium ions. Isotope shifts and transition frequencies were determined for several transitions and their consistency was checked with a King-Plot procedure. The measurements provide clear criteria for the usability of the different transitions in nuclear structure investigations of short lived isotopes at online facilities.

4.1 Source characterization with Ca

With respect to the ion source characterization, collinear laser spectroscopy offers a unique sensitivity to the longitudinal emittance of an ion beam produced from the source. The longitudinal energy distribution is directly accessible as the broadening of the spectral line, as described in Sec. 2.1.

Here, the ion beam and the laser beam were aligned in anticollinear direction, which corresponds to $\cos(\alpha = 0)$ in Eq. 2.4 described in Sec. 2.1.1. Depending on the exact settings, the ion beam diameter is somewhat between 3 and $10\,\mathrm{mm}$ while the laser beam diameter is about $2\,\mathrm{mm}$. The platform potential of the ion source was set to $14\,\mathrm{kV}$ and the ion source was equipped with the 0.6-mm nozzle, producing ion bunches of about 1-ms length. The ablation laser was used with a repetition rate of $50\,\mathrm{Hz}$ and the target rotation was set to 50 steps per second which provided a new spot for every laser shot. The laser energy was set to $1.25\,\mathrm{mJ}$. This laser energy, in combination with the $f = 36\,\mathrm{mm}$ lens, corresponds to a fluence of 1.6 GW/cm^2. This is just slightly above the ablation threshold of 1 GW/cm^2, reducing the wear of the target. The RF of the first funnel and the buncher was set to $5.5\,\mathrm{MHz}$ and the RF amplitude for the first funnel was $32\,\mathrm{V_{pp}}$ and for the buncher $8\,\mathrm{V_{pp}}$ if not otherwise specified.

For the specification measurements the 397-nm transition in $^{40}Ca^+$ ions, described in Sec. 2.4, was used. Resonance signals were recorded by Doppler-tuning at the optical detection region as described in Sec. 2.1.3 and time-resolved fluorescence spectra taken with the TILDA data acquisition. The beam current is monitored with the Faraday cup FC5 behind the optical detection region.

4.1.1 Spectrum of Ca^+

In Fig. 4.1 a typical time-resolved resonance measurement is depicted. In the center, a density plot of the observed fluorescence light is shown with the total voltage between source and optical detection region on the x-axis and the time on the y-axis. The time

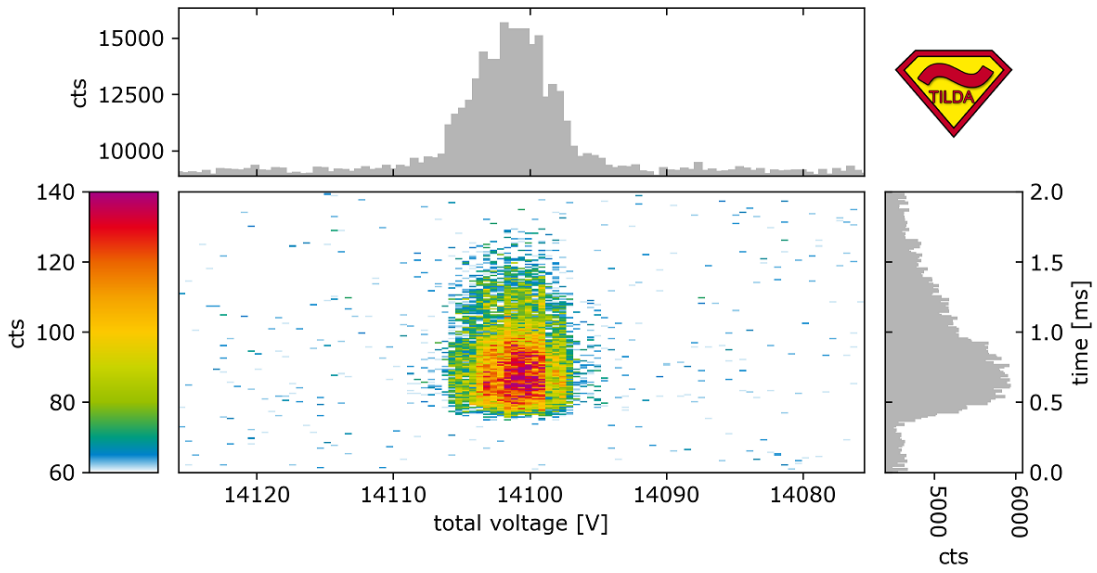

Figure 4.1: Typical signal of a time-resolved bunch spectrum from the collinear laser spectroscopy setup. The 2D-histogram plot shows the time-resolved (y-axis) over the scanned total acceleration voltage. The upper graph shows the projection of the signal onto the x-axis, which represents the resonance signal, whereas the time projection on the right provides information on the time structure of the extracted beam. The color coding is offset to fade out the relatively homogeneous background. For details see text.

is relative to the Q-switch signal of the ablation laser. The horizontal extension of the resonance signal in the colored 2D-histogram plot shows the spectral width of the signal, which correlates to the ions energy spread from the source, while its vertical width represents the duration of the ion bunch. The homogeneous background signal of about 60 counts per bin over the whole plot is offset to white, to enhance the visibility of the signal shape. The plot above the 2D-histogram shows the projection of all data points onto the x-axis, which is the total voltage between the ion source and the optical detection region. For a given mass, this voltage can be converted to a corresponding Doppler shifted frequency observed by the ion in its rest frame, as explained in Sec. 2.1. Hence, in further plots, when the observed ion species and mass is known, this axis will be transformed to the observed frequency and subtracted by the corresponding literature transition frequency.

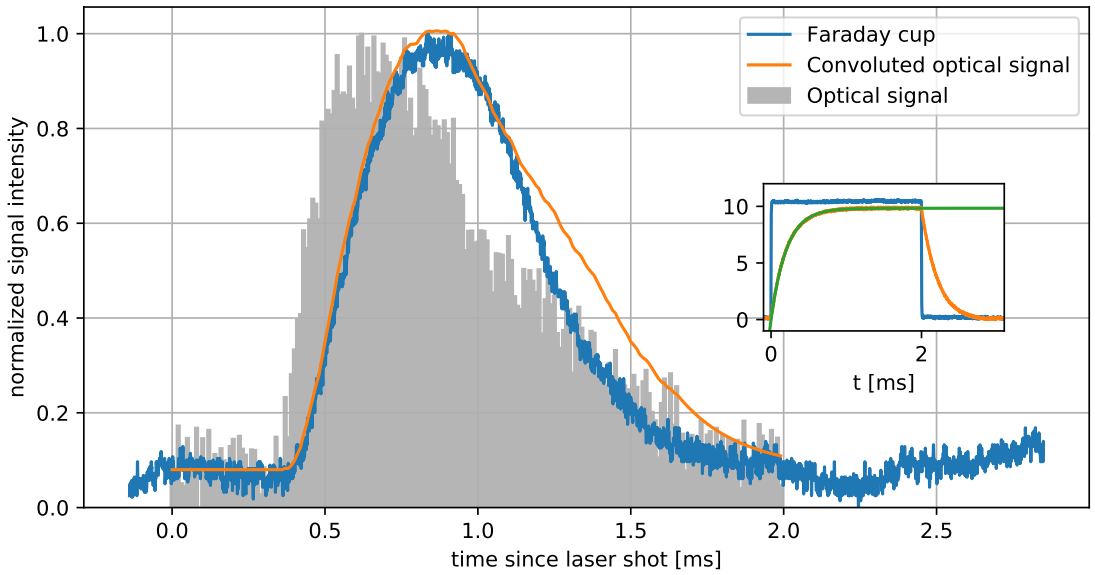

Figure 4.2: Comparison between fluorescence and electrical signal. The blue signal is the current measured at the Faraday cup. The grey signal is the time projection of the fluorescence signal detected from the Ca^+ transition. The orange curve is the convolution of the optical signal and the impulse response function of the TIA behind the Faraday cup. It shows that both signals agree in the overall shape. In the inset the step function is shown in blue and the response signal from the transimpedance amplifier (TIA) in orange. The green curve is the fitted step-response curve.

This allows to directly see the frequency deviation of the measured data from the literature value. Also, the line fits were performed on the frequency axis. On the right, the observed fluorescence is projected onto the time axis, allowing to observe the temporal shape of the resonance.

In Fig. 4.2 the temporal shape of the signal measured on Faraday cup FC5 is shown in blue and compared to the time-projection of the fluorescence signal in grey. Both signals are normalized to their maximum value to make them comparable in size. The ion current arriving at the Faraday cup was fed into a transimpedance amplifier (TIA), converted into a voltage signal and then recorded with an oscilloscope[1]. The signal shape corresponds

[1] Picoscope 6000

to the temporal distribution of the ions in the bunch. It should be noted that this signal is independent of the ion species, whereas the time projection in Fig. 4.1 is restricted to $^{40}Ca^{+}$ ions. the bunch arrival is delayed by 0.5 ms relative to the laser shot and the bunch length is about $1\,\mathrm{ms}$. With the acceleration voltage U of $14\,\mathrm{kV}$, the mass m of the ions between 40 and 50 amu and a flight distance s through the beamline of about $6\,\mathrm{m}$, the singly charged ions have a time of flight

$$t = \frac{s}{v} = \frac{s}{\sqrt{\frac{2eU}{m}}} \tag{4.1}$$

between 23 and $26\,\mu\mathrm{s}$. The shape of the time of flight signal is dominated by the extraction from the ion source and it is impossible to resolve different masses within the ion bunch. This prohibits an analysis of the composition of the bunch, which can in principle contain large amounts of ions that are not relevant for the laser spectroscopic investigation like, for example, charged clusters and molecules.

The signal from the optical detection region seems to have an earlier arrival time of the bunch. This discrepancy can be explained by the transfer function of the amplifier used at the Faraday cup [114]. While the optical detection region counts photons with nanosecond-delay time, the transimpedance amplifier has a linear time-invariant transfer function like a low-pass filter. Measuring the step response $h(t)$ and fitting the data to

$$h(t) = K(1 - e^{-\frac{t}{T}}) \tag{4.2}$$

resulted in a time constant $T = 0.2\,\mathrm{ms}$, which is depicted in the inset of Fig. 4.2. K is the amplification factor of the transimpedance amplifier which is in this case $220 \times 10^6\,\mathrm{V/A}$. From the derivative of the step response the impulse response can be calculated

$$g(t) = h'(t) = \frac{K}{T} e^{-\frac{t}{T}} \tag{4.3}$$

and used to generate a comparable signal from the optical detection. Therefore, the optical signal is also convoluted with the impulse response scaled to the maximum of the ion-current signal shown in orange in Fig. 4.2. The result agrees quite well with the

Table 4.1: Width of the fitted RF-broadened spectra. The resulting RF amplitude from the fit is compared with the one read out by the electronics showing a constant screening factor of 0.63.

	FWHM	RF-amplitude Labjack	RF amplitude fit	screening factor
blue	$(55.0 \pm 5.6)\,\mathrm{MHz}$	$0\,\mathrm{V}$(GND)		
green	$(170 \pm 14)\,\mathrm{MHz}$	$(8 \pm 2)\,\mathrm{V}$	$(5.12 \pm 0.60)\,\mathrm{V}$	0.64 ± 0.18
red	$(290 \pm 14)\,\mathrm{MHz}$	$(19 \pm 3)\,\mathrm{V}$	$(12.0 \pm 0.6)\,\mathrm{V}$	0.63 ± 0.10

evolution of the electrical signal, especially in the rising flank. The discrepancy in the falling flank of the bunch can be a hint of a non-uniform distribution of the ion species in the bunch. If the ratio between $^{40}Ca^{+}$ ions and other isotopes or contaminants like clusters or molecules is not uniform over the time evolution of the bunch, the normalization of the signals can lead to the observed discrepancy between curves. Another explanation might be that the ion beam diameter of the ion species distribution in the beam is non-uniform. If, for example, the diameter of the beam is larger at the beginning and reduces at later times, the ratio of ions that contribute to the optical signal will increase and could lead to such a hump in the signal as observed in Fig. 4.2. To get further insight into the composition of the ion bunch, the bunch needs to be sliced into sections of the order of a µs which will then allow to resolve a time-of-flight mass along the COALA beamline. It has recently been shown at COALA that by pulsing an electrostatic component at the beginning of the beamline with a fast switch. For TIMS this can be extended by changing the delay between the laser trigger and the pulse of the fast switch, which would allow us to analyze the composition of every time slice of the bunch. Unfortunately, such a device was not available during this work.

4.1.2 RF-heating

For precision spectroscopy that is not limited by Doppler broadening, a narrow velocity distribution of the ions of interest is necessary. This can be achieved either by cooling the ions or increasing the beam velocity (see Sec. 2.1.2). The buffer gas in the ion source cools the temperature of the ablated ions from several ten thousand degrees [84], [85] down

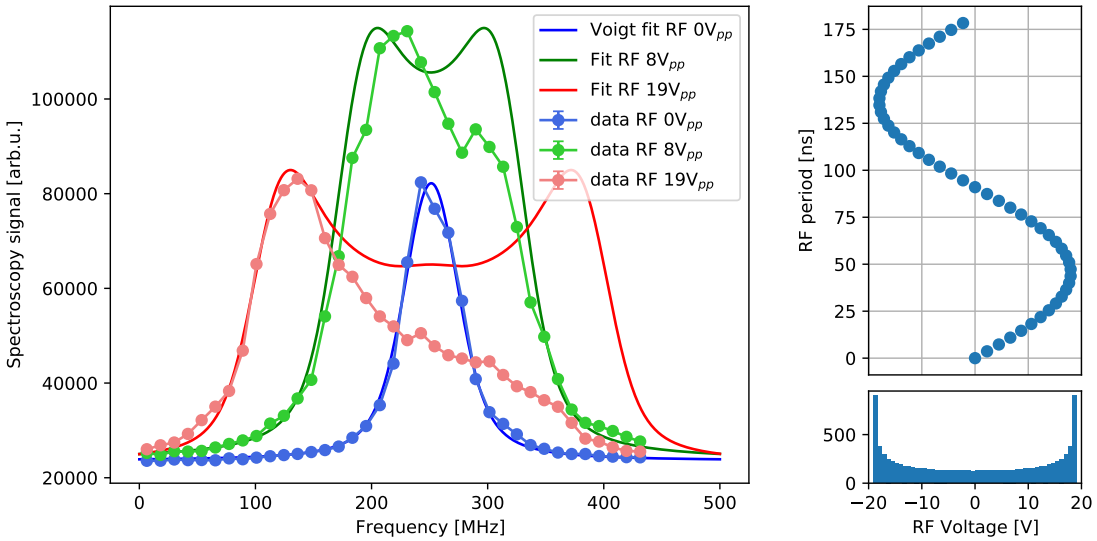

(a) **(b)**

Figure 4.3: RF broadening of the spectra. a) The data points for three different RF amplitudes are shown with the corresponding fit of a convolution of a Voigt profile with the starting potential distribution. b) In the upper graph the RF voltage (x-axis) at discrete time points (y-axis) is plotted and the bar chart below shows the distribution of the time points which is the highest at the maximum RF voltages. Added with the applied HV this is the starting potential distribution.

to room temperature and hence, a low-energy ion beamline (a few keV up to $100\,\mathrm{keV}$) can be used to achieve resolutions that are of the order of the natural line width.

However, additional heating is introduced by the RF that guides the ions, which can counteract the advantages of the buffer gas cooling. To quantify its impact on the longitudinal energy spread of the ion beam, the collinear laser spectroscopy measurements were performed with the same settings as described above but with three different amplitudes of the RF voltage at the buncher. The resulting spectra are shown as projection on the frequency axis in Fig. 4.3 a with the RF amplitude $0\,\mathrm{V_{pp}}$ in blue, $8\,\mathrm{V_{pp}}$ in green and $19\,\mathrm{V_{pp}}$ in red.

For comparison, first the $^{40}Ca^{+}$ spectrum in blue was measured while the RF part of the

buncher was grounded by a $50\,\Omega$ connector and only the DC gradient connected. Therefore, RF-related broadening of the line width was inhibited, allowing to measure the minimal line shape that can be achieved by the ion source without RF heating. The Voigt profile fit yielded a FWHM of $55\,\mathrm{MHz}$ which is about twice the natural line width of $22.3\,\mathrm{MHz}$ (see Sec. 2.4). Next, the settings were tested, which have been used for the ion beam tuning through the COALA beamline. The RF amplitude on the buncher was set to $8\,\mathrm{V_{pp}}$ (green data points) which yielded the highest transmission through the beamline, since the transmission was optimized for those settings. The line width is broadened and the shape cannot be described by a Voigt profile anymore and instead shows a hint of a side peak. The same measurement was performed for the RF amplitude of $19\,\mathrm{V_{pp}}$ shown in red, yielding an even more deformed spectrum.

Nothing was changed on the system besides the RF amplitude, so the influence of a sinusoidal variation of the starting potential was investigated. Since the phase of the 5.5-MHz RF-frequency is not correlated with the ablation laser trigger and several bunches are integrated for each data point in the spectroscopy signal, a temporal resolution of a shifted starting potential by the RF electrodes can not be resolved. For the following, a constant ion current in the buncher during a period of the RF signal ($182\,\mathrm{ns}$) is assumed. In the top chart of Fig. 4.3 b the RF amplitude is plotted in x-direction for equally distanced points in time along one period of the RF signal along the y-axis. The histogram below shows that more time is spent at the maximum and minimum RF voltage. Performing a convolution of the amplitude distribution from the histogram and the distribution from the Voigt fit of the Signal (blue) having no RF influence, results in a distribution with two maxima like the solid green or the red curve. To fit the distribution to the measured data the height of the signal was scaled to the maximum value of the data points and the width of the distribution was fitted to the left flank of the data points. The width is is solely determined by the RF amplitude and the resulting amplitude distribution. The center of the spectrum was chosen to be fixed at the center position of the 0-$\mathrm{V_{pp}}$ RF-measurement. While the resulting curves can follow the overall shape of the data reasonably well on the left side, the peak on the right side shows lower signal for the 8-$\mathrm{V_{pp}}$ (green) data points and even less for the the 19-$\mathrm{V_{pp}}$ (red) data points. The asymmetric shape is likely caused by the transmission through the beamline. The beam tuning was performed by measuring

the ion current on a Faraday cup while the RF amplitude was at $8\,V_{pp}$. With the Faraday cup, only the ion current is recorded and optimized to a peak. Hence, leading to a better transmission for ions from the left side of the spectrum. It is also possible that the laser beam addresses a certain spatial region of the ion beam which favours the ions from the left side of the spectrum. The beamline component that could be responsible for such an asymmetry is the $10°$-bender, which is an electrostatic bender and therefore an energy filter.

The results from the fitted curves are summarized in Tab. 4.1 and compared with the RF amplitudes measured at the ion source. The fit value of the RF amplitude is lower than the one measured by a constant factor of 0.64. During those measurements, the last electrode of the buncher was not connected to the RF since it is designed to serve as a gate electrode for bunching. Simulations of the electric field from the extraction voltage of $14\,kV$ showed that this extraction field penetrates further into the funnel beyond the last electrode. This way, the RF signal of the second last electrode could still add a modulation on the extraction potential which is screened to some degree by the fixed voltage of the last electrode. Since the factor of this screening is the same within its uncertainty for both cases, this indicates that the broadening is correlated to the RF amplitude.

To eliminate this effect, the last five electrodes were disconnected from the RF. SIMION simulations showed that in this case the RF fields and the extraction fields are well separated. Unfortunately, the ion source stopped working at that time. Time restrictions required progressing to measurements with titanium, where the same effects should be observable and its absence would also validate the success of this adaption. The transition investigated in titanium has a comparable natural line width of 22 MHz, as described in more detail in Sec. 2.3 and Sec. 4.2.1. In Fig. 4.4, the FWHM of the spectrum was investigated for various RF amplitudes of both the funnel and the buncher, while the other one was set to standard operation values ($18\,V_{pp}$ for the funnel and $35\,V_{pp}$ for the buncher). For both devices, one can identify a slight rise of the FWHM with higher RF amplitudes. Compared with the variations that can be observed at the standard operation values, this inclination is negligible. This result shows that disconnecting the last five electrodes from the RF of the buncher did mitigate the RF heating to a degree that is not

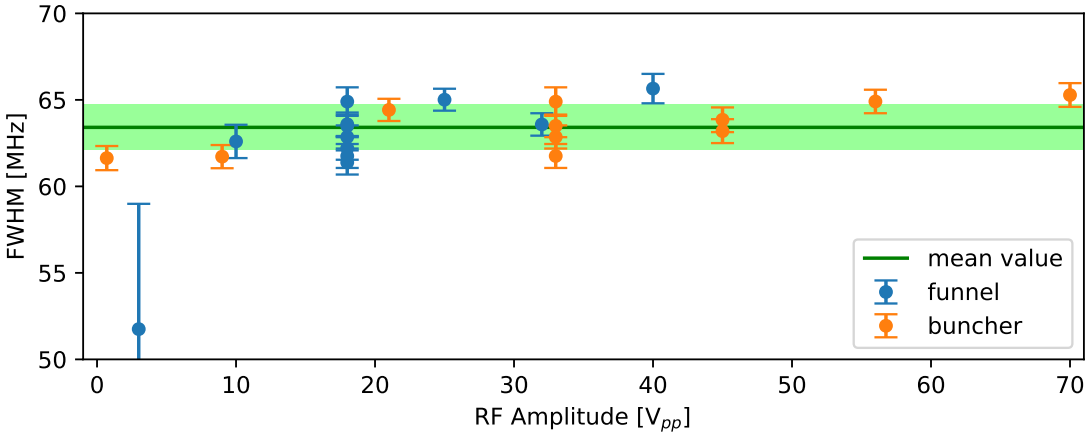

Figure 4.4: Resonance linewidth of the recorded spectra of the $3d^2(^3\mathrm{F})4s\ ^4F_{/} \rightarrow 3d^2(^3\mathrm{F})4p\ ^4G_{/}$ transition in $^{48}\mathrm{Ti}^+$. The FWHM of different measurements is plotted against the RF amplitude that was applied to the funnel (blue) and the buncher (orange) together with the mean value $(63.4 \pm 1.3)\,\mathrm{MHz}$ in green, excluding the funnel value at $3\,\mathrm{V_{pp}}$ because of its large uncertainty.

visible anymore even for RF amplitudes up to $70\,\mathrm{V_{pp}}$.

4.1.3 Effects of buffer gas cooling

To investigate the advantages of the buffer gas extraction, the ion source was benchmarked against other Ca^+ sources that have previously been employed at the COALA beamline. At COALA, laser spectroscopy was performed on a Ca^+ beam generated from three different ion sources so far [24], [54], [110]. The main characteristics that will be compared are the spectroscopic linewidth, which corresponds with the longitudinal energy spread of the ion source, the length of the ion bunch and the center position of the resonances. The latter is possible since a frequency comb is available to stabilize the laser system at well known absolute frequencies.

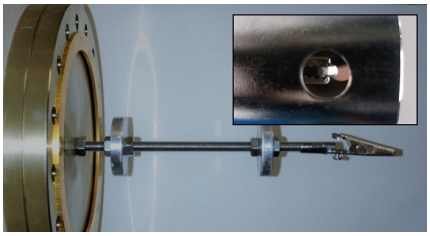

(a)

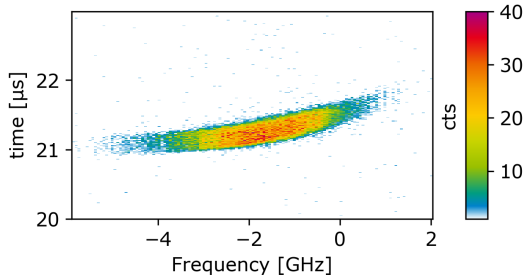

(b)

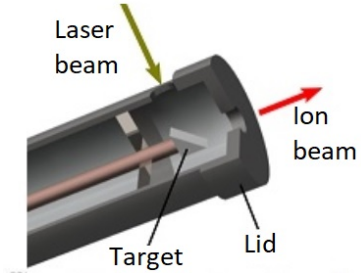

(c)

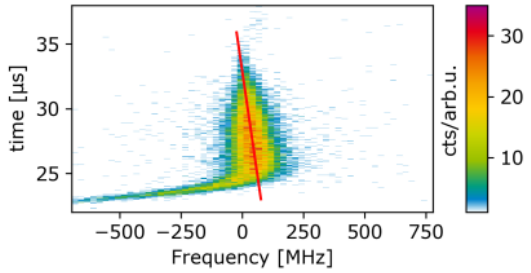

(d)

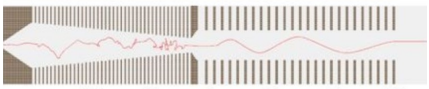

(e)

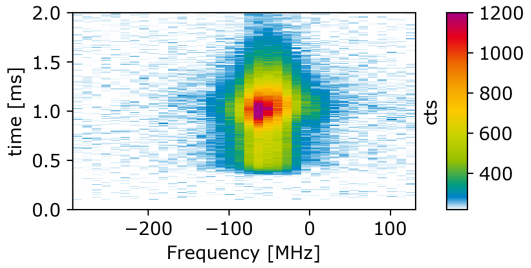

(f)

Figure 4.5: Ablation laser ion sources employed at COALA and their time and frequency spectrum. In the most simple design (a), a clamp holds a piece of calcium which is then ablated with a pulse laser. In absence of a dedicated electrostatic extraction geometry, the energy spectrum of the ions is very broad but the injection into the beamline is almost instantaneous (b). By adding some shielding and an extractor lid (c), the spectrum becomes considerably narrower, but the extraction from the source region takes about an order of magnitude longer (d). Both simple sources show effects of correlation between the arrival time and Doppler shift, which are discussed in [24]. This is not the case for TIMS which is described in this work (e): The spectrum (f) shows the smallest linewidth due to the buffer gas cooling which is also responsible for the two orders of magnitude increase in extraction time and temporal width.

Since the measurements reported in the following were carried out with the non-optimized buncher, the comparison of the linewidth is performed for the resonance taken without RF applied to the buncher. Additionally the linewidth of a titanium measurement is presented which was taken with the optimized setup, having a comparable natural line width of $22\,\mathrm{MHz}$.

In Fig. 4.5 three variants of a laser ablation ion source are shown with corresponding typical spectra. For each ion source, a photo or a schematic is depicted on the left. On the right the corresponding density plot shows the fluorescence intensity as a function of frequency (x-axis) and time (y-axis), While all three variants use laser ablation to produce ions, the first variant has the calcium target inside a tube that is open towards the extraction electrode. The second variant is basically the same design with an additional lid on top of the tube with a small exit hole in the middle. The third variant is the TIMS ion source described in this work with buffer-gas-cooled laser ablation and the extraction through an RF funnel system. In all three cases the calcium target is hit by a laser pulse and the produced ions are accelerated into the COALA beamline (see Sec. 3.6) at similar beam energies. There, the ions are probed by collinear laser spectroscopy resulting in the spectrum shown on the right. The laser addresses only one specific isotope and hence, the recorded spectra only shows the ^{40}Ca isotope. This implies that differences of the time-of-flight through the beamline can only occur due to a different acceleration potential or a delayed extraction. These effects can be separated by the time-resolved spectroscopy signal, since a difference in the starting potential also correlates with a shifted resonance frequency while a delayed extraction with constant starting potential appears always at the same resonance frequency.

In the case of Fig. 4.5 a, a grain of calcium was mounted with a simple clamp and set onto a high voltage potential. The inset shows the calcium grain loaded in the clamp and with a metallic tube around the clamp. In Fig. 4.5 b the resulting spectrum is shown. The temporal width of the bunch is the smallest of all three sources with less than $1\,\mu\mathrm{s}$, since the ablation plume is directed into the transport beamline, and no thermalization of the ions occurs. Accordingly, the energy width is considerably large. A Voigt fit to the spectrum yields a FWHM of $2200\,\mathrm{MHz}$, which is about 100 times the natural line width

and equivalent to an energy spread of $95\,\mathrm{eV}$. This can originate from a field gradient along the ablation plume while the ions are formed. Additionally, also the laser ablation process itself can generate starting energies of the order of several $100\,\mathrm{eV}$ [87] and the target potential can increase by electron emission which is discussed in more detail in [24]. The bunch length is sufficiently short to separate different masses along the time of flight through the beamline. This has been used to demonstrate the usability of the ion source for a wide range of elements [24]. By enclosing the metallic tube with a lid at the end, the exit diameter is reduced from $40\,\mathrm{mm}$ to $10\,\mathrm{mm}$ as shown in Fig. 4.5 c. In this configuration, the time length of the bunch has increased by more than a factor of 10 while the energy spread has decreased by more than an order of magnitude as visible in Fig. 4.5 d. The narrow "fast" tail between 23 and $25\,\mu\mathrm{s}$ still has the width and shape like the signal in Fig. 4.5 b. However the main part of the signal arises from a 10-$\mu\mathrm{s}$ long bunch which has a comparably smaller width of $120\,\mathrm{MHz}$ equivalent to $5\,\mathrm{eV}$. That means that those ions must have been extracted in a "slow" process but then all experienced the same acceleration potential and hence have the same Doppler-shifted resonance frequency. A closer look at the center position of the resonance frequency along the timeline of the bunch shows that there is still a correlation between the center of the resonance and the time-of-flight indicated by the red line in the 2D-histogram plot. In Fig. 4.6 a this has been investigated in detail by slicing this part of the bunch in $2\,\mu\mathrm{s}$ slices. The center position of the resonance frequency decreases by $38\,\mathrm{MHz}$ from the first slice centered at $27\,\mu\mathrm{s}$ to the last slice centered at $35\,\mu\mathrm{s}$ which is about $(5.0 \pm 0.3)\,\mathrm{MHz}/\mu\mathrm{s}$. Additionally, the FWHM of the single slices decreases from $130\,\mathrm{MHz}$ down to about $55\,\mathrm{MHz}$ with increasing time.

In Fig. 4.5 e the TIMS scheme of the buffer gas extraction system is depicted with the path of a single ion colliding with the buffer gas inside of the funnel. The laser ablation in a buffer gas should erase any energy information from the ionization process by the dissipative process of collisions within this gas and provides the ions thermalized to room temperature. The temporal length of the ion bunch of $1\,\mathrm{ms}$ is dominated by the relatively slow extraction through the first nozzle and the funnel which is shown in Fig. 4.5 f. This produces a bunch that is more than a hundred times longer than the one of the ablation with the metal lid, but as expected, the collisions with the buffer gas completely remove the center-frequency-to-time dependence. In Fig. 4.6 b, the temporal evolution of the

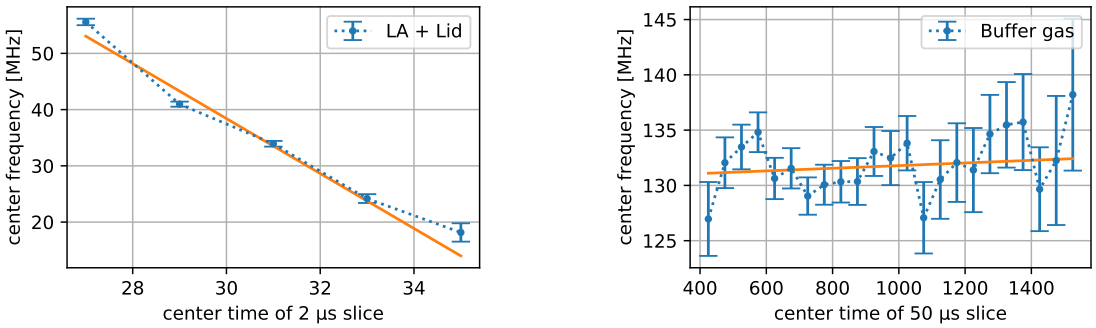

(a) **(b)**

Figure 4.6: Drift of the center frequency along the temporal evolution of a bunch. a) The 2-μs slices of the laser ablation source with the lid drift more than 30 MHz over the whole bunch. b) The center value of the TIMS source shows a variation of about $5\,\mathrm{MHz}$ over the whole bunch length but no statistically significant shift.

center position is shown in detail. In this case only a statistically insignificant drift of about $(1 \pm 2)\,\mathrm{kHz/\mu s}$ is observed. Even though the bunch is much longer, this equals only to a total frequency shift of $<1.3\,\mathrm{MHz}$ over the whole bunch from 400 to $1500\,\mu\mathrm{s}$. It should be noted that this is completely covered by the statistical distribution of the data points and their individual uncertainty. The same analysis has been repeated for titanium with the optimized buncher showing a maximum total frequency shift of less than $5\,\mathrm{MHz}$ over the whole bunch, which is still an order of magnitude smaller than with the lid. As discussed in Sec. 4.1.2, the width of the spectrum shown in Fig. 4.5 f has been measured without RF fields at the buncher, to be about $55\,\mathrm{MHz}$ which is two to three times the natural linewidth and an improvement by a factor of two to the laser ablation with the lid. Measurements of $^{48}\mathrm{Ti}^{+}$ using the optimized buncher yielded a FWHM of $(63.4 \pm 1.3)\,\mathrm{MHz}$. Taking into account that the natural linewidth of the calcium and the titanium transition are both about $22\,\mathrm{MHz}$, this shows an improvement of a factor of two compared to the measurement with the lid.

For most measurements at COALA so far, a surface ionization ion source has been used. This ion source produces a continuous ion beam by heating a graphite tube filled with small calcium grains. As this ion source was used in high precision absolute high-voltage

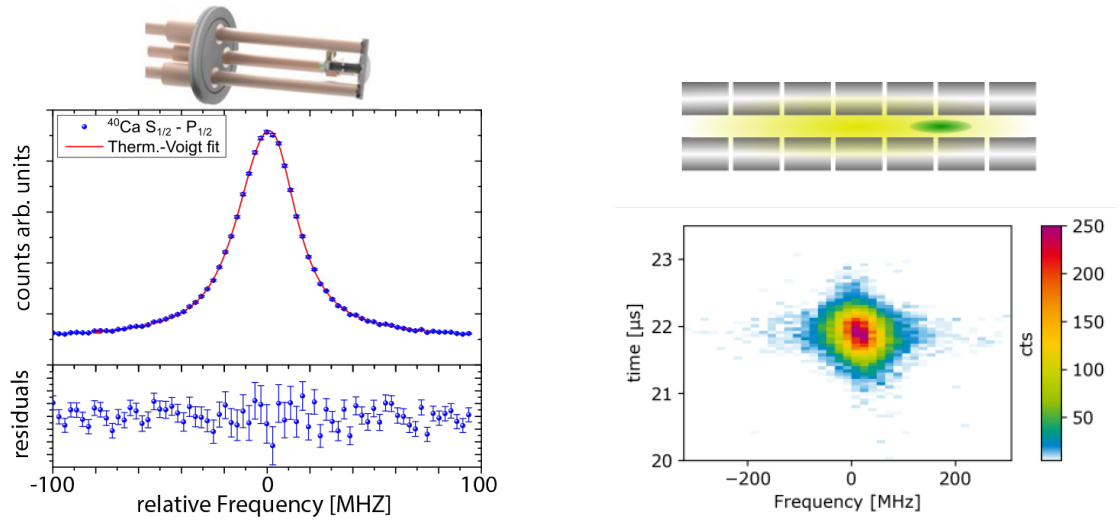

(a) (b)

Figure 4.7: Surface ionization ion source and RFQ cooler and buncher. a) On top the surface ionization source used at the COALA beamline is shown which produces a smooth and narrow line profile with FWHM 30 MHz as depicted below (graphic modified from [110]). b) The schematic on top shows the rods of an RFQ cooler and buncher with the He gas shown in yellow and the ion bunch in green. Below a histogram of collinar laser spectroscopic Ca^+ data is shown. The device produces very short symmetric bunches of the order of 1 µs together with a FWHM of 78 MHz.

measurements [4], [55], it was optimized for producing a stable ion beam with a low energy spread [110]. The continuous beam has no bunch structure, and hence, only the frequency spectrum can be compared. In Fig. 4.7 a, a rendered image of the source is shown with the measured resonance spectrum below. The width of this spectrum is 30 MHz and hence, only 8-MHz wider than the natural linewidth. This shows that there is still about a factor of two of improvement possible for the TIMS ion source.

Another interesting comparison can be performed with ion bunches from the RF quadrupole cooler and buncher, installed at Michigan State University (MSU) [15], [100]. The basic idea of such a device is also to cool an externally injected ion beam with helium buffer gas, accumulate the ions and eject them as a short cooled bunch. The accumulation is especially important for the non-stable isotopes that are produced with much lower rates.

Table 4.2: Spectral width and energy spread of the different ion sources described in this section. The FWHM was determined from a Voigt fit to the data with free width for the Gaussian and the Lorentzian width. The σ value was determined when the linewidth of the Lorentz was restricted to the natural linewidth and describes the standard deviation of the Gauss part of the Voigt. This value was then converted into an energy standard deviation which neutralizes the effects of different acceleration potentials and masses for better comparison. The ion sources are the clamp laser ablation (LA), the clamp laser ablation with the lid (LA + lid), the RFQ cooler and buncher from MSU (RFQ C&B) with $60\,\mathrm{kV}$ starting potential, the TIMS source with Ca and Ti and the surface ionization source.

Ion source	FWHM [MHz]	σ [MHz]	σ [eV]
LA	2547 ± 172	1076 ± 14	46.0 ± 0.6
LA + lid	127.0 ± 4.6	54.4 ± 1.4	2.33 ± 0.06
RFQ C&B (60 kV)	77.7 ± 1.5	29.2 ± 1.1	1.83 ± 0.07
TIMS (Ca)	55.8 ± 5.0	18.2 ± 0.6	0.78 ± 0.03
TIMS (Ti)	62.9 ± 2.7	20.9 ± 1.3	0.83 ± 0.05
Surface ionization	30.9 ± 0.2	6.65 ± 0.05	0.285 ± 0.002

The low rates are compensated by the bunching to allow collinear laser spectroscopy of isotopes with a production of a few ten ions per second for favorable cases.

In Fig. 4.7 b, the schematic drawing of such a device is shown on top with the ion bunch depicted in green. In the histogram, one can see that this device can produce bunches which are of the order of $1\,\mu\mathrm{s}$. The three orders of magnitude shorter bunches allow a much better signal-to-noise ratio as also the time-independent background will be measured only for a µs. When comparing the linewidth, one has to take into account that all measurements that have been performed at COALA were done at a beam energy of 14 - $15\,\mathrm{keV}$ while at MSU a 30-keV beam is used. Therefore, the Doppler-compression is a factor $\sqrt{2}$ larger at MSU. At 30-keV starting voltage a linewidth of $78\,\mathrm{MHz}$ is achieved, which is $110\,\mathrm{MHz}$ if scaled down to a 15-keV beam. This is a factor two broader than with the buffer-gas-cooled laser-ablation source. The larger linewidth can be expressed as an energy-spread of the underlying velocity distribution resulting in a value of $\sigma = 1.83\,\mathrm{eV}$ or FWHM = $4.7\,\mathrm{eV}$ which is in agreement with the values presented in [100]. Nevertheless, the strong advantage of this system is the short bunch length that significantly reduces

the background signal.

In Tab. 4.2 an overview of the values for the five different sources is given. The FWHM was calculated from a fit with no restrictions for the Gauss and the Lorentz part of the Voigt profile. The value σ was calculated from a fit where the width of the Lorentz part of the Voigt was fixed at the natural line width. Assuming that all other broadening comes from a Gaussian distribution, the standard deviation can be used to estimate the energy spread. This energy spread was calculated with the differential Doppler shift depending on the transition frequency and the acceleration voltage and transition frequency. This way the longitudinal energy spread can be estimated without an influence of different starting potentials and transitions.

These results show that the developed ion source is able to produce ion bunches with a clearly improved energy spread compared to the laser ablation in vacuum. Compared to the RF cooler and buncher at MSU, it can produce at least a comparable energy spread, making this source an excellent provider of reference measurements for stable isotopes that can be used for measurements of short-lived isotopes. The comparison with the RFQ cooler and buncher shows especially that introducing bunch accumulation shows a high potential for improvement. Reducing the bunch length will increase the signal to noise ratio significantly, allowing shorter measurement times and better resolution. It also will enable the system to measure even weaker transitions. Finally, the comparison with the surface ionisation ion source shows that there may be some potential to decrease the energy spread further to produce short and narrow ion bunches from a large variety of elements.

4.2 Spectroscopy of Ti

The commissioning experiments with calcium demonstrated the capabilities of the laser-ablation ion source. The advantage of the ion source is that it can produce ions from a variety of elements including the transition metals. One of the candidates of interest for astronomy and nuclear structure is titanium, and here particularly the 338.47-nm transition [11]. Three transitions have been investigated at the COALA setup with the ions provided by TIMS and the results will be discussed in the following sections. The ion source was stabilized to $14\,\mathrm{kV}$ and the RF was set to $18\,\mathrm{V_{pp}}$ at the funnel and $33\,\mathrm{V_{pp}}$ at the buncher. The ablation laser was operated most of the time between 0.8 and $1.2\,\mathrm{mJ}$ at $100\,\mathrm{Hz}$ repetition rate and focused with the f =$36\,\mathrm{mm}$ lens. This led to average ion currents between 3 and $20\,\mathrm{pA}$ at the Faraday cup behind the optical detection region. The current was sometimes stable but more often oscillating around these values. The spectroscopy laser was overlapped anticollinearly with the ion beam and stabilized to the frequency comb except for the first measurements of the $J = {}^5\!/_2 \rightarrow {}^7\!/_2$ (T_{57}) transition. Here the laser had to be stabilized to the wavemeter. The measurements of the $J = {}^3\!/_2 \rightarrow {}^5\!/_2$ (T_{35}) were performed with the spectroscopy laser light transported in fiber, while for the other two transitions the laser light was guided only by mirrors and lenses. To investigate different possible transitions for their usability in collinear laser spectroscopy and to test the setup, three transitions that were in reach with the laser system have been measured from the lowest energy level upwards, which are presented in the next subsection. For all transitions, spectra from all five stable isotopes were recorded. As ^{48}Ti is the most abundant isotope and practically in the center of the stable part of the isotopic chain it has been used as reference isotope for the isotope shifts. For this reason ^{48}Ti has been measured several times in between the other isotope measurements. This allows to monitor drifts of the system and to have reference measurements close to the other isotope measurements which reduces the effect of long-term drifts in the system. This long-term behaviour will be discussed before the isotope shift results are presented. Systematic uncertainties of the measurements are discussed and the results will then be compared to literature values and tested for consistency with the King-Plot method.

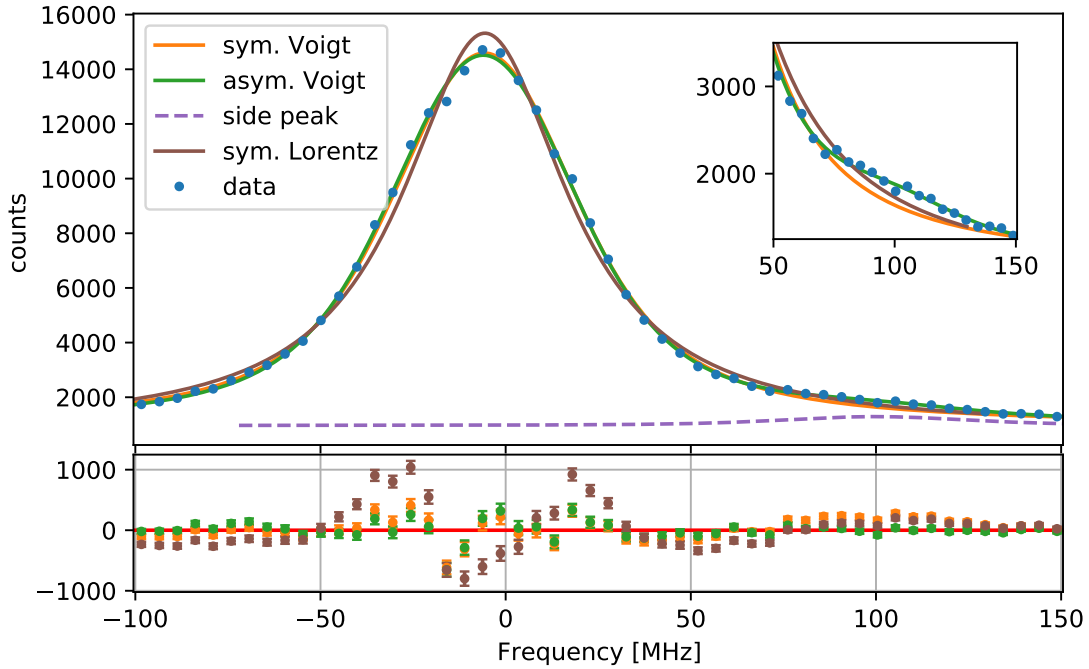

Figure 4.8: Typical spectrum of a ^{48}Ti isotope. Different line shapes have been fitted to the data. The Lorentzian profile shows the strongest deviation. The Voigt and the asymmetric Voigt profile describe the spectrum reasonably well. The asymmetric Voigt performs better with respect to a small side peak at $100\,\mathrm{MHz}$ which is enlarged in the inset.

4.2.1 Spectra of the Ti^+ transitions

The ground state $3d^2(^3\mathrm{F})4s$ from titanium has nine possible fine-structure transitions to $3d^2(^3\mathrm{F})4p$ levels (see Sec. 2.3). Within this work, three of these transitions have been investigated which had the largest transition rates and were accessible by the laser system which are $J = {}^3/_2 \rightarrow {}^5/_2$ (T_{35}), $J = {}^5/_7 \rightarrow {}^7/_2$ (T_{57}) and $J = {}^7/_2 \rightarrow {}^9/_2$ (T_{79}). For each transition, all stable isotopes ^{46,47,48,49,50}Ti were investigated. ^{46,48,50}Ti are even-even isotopes and have a nuclear spin of $I = 0$. The line shape is modelled as the convolution of two broadening distributions, a Lorentzian shape and the Gaussian shape. The first corresponds to the finite lifetime of the upper energy level and the resulting natural linewidth as well as saturation broadening. If the ions have a velocity distribution, e.g. the Boltzmann distribution of a thermal ensemble, the relativistic Doppler effect adds a broadening which leads to a Gaussian distribution around the central frequency. The convolution of a Lorentz and a Gauss curve is called a Voigt curve and is often used to model resonance line shapes. Additionally, effects like collisions with particles and photon recoils can lead to an asymmetric broadening in collinear laser spectroscopy as they effect the ion velocity only in one direction. Asymmetric broadening that is not included in the line-shape model directly influences the center position of a fitted transition spectrum since it shifts a symmetric curve systematically to one side. In Fig. 4.8 a typical ^{48}Ti spectrum is depicted where three different line shapes are fitted to the data. In this graph, the x-axis is transformed from the acceleration voltage to the corresponding frequency seen by the ion. This frequency is then subtracted by the literature value of the transition frequency. This way the transition frequency offset to the literature and the linewidth can be directly extracted from the fit. For a Doppler broadened line, a symmetric Voigt fit (orange) is expected to fit the data well. For comparison a pure Lorentzian shape (dark red) was fitted which struggles to describe the flanks and the top of the data sufficiently. While the symmetric Voigt describes the data already well, at $100\,\mathrm{MHz}$ a consistent deviation between the fit and the data was found wich can be seen enlarged in the inset. For this reason an asymmetric Voigt (green) including a side peak (purple) was fitted to the data. The asymmetric Voigt fit confirms a slight asymmetry yielding a side peak at -4.44(12) eV. Such side peaks can occur in collinear laser spectroscopy and are ascribed to inelastic

collisions with residual gas atoms that lead to electron excitation. The required energy is taken from the kinetic energy of the ion and subsequently irradiated as a photon. In such a case, the ion energy is shifted by the excitation energy and the ions will appear in the spectrum shifted by exactly this amount. For temperatures of the order of $300\,\mathrm{K}$ only the ground state quadruplet is populated in Ti^+ ions. Excitation transitions are possible e.g. to the $3d^2(^3\mathrm{F})4p\,^2G$ doublet (4.28 - $4.26\,\mathrm{eV}$) and the $3d^2(^3\mathrm{F})4p\,^4D$ quadruplet (4.06 - $4.02\,\mathrm{eV}$). This fits well to the observed side peak and might explain its origin.

With respect to the fitted center position, all fit functions agree within $(260 \pm 110)\,\mathrm{kHz}$. This is negligible compared to other systematics that will be discussed below. Hence, the following data analysis is performed with symmetric Voigt profiles but the asymmetry will be accounted for in the systematic uncertainties.

^{47}Ti and ^{49}Ti have a nuclear spin of $I = 5/2$ and $I = 7/2$, respectively, which causes hyperfine splitting. The strength of this splitting depends mainly on the nuclear magnetic-dipole moment μ_I and the magnetic field created by the electron at each energy level B_J which is encoded in the spectroscopic factor

$$A \propto \mu_I B_J. \tag{4.4}$$

Depending on the A factor A_u of the upper and A_l of the lower level, the resulting spectrum can consist of completely separated peaks or several peaks so close to each other that they cannot be resolved. Additionally, the quadrupole moment of the nucleus adds a minor shift to the individual hyperfine components which is taken into account by the B factor B_u for the upper level and B_l for the lower level. One goal of this work was to identify a transition that offers a spectrum with well-separated lines, which can be resolved even in online measurements where only ion beams of very low intensities are available.

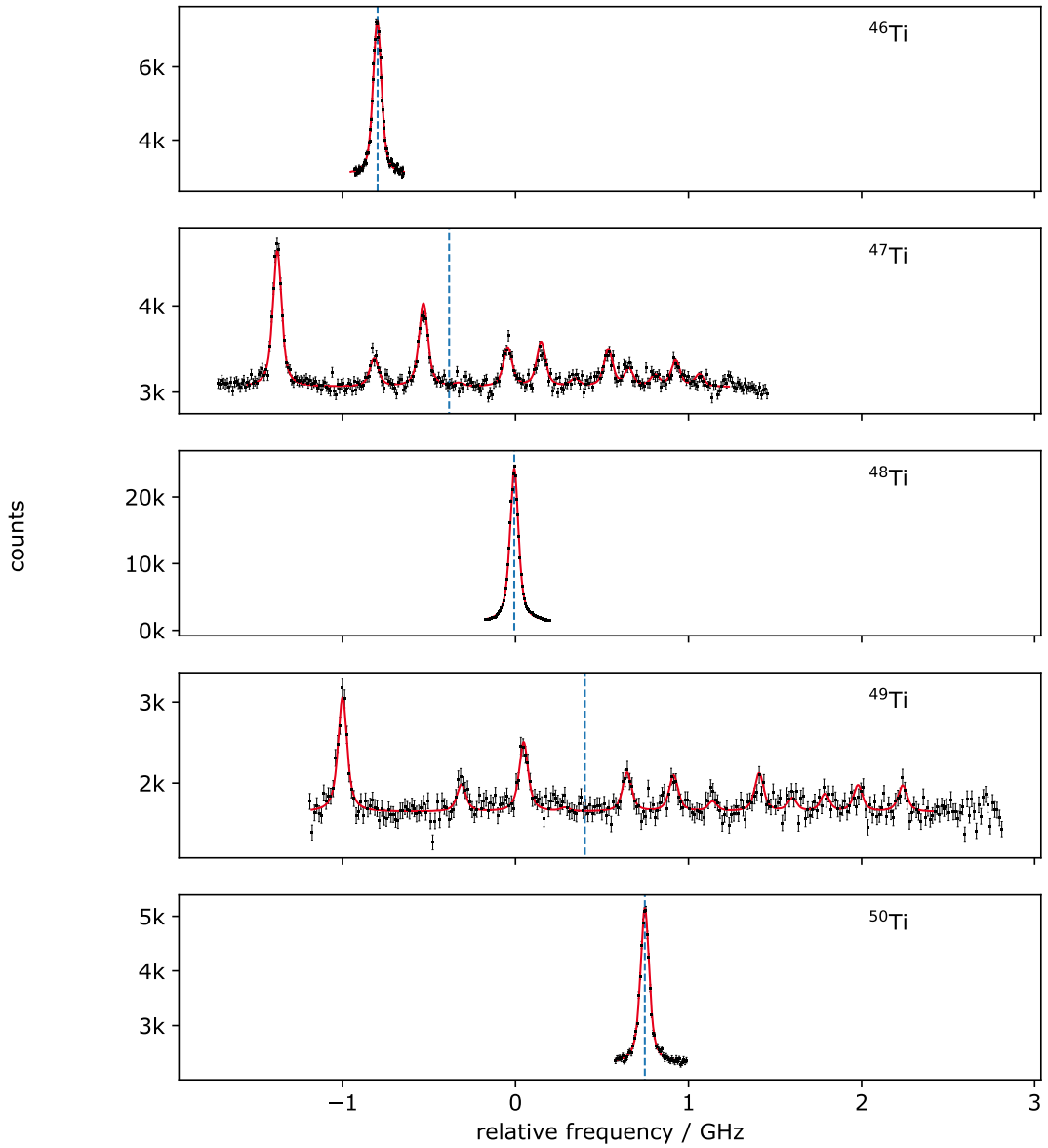

Figure 4.9: Spectra of the $J = 3/2 \rightarrow 5/2$ transition for all five stable isotopes of Ti^+. The data is presented with the statistical uncertainty as error bar in black and the symmetric Voigt profile fit to the data in red. The dashed blue line marks the center frequency or the center of gravity in case of the odd isotopes. In this transition, all hyperfine lines are resolved in the odd isotopes.

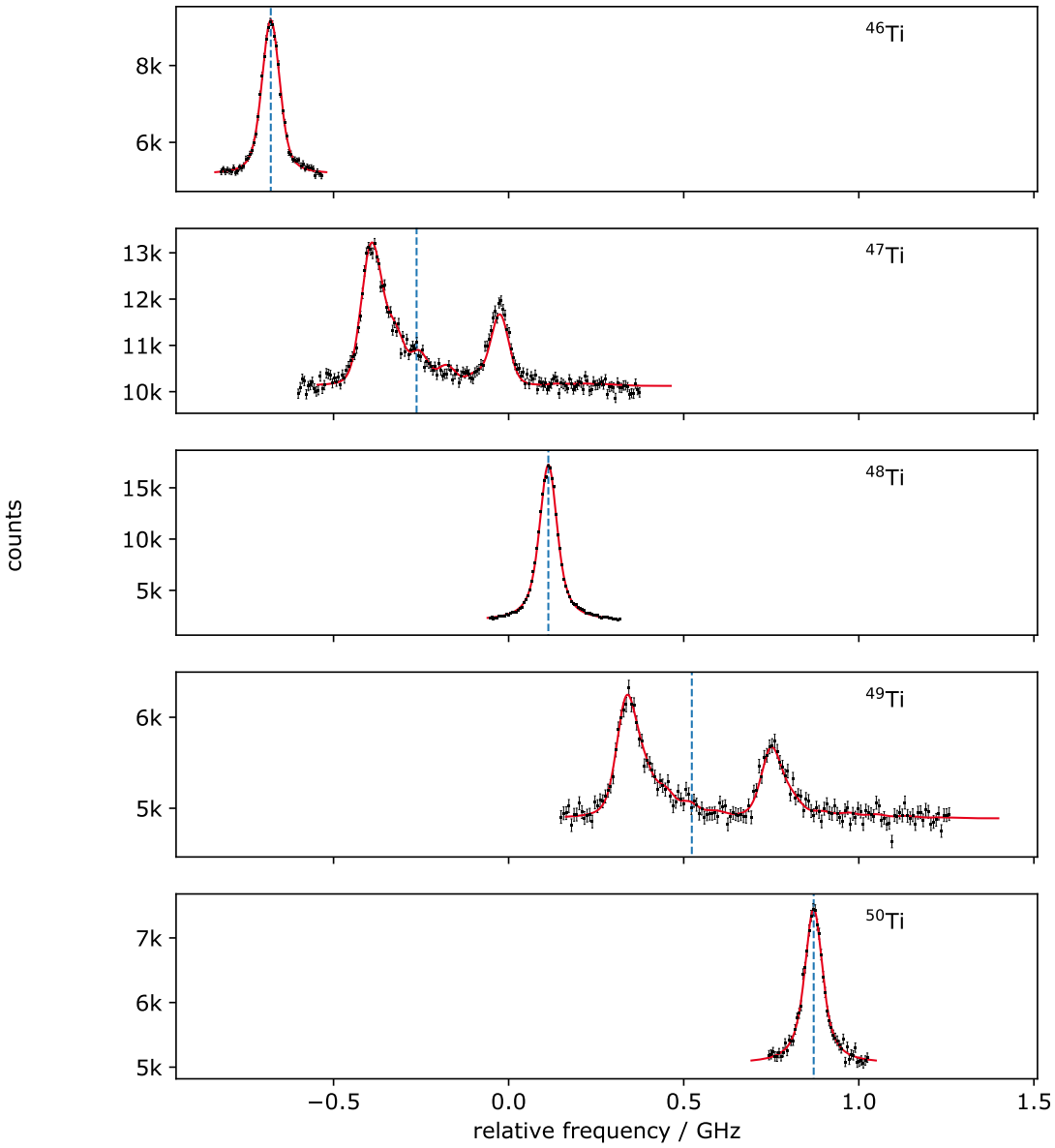

Figure 4.10: Spectra of the $J = {}^5/_2 \rightarrow {}^7/_2$ transition for all five stable isotopes of Ti^+. The data is presented with the statistical uncertainty as error bar in black and the symmetric Voigt profile fit to the data in red. The dashed blue line marks the center frequency or the center of gravity in case of the odd isotopes. In this transition the 15 hyperfine lines of the odd isotopes are squeezed together in two broad peak structures.

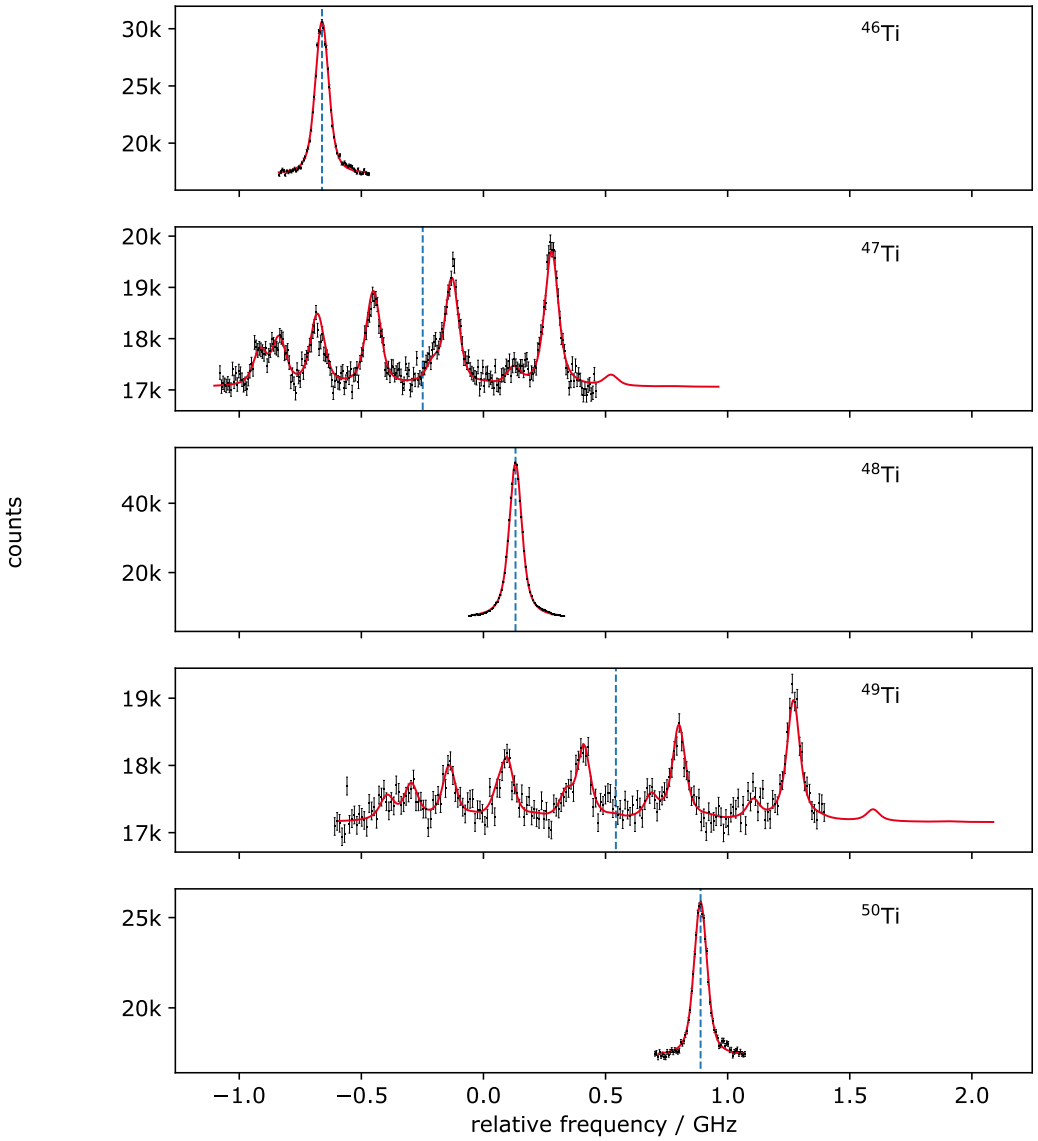

Figure 4.11: Spectra of the $J = {}^{7}/_{2} \rightarrow {}^{9}/_{2}$ transition for all five stable isotopes of Ti^{+}. The data is presented with the statistical uncertainty as error bar in black and the symmetric Voigt profile fit to the data in red. The dashed blue line marks the center frequency or the center of gravity in case of the odd isotopes. In this transition the 15 hyperfine lines of the odd isotopes are allocated within the visible spectrum, which has enough separated peaks to fit all free fit parameters well.

In Figs. 4.9, 4.10 and 4.11 the spectra of all isotopes are shown for the transitions T_{35},T_{57} and T_{79} respectively. The T_{35} transition in Fig. 4.9 shows all 12 hyperfine lines separated even though some of the peaks are not clearly distinguishable from the background. In the fit, the relative intensities were set to the theoretical values calculated from the 6-j symbols. For the peak positions five variables have been fitted freely which are the center frequency and the hyperfine parameters A_{l}, A_{u}, B_{l} and B_{u}. Since the nuclear spin is well known, five strong peaks are sufficient to determine all relevant information. For the linewidth the width of the Gaussian and the Lorentzian shape were fitted freely if not otherwise noted as well as the offset.

The individual peaks in the transitions T_{57} and T_{79} can not be resolved since the linewidth is larger than the splitting of the hyperfine lines. In the T_{57} transition shown in Fig. 4.10, all 15 hyperfine lines are compressed into two peaks. Nevertheless, the center frequency was determined with a statistical uncertainty of $\pm 2\,\mathrm{MHz}$. In the case of the T_{79} transition in Fig. 4.11, the spectrum shows five intense peaks which is sufficient to fit the five free parameters that determine the center position and the hyperfine parameters, allowing for a more precise determination.

4.2.2 Reference measurements and system stability

During the data analysis, all files that were recorded with parallel measured laser frequency and high voltage were stored in a database. If this parallel data was not recorded or the stabilization was not active the files were rejected for analysis. From this database, the data was fitted with the python-based fit program PolliFit [65]. The fit is performed in the frequency space and, hence, the Doppler tuning voltage is transformed to a frequency relative to the literature frequency.

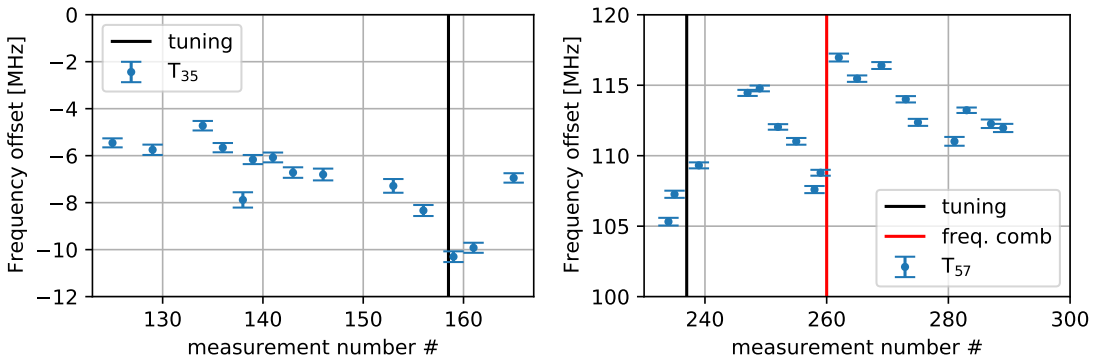

(a) (b)

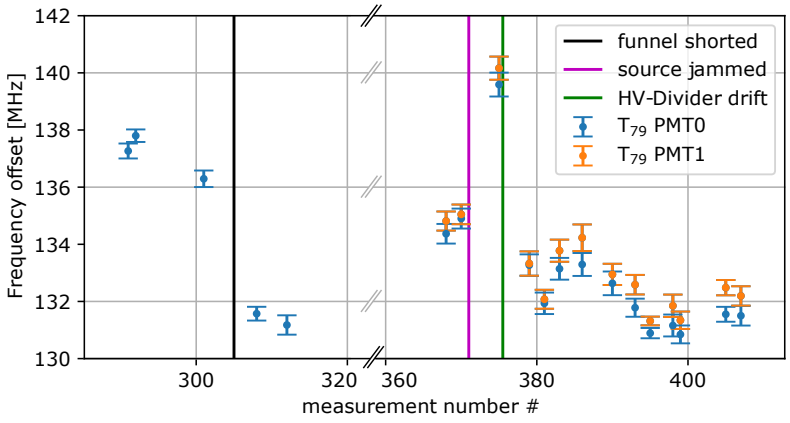

(c)

Figure 4.12: Measurements of the transition frequency of ^{48}Ti. In all three plots the deviation from the literature transition frequency is plotted against the measurement number. a) transition $J = {}^3/_2 \rightarrow {}^5/_2$ with the time of ion beam tuning marked with a black line. b) transition $J = {}^5/_2 \rightarrow {}^7/_2$ with line marking when the frequency measurement was switched from a wavemeter to a the frequency comb in red and the beam tuning in black. c) transition $J = {}^7/_2 \rightarrow {}^9/_2$. The first five measurements with only PMT0 like in the other measurements and after the installation with the additional results from PMT1. In black the it is marked when the funnel had a short circuit and in purple when the ion source target jammed which led to the HV-Divider drift marked in green.

In Fig. 4.12 the evolution of the center frequency of the reference isotope ^{48}Ti is shown for the three different transitions. These measurements were performed regularly during the measurement period. This way the measurements of the other isotopes can be compared to the closest reference measurement reducing effects of drifts and also revealing the stability of the system during the measurement period. These drifts, which appear in all three transitions, are of the order of $10\,\mathrm{MHz}$ and can be caused by a drift of the acceleration potential or changes in the angle between laser and ion beam introduced by changes of the ion-beam tuning. The vertical black lines in Fig. 4.12 a mark where the ion beam was tuned to achieve a better signal-to-noise ratio. The beam tuning before measurement #159 changes the center frequency by $-2.1\,\mathrm{MHz}$ which would correspond to a change of the angle between the beams by $2.5\,\mathrm{mrad}$ if the drift was purely caused by beam tuning.

In Fig. 4.12 b the T_{57} transition reference measurements are shown. For the measurements before the red vertical line the spectroscopy laser was stabilized to the wavelength meter until the frequency comb was employed. The absolute frequency measurement of the wavelength meter is less accurate than with the comb but could be confirmed to deviate less than $2\,\mathrm{MHz}$. The relative drift of the set laser frequency during the 3 hours measurement period is less than $0.75\,\mathrm{MHz}$ according to [115]. Hence, the drift of $10\,\mathrm{MHz}$ cannot be explained by drifts of the laser frequency. Beam tuning was only performed before measurement number #238 (black line) and thus, cannot explain the drift. The laser ablation process can cause short-term (millisecond) voltage deviations since a considerable amount of charge is removed from the target surface. This has to be compensated by a current from the Heinzinger[2] 14-kV power supply. Due to the helium gas in the target region, the charged particles stay separated from the conducting volume also for short timescales, before reaching conducting surfaces again. This again will compete with the Heinzinger for re-charging the high-voltage platform. As shown in Fig. 4.6, the center frequency does not change within the temporal structure of an ion bunch, which indicates that the voltage equilibrium is re-established at the time when the bunch is ejected from the second nozzle. The voltmeter[3] reads out the divider voltage and transmits it to the data acquisition. It is unable to detect such short-term fluctuations since it is averaging

[2] Heinzinger PNChp 20000-10 po
[3] KEYSIGHT 3458A 8½ Digit Multimeter

over 1-s timescales. It might, however, read a slightly modified voltage since the repetitive 100 Hz, <1 ms voltage fluctuations are contributing to the averaging interval. This would lead to an offset between the "real" voltage and read-out voltage, which could also vary in amplitude depending on the exact parameters of the ablation process. A maximum offset of $0.5\,\mathrm{V}$ seems plausible and can also explain the fluctuations in the center frequency of the reference isotopes. However, this process is not fully understood yet, and was not investigated further in the titanium measurements. Thus, this plausible explanation should be taken with the necessary caution until further experiments are conducted.

While measuring the transition T_{79} shown in Fig. 4.12 c, the funnel electrodes had a short circuit introduced by the titanium material deposition in the electrode gaps. After clearing the funnel short circuit and continuing the measurements the center frequency had shifted $-4.8\,\mathrm{MHz}$. The reason for this difference is again not explicable by the well-understood systematic uncertainties.

Between #320 and #360 another PMT was installed at the second chamber of the optical detection region. It should be noted that there is a small (0.5 MHz) but systematic offset between the results from the two detection chambers. This difference could be caused by a small contact potential arising from the different surface structure or surface oxidation. Another possibility is that the laser beam, which is smaller than the ion beam, is interacting with another part of the ion beam in the two detection chambers that may have a slightly different velocity distribution. However, the offset of $0.5\,\mathrm{MHz}$ is negligible compared with the other uncertainties and does especially cancel in the isotope shifts.

Long-term drifts of the beam energy due the acceleration potential are generally unlikely, since the applied HV at the ion source was stabilized to the value of a precision HV divider to $\pm 0.01\,\mathrm{V}$ allowing frequency drifts of only $<0.26\,\mathrm{MHz}$. After measurement #373 the ion-source target jammed and the whole system had to be shut down for a few hours of maintenance. The first reference after the restart has an offset of about $6\,\mathrm{MHz}$ to the other reference measurements. However, the voltage divider used for the stabilization is known to have a run-in time until it reaches its specifications. A short term 18-ppm deviation is possible and can explain the outlying data point #373. In all other measurements, the HV divider had a sufficiently long running-in time of more than 60 min.

Table 4.3: Isotope shift of all stable titanium isotopes in the three investigated $4s \rightarrow 4p$ transitions. The first parenthesis denotes the statistical uncertainty and the second gives the total uncertainty where the systematic uncertainty of $\pm 600\,\mathrm{kHz}$ has been added in quadrature. T_{35}: $J = {}^3/_2 \rightarrow {}^5/_2$; T_{57}: $J = {}^5/_2 \rightarrow {}^7/_2$; T_{79}: $J = {}^7/_2 \rightarrow {}^9/_2$

Transition	^{46}Ti	^{47}Ti	^{49}Ti	^{50}Ti
T_{35}	-788.1(0.4)(0.8)	-375.0(0.6)(0.9)	408.5(1.1)(1.3)	753.6(0.3)(0.7)
T_{57}	-790.2(0.8)(1.0)	-373.6(1.9)(2.0)	412.4(2.1)(2.2)	754.4(0.3)(0.7)
T_{79}	-792.6(0.3)(0.7)	-377.9(1.1)(1.3)	408.7(1.4)(1.6)	756.9(0.7)(1.0)

4.2.3 Isotope shifts

The measurement of a frequency difference is much more precise than the absolute frequency measurements since many uncertainties cancel in the relative measurement. During the measurement period, every transition was measured several times and compared to a reference measurement in ^{48}Ti to determine the isotope shift. Generally, the reference measurement closest in time was chosen, or if the measurement was performed between two reference measurements, it was compared to the mean of both reference measurements. The resulting isotope shift is calculated by the weighted average

$$\nu_{\text{w.av.}} = \frac{\sum w_i x_i}{\sum w_i} \tag{4.5}$$

according to the uncertainty from the fit results Δx_i with the weight

$$w_i = \frac{1}{\Delta x_i^2}. \tag{4.6}$$

The uncertainty of the weighted average is given by

$$\Delta\nu_{\text{w.av.}} = \frac{1}{\sqrt{\sum w_i}}. \tag{4.7}$$

If the standard deviation

$$\Delta\nu_{\text{st.dev.}} = \sqrt{\frac{\sum_{i=1}^{n}(\nu_i - \mu)^2}{n}} \tag{4.8}$$

Table 4.4: A and B values of the three investigated transitions. The uncertainty is the statistical uncertainty which is large for the B values of the last two transitions because the different lines are not well separated. The subscript u indicates the upper level and the subscript l the lower level.

Transition	Isotope	A_u	A_l	B_u	B_l
$J = {}^3/_2 \rightarrow {}^5/_2$	^{47}Ti	-120.3(0.5)	68.0(0.8)	78(4)	23(4)
	^{49}Ti	-120.3(0.4)	68.4(0.6)	50(6)	8(7)
$J = {}^5/_2 \rightarrow {}^7/_2$	^{47}Ti	-69.2(0.6)	-72.4(1.0)	71(26)	18(21)
	^{49}Ti	-69.3(1.8)	-73.1(3)	17(20)	-35(23)
$J = {}^7/_2 \rightarrow {}^9/_2$	^{47}Ti	-43.7(0.9)	-114.7(1.1)	133(40)	70(31)
	^{49}Ti	-45.1(1.6)	-116.8(2.0)	36(74)	-8(65)

with the arithmetic mean μ and the number of individual values for the shift of one isotope n yielded a larger value, it was taken as the uncertainty of the mean instead.

The extracted isotope shifts are listed in Tab. 4.3, with the statistical uncertainty in the first parentheses and the total uncertainty in the second. The total uncertainty is calculated by adding a systematic uncertainty of $600\,\mathrm{kHz}$, which will be discussed below, in quadrature.

For the determination of the isotope shift of the odd isotopes ^{47,49}Ti, the center of gravity of the hyperfine structure had to be determined (see Sec. 2.3). For this reason, the A and B hyperfine parameters of the transitions as well as the center-of-gravity of the hyperfine structure are free parameters of the fit. The resolved peaks in the T_{35} transition lead to a higher precision for the hyperfine parameters, than in the other two transitions. Due to the lower abundance and the splitting into multiple lines, the signal of the odd isotopes was very weak in some measurements. For this reason in the analysis of measurement #297 the fit parameters had to be constrained, i.e., the hyperfine parameters were fixed to the average of the other measurements of the T_{79} transition to extract at least the isotope shift from this spectrum.

In Tab. 4.4 the extracted hyperfine parameters A and B are shown. The values of the T_{35} transition could be determined with an uncertainty better than $1\,\mathrm{MHz}$ for A and better than $10\,\mathrm{MHz}$ for B. For the other two transitions the uncertainty of the A values is up to three times higher as less peaks could be resolved. Since the sensitivity on the B value is

Table 4.5: Ratios of the A and B values for all three transitions. Since the ratio between the values can be extracted from measurements of the magnetic moment and the quadrupole moment, they can be compared to literature values derived from the table of Stone [73]. The subscript u indicates the upper level and the subscript l the lower level.

Transition	A_u/A_u	A_l/A_l	B_u/B_u	B_l/B_l
Stone [73]	0.99973(1)	0.99973	1.21(4)	1.21(4)
$J = {}^3/_2 \rightarrow {}^5/_2$	1.000(5)	0.995(16)	1.55(0.23)	2.98(2.71)
$J = {}^5/_2 \rightarrow {}^7/_2$	0.998(54)	0.990(29)	4.3(5.2)	-0.52(0.42)
$J = {}^7/_2 \rightarrow {}^9/_2$	0.969(38)	0.982(19)	3.7(7.9)	-9.4(82.6)

lower, the corresponding uncertainty is even larger.

The ratio between the A values of two isotopes correlates to their magnetic moment μ_I and their nuclear spin I in the absence of a hyperfine anomaly

$$\frac{A}{A'} \propto \frac{\mu_I}{\mu_I'} \frac{I'}{I}.$$

For ^{47}Ti and ^{49}Ti, with the magnetic dipole moments from Stone [73], $\mu_I(^{47}\mathrm{Ti}) = -0.78848(1)$ and $\mu_I(^{49}\mathrm{Ti}) = -1.10417(1)$ and the nuclear spins $I(^{47}\mathrm{Ti}) = {}^5/_2$ and $I(^{49}\mathrm{Ti}) = {}^7/_2$ this ratio is 0.99973(1), which agrees within the uncertainty with the measured ratio of 1.000(5) for A_u and 0.995(16) for A_l in the T_{35} transition. This is also the case for the A value ratio of the other two transitions, showing that the values from this work agree with the literature, as shown in Tab. 4.5.

The B values between different isotopes are related to the electric quadrupole moment

$$\frac{B}{B'} \propto \frac{Q}{Q'}.$$

According to Stone, a ratio of 1.21(4) is expected. As discussed above, the extracted B values have a relatively large uncertainty, particularly for the T_{57} and the T_{79} transition. As shown in Tab. 4.5, our results agree with the reference values within that large uncertainty especially in the well-resolved T_{35} transition. However, the current resolution of this measurement is not sufficient to precisely determine electric quadrupole moments.

4.2.4 Systematic uncertainties

Besides the statistical uncertainty, several systematic contributions add to the total uncertainty. In all tables, the statistical uncertainty is given in the first parentheses and the total uncertainty in the second parentheses. The rest-frame transition frequency

$$\nu_0 = \nu_a \left[1 + \frac{eU_{\text{tot}}}{mc^2} \left(1 + \cos(\alpha) \sqrt{1 + 2\frac{mc^2}{eU_{\text{tot}}}} \right) \right]^{-1} \tag{4.9}$$

depends on several parameters, which all need to be treated carefully in order to estimate their systematic impact. The parameters are the anticollinear laser frequency ν_a, the electric charge e, the total acceleration voltage U_{tot}, the ion mass m, the speed of light c and the angle between laser and ion beam α.

In the determination of isotope shifts, most of the systematic uncertainty contributions cancel in the calculated frequency difference. In the following, the uncertainty of the total transition frequencies will be discussed first and then the remaining relative contributions will be extracted. The remaining uncertainty for the isotope shift is, if not noted otherwise, due to the different masses of the isotopes and the mass dependency of the Doppler shift, which leads to a slightly different impact of the uncertainties for the different isotopes. For this reason, the noted uncertainty of the isotope shift will always be the largest uncertainty from all measured isotopes.

The laser frequency ν_a was stabilized to a frequency comb, yielding an uncertainty of $300\,\text{kHz}$ which corresponds to an uncertainty of $10\,\text{kHz}$ for the isotope shift, since the laser frequency was not changed between the different isotope measurements and the respective reference measurements. The uncertainties of the speed of light c and the electric charge e is zero by definition. The atomic mass value is taken from [68] and subtracted by an electron mass [116] with a maximum uncertainty of $0.18\,\mu\text{u}$. This causes an uncertainty of 1.4 kHz and can be neglected.

The laser and ion beam are overlapped anticollinearly at an angle $\alpha = 0 \pm \Delta\alpha$. The maximum angular deviation possible for two infinitely small beams passing through the

two 10-mm irises, $2\,\mathrm{m}$ apart, of the COALA setup is $10\,\mathrm{mrad}$. Since the ion beam has about the size $10\,\mathrm{mm}$ and the laser beam was adjusted with a smaller iris diameter, an alignment worse than half of this angle can be excluded, as it would lead to significant signal loss through the irises, which were also closed to smaller diameters while beam-tuning. Hence, the angle uncertainty $\Delta\alpha$ is estimated to be $5\,\mathrm{mrad}$, which leads to a maximum deviation of the absolute transition frequency of $10\,\mathrm{MHz}$ for the probed transitions. As the angle was always kept constant during the isotope shift measurements compared to the reference measurement this shift was shifting all isotopes in the same way. The corresponding uncertainty for the isotope shift is below $12\,\mathrm{kHz}$.

The remaining parameter in Eq. (4.9) is the acceleration voltage U_{tot} which consists of the contributions

$$U_{\mathrm{tot}} = U_{\mathrm{acc}} + U_{\mathrm{offset}} + f_{\mathrm{Kepco}} \cdot U_{\mathrm{DAC}} + U_{\mathrm{KepcoOffset}}. \tag{4.10}$$

The acceleration voltage was measured with a high voltage divider with an accuracy of $3\,\mathrm{ppm}$ according to the calibration with the PTB[4] reference divider. At a 14-kV acceleration voltage this results in $42\,\mathrm{mV}$ which is also limiting the high voltage control loop precision, leading to an uncertainty in the absolute frequency of $1.1\,\mathrm{MHz}$ and for the isotope shift of $0.03\,\mathrm{MHz}$.

For the Doppler tuning, an additional voltage is applied to the detection region. A precise voltage between -8 and 8 V is generated by an 18-bit DAC and fed to a Kepco high voltage amplifier which amplifies this voltage by a factor f_{Kepco} with an offset of $U_{\mathrm{KepcoOffset}}$. This amplification factor was measured once during the measurement period of 8 days. In [55], this factor did change less than $100\,\mathrm{ppm}$ per year between 2018 and 2019 and is assumed to be constant over this measurement period. Fitting a straight line to the measured output voltage of the Kepco amplifier against the DAC set value, results in an inclination of $50.291\,64 \pm 0.000\,46$ with an offset of $(-0.011\,08 \pm 0.000\,33)\,\mathrm{V}$. The offset uncertainty corresponds to $10\,\mathrm{kHz}$ for the absolute transition frequency and less than one kHz for the isotope shift. The uncertainty of the inclination corresponds to $3.7 \times 10^{-3}\,\mathrm{V}$ and hence $95\,\mathrm{kHz}$ for the absolute transition frequency and $2\,\mathrm{kHz}$ for the isotope shift. The uncertainty of the 18-bit DAC can be neglected.

[4] Physikalisch-Technische Bundesanstalt (metrology institut Germany)

Additionally, contact potentials between the metals used in the connection chain between the HV supply and the funnel/buncher electrodes as well as the connection chain to the optical detection region can lead to an offset to the applied voltage. As the metals involved and their work function energies are Cu (4.53 - $5.1\,\mathrm{eV}$), Fe (4.67 - $4.81\,\mathrm{eV}$) and Al(4.06 - $4.26\,\mathrm{eV}$) [117], this can cause a maximum offset U_{cont} of $\pm 1.04\,\mathrm{V}$ corresponding to $26.8\,\mathrm{MHz}$ for the absolute transition frequency and $0.56\,\mathrm{MHz}$ for the isotope shift.

Another effect to be considered in this context is the drift of the center frequency along the temporal evolution of the bunch as discussed in Sec. 4.1.3. The drift for titanium was up to $5\,\mathrm{MHz}$. It could not be certified if this drift was coming from ions that are decelerated by collisions during extraction or by ions having a higher starting velocity from the gas jet extraction. This uncertainty will be accounted for as center drift with $\pm 5\,\mathrm{MHz}$ for the absolute transition frequency and $\pm 110\,\mathrm{kHz}$ for the isotope shift according to the corresponding difference of $0.2\,\mathrm{eV}$ in starting energy.

As mentioned in Sec. 4.2.2, there are changes of the center frequencies between the reference measurements that cannot be explained by the systematic uncertainties mentioned so far and are not covered by the statistical uncertainty from the fit results. Performing regularly reference measurements for the isotope shift measurements is extremely important to extract precise isotope shifts despite this effect. This shift can be related to voltage fluctuations during the ablation process that are integrated in the HV voltage measurement and lead to a systematic offset. For this reason $0.5\,\mathrm{V}$ are considered as systematic uncertainty for the offset of the high voltage measurement in the absolute transition frequency. This offset correlates with an uncertainty of $270\,\mathrm{kHz}$ for the isotope shift. The measurements of the non reference isotopes were performed sometimes before and sometimes after the reference measurement leading to deviations in both directions of the offset-drift. For this reason this uncertainty is represented in the standard deviation of the isotope shift measurements. All systematic uncertainties are summarized in Tab. 4.6.

Table 4.6: Summary of systematic uncertainties. Each line lists a cause for uncertainty, its absolute value and its impact on the absolute transition frequency evaulation and the isotope shift measurement. The latter is, generally, two to three magnitudes lower since most contributions cancel out when the isotope shift is calculated.

parameter	value uncertainty	uncertainty ν_0 [MHz]	uncertainty IS [kHz]
laser freq.	$\pm$0.3 MHz	$\pm$0.3	$\pm$10
angle	$\pm 5\,\mathrm{mrad}$	-10	$\pm$12
mass	$0.18\,\mu\mathrm{u}$	$\pm$0.0014	< 1
U_{acc}	$42\,\mathrm{mV}$	$\pm$1.1	$\pm$30
f_{Kepco}	$\pm 46 \times 10^{-5}$	$\pm$0.095	$\pm$2
$U_{\mathrm{KepcoOffset}}$	$\pm 0.33\,\mathrm{mV}$	$\pm$0.01	< 1
U_{cont}	max. $1.04\,\mathrm{V}$	$\pm$26.8	$\pm$560
center drift	$< 5\,\mathrm{MHz}$	$\pm$5	$\pm$110
asymmetry	$\pm 0.26\,\mathrm{MHz}$	$\pm$0.26	$\pm$6
sys. offset	$\pm 0.5\,\mathrm{V}$	$\pm$12.5	$\pm$270
diff. PMT	$\pm$0.5 MHz	$\pm$0.5	$\pm$10
combined	-	$\pm$32	$\pm$633

4.2.5 King-Plot

A consistency check of the measured isotope shift is performed using a King-Plot. Plotting the modified isotope shifts of two transitions against each other, the data points should form a straight line. This is shown in Fig. 4.13 a and b, where the modified isotope shifts of the T_{57} and the T_{79}, respectively, are plotted against the T_{35} isotope shifts. The T_{35} transition was chosen as reference since a lower uncertainty was achieved in that case. In both cases, an excellent linearity within the 1σ interval is achieved which demonstrates the reliability of the measurements.

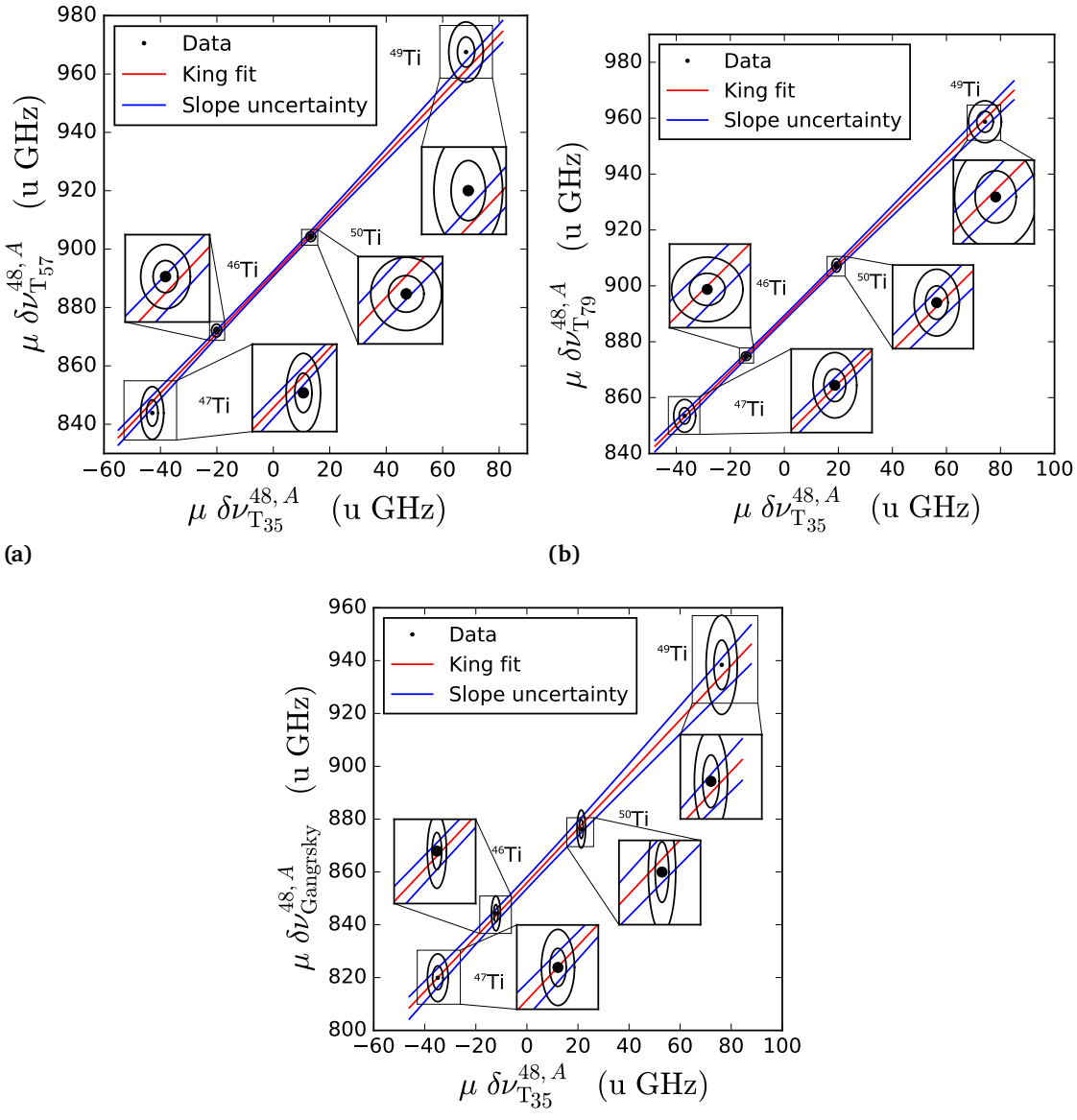

Figure 4.13: King-Plot comparison between the individual transitions. In a) -c) King fits are shown that plot the isotope shifts of a transition against the isotope shift of the $J = 3/2 \rightarrow 5/2$ transition and showing magnified details of the errors aside. The lines are in particular a) $J = 5/2 \rightarrow 7/2$, b) $J = 7/2 \rightarrow 9/2$ and c) the $3d^2(^3\mathrm{F})4s\,^4F_{/} \rightarrow 3d^2(^3\mathrm{F})4p\,^4F_{/}$ transition investigated by Gangrsky et al. [47].

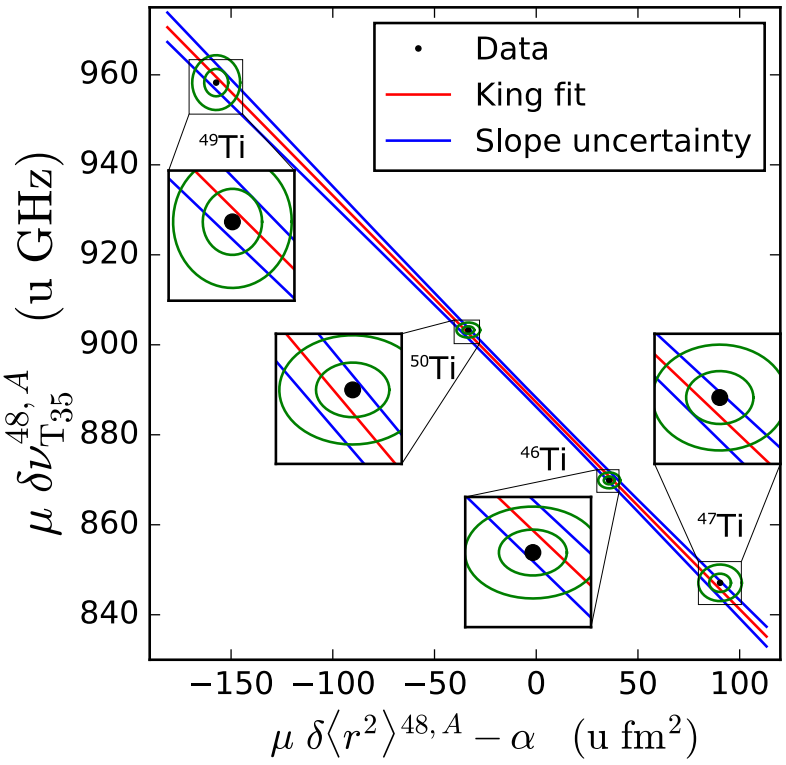

Figure 4.14: King-Plot to determine atomic factors for charge radii determination. The modified isotope shift is plotted against the modified charge radius and a straight line is fitted to the data. The inclination of the line is the field shift factor and from the y-axis intersection the mass shift factor can be extracted. The uncertainty is shown magnified in the insets.

This procedure can also be used to compare the presented results with measurements from other groups. In Fig. 4.13 c the measured isotope shifts from Gangrsky et al. 2004 [47] of the $3d^2(^3\mathrm{F})4s\ ^4F_{3/2} \rightarrow 3d^2(^3\mathrm{F})4p\ ^4F_{3/2}$ transition are plotted against the T_{35} transition. Again, both modified isotope shifts align within the 1-σ interval, which means that both results agree well. Furthermore, the field-shift ratio can be extracted from these King Plots to be $F_{T_{57}}/F_{T_{35}} = 1.02(5)$, $F_{T_{79}}/F_{T_{35}} = 0.96(4)$ and $F_{T_{33}}/F_{T_{35}} = 1.03(8)$. Within uncertainties they are all consistent with 1, as is expected for transitions from the same fine-structure multiplett. Deviations from this ratio are caused by relativistic effects and

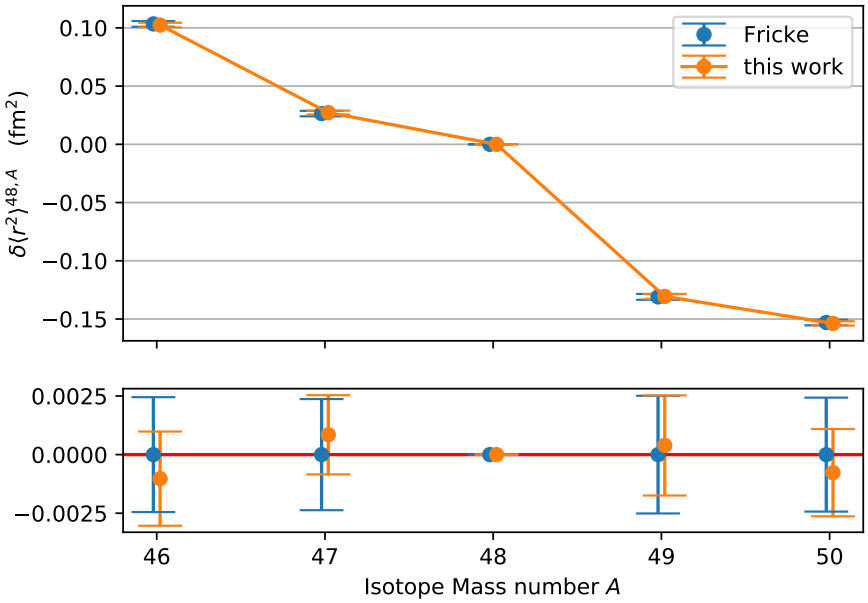

Figure 4.15: Difference of the mean squared charge radius of the stable isotopes compared to the value of ^{48}Ti. In the upper plot the literature values derived from [76] are shown in blue and compared with values extracted in this work, shown in orange. In the lower plot the deviations from the literature values are shown enlarged, showing a well agreement.

were reported previously and used as a benchmark for atomic theory [13], [54], [118]. However, a much more accurate measurement would be required to see such an effect.

Another King-Plot procedure can be used to determine the field-shift factor F and the mass shift factor K as described in Sec. 2.2.2. In Fig. 4.14 the modified isotope shift of the T_{35} transition is plotted against the modified charge radius difference. For this analysis, the charge radii from Fricke and Heilig [76] were used as input parameters, which are listed in Tab. 2.1, derived according to the method described in König et al. [119]. The data points agree with a straight line within their uncertainties. Since the charge radius values were derived from other methods than laser spectroscopy this shows that the results from this work agree also with independent measurements. The mass- and field shift parameters were extracted and are listed in Tab. 4.7. This will allow us one

Table 4.7: Extracted field shift and mass shift constants from the King Plot analysis of the three measured transitions.

transition	F [MHz/fm^2]	K [GHz/u]	K_α [GHz/u]	α [u fm^2]
$J = {}^3/_2 \rightarrow {}^5/_2$	-460(34)	818.3(5.4)	886.8(2.1)	-149
$J = {}^5/_2 \rightarrow {}^7/_2$	-490(40)	881.5(6.4)	889.0(2.3)	-150
$J = {}^7/_2 \rightarrow {}^9/_2$	-439(34)	825.9(5.4)	890.8(2.1)	-148

to determine the charge-radii of short-lived isotopes from isotope shift measurements as they are planned at FRIB.

For further analysis, the charge radii were projected onto the fitted straight line using this physical constraint of the King-Plot to improve the values of $\delta\langle r^2\rangle$. Results are depicted in Fig. 4.15. The reference values from Fricke and Heilig are plotted in blue, and the result from this work in yellow. The result from this work was derived from the combination of all three measured transitions T_{35}, T_{57} and T_{79} which were fitted together in one multi-dimensional King-Plot using the Monte-Carlo method to find the best fit, as described in [120].

A King-Plot was also used in the analysis of Gangrsky et al. from 1995 [46] to determine the differential nuclear charge radius $\delta\langle r^2\rangle$ of ^{47}Ti and ^{49}Ti. To that point, model-independent values for the mean square charge radius $\langle r^2\rangle$ of ^{46,48,50}Ti were known from Wohlfahrt et al. [121] and were used as input parameters. In a second measurement in Gangrsky et al. from 2004 [47] the short-lived isotopes, ^{44}Ti and ^{45}Ti, were measured together with all stable isotopes. The analysis was performed with the same input parameters from Wohlfahrt. Using the values from Fricke and Heilig [76] as input for the isotope shifts of Gangrsky from 2004, shifts the values for $\delta\langle r^2\rangle$ slightly, which then agree well with the results presented in this work.

4.2.6 Transition frequencies

Since the beam energy can be determined from the HV divider and the laser frequency is well known from the lock to the frequency comb, it is possible to extract values for the

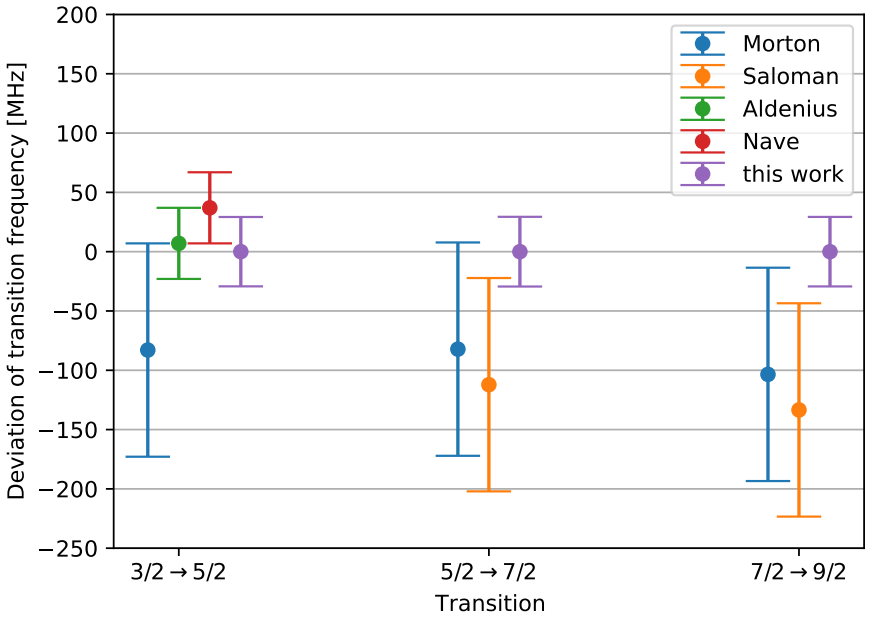

Figure 4.16: Comparison of transition frequencies. For the $J = {}^3/_2 \rightarrow {}^5/_2$ transition more recent values from Aldenius [122] and Nave [123] exist, which are in good agreement with the value presented in this work. For the other two transitions only the values presented in Morton and Saloman [124] exist, which agree with the values from this work but the uncertainties are improved by a factor of two.

transition frequencies according to (4.9). As discussed in Sec. 4.2.4, the beam-energy uncertainty and the alignment cause the dominant systematic uncertainties. The results are listed in Tab. 4.8. In the literature, three groups performed measurements with notable precision on these Ti^+ transitions before. Huldt et. al [125] and Zapadlik et al. [127] investigated all lines in Ti from hollow cathode discharges with a spectrometer. However, the uncertainty from Huldt et al. is rather large ($5\,\mathrm{GHz}$) and the results from Zapadlik et al. were not directly published. Instead, these measurements were privately communicated and published in the tables of Morton [126] and Saloman [124]. The values from both reference tables are given in Tab. 4.6 since they yield slightly different results. Also, the stated uncertainties differ. Hence, a 90-MHz uncertainty is listed in Tab. 4.6, which is the lower uncertainty limit of the original report from Zapadlik et al. [127], in which

Table 4.8: Transition frequencies compared with literature values. The transitions were first measured by Huldt [125] with a rather large uncertainty. With improved accuracy those values were measured by Zapadlick but published only as a private communication in Morton [126] and Saloman [124]. Aldenius [122] remeasured the $J = {}^3/_2 \rightarrow {}^5/_2$ transition which was reevaluated by Nave [123]. For values presented from this work, the value in the first parentheses represents the statistical uncertainty and the value in the second parentheses the total uncertainty, with the systematic uncertainty of $\pm 30.8\,\mathrm{MHz}$ added in quadrature.

	$J = {}^3/_2 \rightarrow {}^5/_2$	$J = {}^5/_2 \rightarrow {}^7/_2$	$J = {}^7/_2 \rightarrow {}^9/_2$
Huldt [125]	885 717 630(5000)	888 598 636(5000)	891 657 418(5000)
Morton [126]	885 720 359(90)	888 600 075(90)	891 661 526(90)
Saloman [124]	-	888 600 045(90)	891 661 496(90)
Aldenius [122]	885 720 448(30)	-	-
Nave [123]	885 720 478(30)	-	-
this work	885 720 441(1.6)(32)	888 600 157(3.3)(32)	891 661 629(2.5)(32)

they inform that they measured lines in Ti with uncertainties of 90-$150\,\mathrm{MHz}$. The third group, Aldenius et al., performed measurements with a high-resolution Fourier transform spectrometer and a hollow-cathode light source on selected lines of astronomical interest, including the $J = {}^3/_2 \rightarrow {}^5/_2$ transition in Ti^+ [122], [128]. They achieved an uncertainty of $30\,\mathrm{MHz}$. A small correction to this value was done by Nave since he improved the reference values for the spectrometer calibration [123].

In Fig. 4.16 all results are plotted with exception of the measurement from Huldt et al. due to their large uncertainty. The result from Zapadlik is systematically shifted to smaller frequencies, which indicates a deviation in the calibration of their spectrometer, which is, however, covered by the reported uncertainty. The new collinear laser spectroscopy measurements are in good agreement with the literature. Particularly, the most precise measurement from Aldenius is confirmed by the new measurements.

5 Future technical improvements

Even though the ion source was carefully simulated and designed, a few options for future improvements were identified during tests and operation. Particularly, the deposition of material at the funnel electrodes came up as an unexpected challenge for continuous operation of the source. Moreover, the funnel chamber was not designed to be frequently disassembled for cleaning, which should be considered as a design improvement for a next version. A solution might be the use of femtosecond lasers, which are becoming more and more affordable as tabletop devices and could be an option to mitigate this deposition since the heat conduction is to slow to melt the target surface and, hence, prevents effects like phase explosion.

Another detail that should be considered is that a short focal length of the lens in front of the ablation target can strongly reduce the material ejection from the target without deterioration of the ion production. This is possible due to the smaller focus with the short focal length. To enable a movement of the focus along the target radius and the observation of the target with a camera, the last mirror should be placed closely to the lens. In the present design this is not possible due to the long small bore hole between the window flange and the lens which is positioned inside the vacuum chamber. For this reason it would be advantageous to have the window flange close at the target and also to forsee a possibility to adjust the lens from the outside.

Concerning the buncher, one major challenge could be already solved within this work: the line broadening caused by RF-heating in the buncher was reduced from up to 300 MHz down to a level where a correlation between RF voltage and linewidth is no longer

observed. This leads to an energy spread of the ion source that is comparable to the one of RFQ cooler and bunchers used at online facilities. Nevertheless, additional studies need to be undertaken in the bunching section. Even though the transport of ions through the buncher exit can be completely blocked by a reasonable DC voltage, no evidence of ion accumulation could be demonstrated. This should be investigated further with more sensitive detection devices like a magnetof. A successful bunching of the ions in this section will allow to release a much shorter bunch and will significantly improve the signal-to-noise ratio.

An additional feature to investigate the ion beam composition in terms of elements, charge-states and molecule formation, would be the installation of a fast HV-switch for precise time-of-flight measurements. It would allow also to cut time slices out of the ion bunch and enable to investigate this composition for each time segment.

6 Summary and Outlook

In this work a versatile laser ablation ion source with buffer gas extraction was built. Ion production was successfully demonstrated for iron, copper, calcium and titanium whereof calcium and titanium were investigated by laser spectroscopy. Furthermore, the rest-frame frequencies and the isotope shifts of all five stable titanium isotopes were measured for the transitions $3d^2(^3\mathrm{F})4s\ {}^4F_{3/2} \rightarrow 3d^2(^3\mathrm{F})4p\ {}^4G_{5/2}$, $3d^2(^3\mathrm{F})4s\ {}^4F_{5/2} \rightarrow 3d^2(^3\mathrm{F})4p\ {}^4G_{7/2}$ and $3d^2(^3\mathrm{F})4s\ {}^4F_{7/2} \rightarrow 3d^2(^3\mathrm{F})4p\ {}^4G_{9/2}$ at the COALA beamline at TU Darmstadt on an ion beam provided by this ion source.

Essentially, ion beams from all elements can be produced either from a pure target material or an alloy. The ion source design enables the fast exchange ($<$ 3 h) of the different targets, by opening a single flange. Also, the RF system can be flexibly adapted to new ion species since the frequency can be adjusted between 1 and $10\,\mathrm{MHz}$ with amplitudes between 0 and $70\,\mathrm{V_{pp}}$. This shows the high versatility of the ion source and enables several future applications. Additionally, the laser background in spectroscopy experiments can be strongly reduced by the use of this ion source since a bunched beam with a pulse length of 1 ms is generated. The superiority of the buffer-gas cooled laser ablation source compared to a direct laser ablation source was demonstrated in spectroscopy measurements on Ca^+. The energy width and, hence, the linewidth could be significantly improved to approximately $60\,\mathrm{MHz}$. This is comparable to the linewidth, e.g., observed from ion beams cooled in a radio-frequency quadrupole trap. Also the line-shape was improved from being strongly asymmetric in case of direct ablation [24] to a nearly Voigtian profile.

With this source the above mentioned titanium transitions were measured. The determined rest-frame frequencies of the $J = {}^5/_2 \rightarrow J = {}^7/_2$ and the $J = {}^7/_2 \rightarrow J = {}^9/_2$ transitions could be significantly improved compared to literature values [124], [126] and the $J = {}^3/_2 \rightarrow J = {}^5/_2$ transition is of the same precision and in excellent agreement with a recent spectrometer measurement [122], [123]. The present uncertainty is dominated by the beam energy and will be further improved by simultaneous collinear and anticollinear measurements, which are independent of the beam energy.

Also, the isotope shifts in these transitions were determined with MHz accuracy, which is of importance as reference for astrophysical observations of quasar spectra. The uncertainty estimation was validated by comparing the results of all measured transitions, of literature isotope shifts from another transition [47], and the respective nuclear charge radii from muonic and electron-scattering measurements [76] through a King-plot analysis. The mass- and field-shift parameters were extracted, which are crucial for the extraction of nuclear charge radii from short-lived isotopes. Furthermore, the analysis of the three transitions yielded that the $J = {}^3/_2 \rightarrow J = {}^5/_2$ transition is best suited for online measurements since all hyperfine peaks of the odd-N isotopes are clearly resolved. In case of the $J = {}^5/_2 \rightarrow J = {}^7/_2$ transition, all peaks are merged into two lines, which strongly affects the achievable fit uncertainty for low statistic measurements and makes the extraction of hyperfine parameters unreliable. In the $J = {}^7/_2 \rightarrow J = {}^9/_2$ transition at least five strong peaks out of 15 could be resolved which would also be sufficient to constrain all free fit parameters. The measurements in titanium can be seen as the starting point to explore many more transitions of other elements that are of high interest for quasar observations [11] or for nuclear structure investigations. Particularly in the regime of the transition metals, only a few elements have been investigated with laser spectroscopy, which now became available with the laser ablation ion source. Isotope-shift measurements on stable beams will provide reference values for calibration purposes and the mass- and field shift parameters and, hence, will pave the way for nuclear structure investigations.

Bibliography

[1] "On the Revision of the International System of Units (SI). Resolution 1 (CGPM 26th Meeting, Versailles, November 13–16, 2018)", *Measurement Techniques*, vol. 62, pp. 472–473, 2019. DOI: 10.1007/s11018-019-01648-4.

[2] O. Poulsen, "Velocity and high-voltage measurements using resonant collinear, fast-beam/laser interactions", *Nuclear Instruments and Methods in Physics Research*, vol. 202, pp. 503–509, 1982. DOI: 10.1016/0167-5087(82)90548-8.

[3] J. Kohlmann and R. Behr, "Development of Josephson voltage standards", in *Superconductivity - Theory and Applications*, A. Luiz, Ed., InTech, 2011, ISBN: 978-953-307-151-0. DOI: 10.5772/17031.

[4] J. Krämer, K. König, C. Geppert, P. Imgram, B. Maaß, J. Meisner, E. W. Otten, S. Passon, T. Ratajczyk, J. Ullmann, and W. Nörtershäuser, "High-voltage measurements on the 5 ppm relative uncertainty level with collinear laser spectroscopy", *Metrologia*, vol. 55, pp. 268–274, 2018. DOI: 10.1088/1681-7575/aaabe0.

[5] J.-P. Uzan, "The fundamental constants and their variation: Observational and theoretical status", *Reviews of Modern Physics*, vol. 75, pp. 403–455, 2003. DOI: 10.1103/RevModPhys.75.403.

[6] M. P. Savedoff, "Physical Constants in Extra-Galactic Nebulæ", *Nature*, vol. 178, pp. 688–689, 1956. DOI: 10.1038/178688b0.

[7] D. J. Mortlock, S. J. Warren, B. P. Venemans, M. Patel, P. C. Hewett, R. G. McMahon, C. Simpson, T. Theuns, E. A. Gonzáles-Solares, A. Adamson, S. Dye, N. C. Hambly, P. Hirst, M. J. Irwin, E. Kuiper, A. Lawrence, and H. J. A. Röttgering, "A luminous quasar at a redshift of $z = 7.085$", *Nature*, vol. 474, pp. 616–619, 2011. DOI: 10.1038/nature10159.

[8] M. T. Murphy, J. K. Webb, V. V. Flambaum, V. A. Dzuba, C. W. Churchill, J. X. Prochaska, J. D. Barrow, and A. M. Wolfe, "Possible evidence for a variable fine-structure constant from QSO absorption lines: motivations, analysis and results", *Monthly Notices of the Royal Astronomical Society*, vol. 327, pp. 1208–1222, 2001. DOI: 10.1046/j.1365-8711.2001.04840.x.

[9] J. K. Webb, V. V. Flambaum, C. W. Churchill, M. J. Drinkwater, and J. D. Barrow, "Search for Time Variation of the Fine Structure Constant", *Physical Review Letters*, vol. 82, pp. 884–887, 1999. DOI: 10.1103/PhysRevLett.82.884.

[10] V. A. Dzuba, V. V. Flambaum, and J. K. Webb, "Calculations of the relativistic effects in many-electron atoms and space-time variation of fundamental constants", *Physical Review A*, vol. 59, pp. 230–237, 1999. DOI: 10.1103/PhysRevA.59.230.

[11] J. C. Berengut, V. A. Dzuba, V. V. Flambaum, J. A. King, M. G. Kozlov, M. T. Murphy, and J. K. Webb, "Atomic Transition Frequencies, Isotope Shifts, and Sensitivity to Variation of the Fine Structure Constant for Studies of Quasar Absorption Spectra", in *From varying couplings to fundamental physics*, ser. Astrophysics and Space Science Proceedings, C. Martins and P. Molaro, Eds., Berlin: Springer, 2011, pp. 9–16, ISBN: 978-3-642-19396-5. DOI: 10.1007/978-3-642-19397-2{\textunderscore}2.

[12] P. Campbell, I. D. Moore, and M. R. Pearson, "Laser spectroscopy for nuclear structure physics", *Progress in Particle and Nuclear Physics*, vol. 86, pp. 127–180, 2016. DOI: 10.1016/j.ppnp.2015.09.003.

[13] P. Imgram, K. König, J. Krämer, T. Ratajczyk, R. A. Müller, A. Surzhykov, and W. Nörtershäuser, "Collinear laser spectroscopy at ion-trap accuracy: Transition

frequencies and isotope shifts in the $6s\,^2\mathrm{S}_{1/2} \rightarrow 6p\,^2\mathrm{P}_{1/2,3/2}$ transitions in Ba^+", *Physical Review A*, vol. 99, 2019. DOI: 10.1103/PhysRevA.99.012511.

[14] S. L. Kaufman, "High-resolution laser spectroscopy in fast beams", *Optics Communications*, vol. 17, pp. 309–312, 1976. DOI: 10.1016/0030-4018(76)90267-4.

[15] K. Minamisono, P. F. Mantica, A. Klose, S. Vinnikova, A. Schneider, B. Johnson, and B. R. Barquest, "Commissioning of the collinear laser spectroscopy system in the BECOLA facility at NSCL", *Nuclear Instruments and Methods in Physics Research Section A*, vol. 709, pp. 85–94, 2013. DOI: 10.1016/j.nima.2013.01.038.

[16] P. Ahlberg, *Nobel Lectures in Chemistry 2001 – 2005*. World Scientific, 2008, ISBN: 978-981-279-444-4. DOI: 10.1142/6782.

[17] B. Wolf, *Handbook of Ion Sources*, First edition. Boca Raton, FL: CRC Press, 2017, ISBN: 9781315214054.

[18] J. S. Becker, "State-of-the-art and progress in precise and accurate isotope ratio measurements by ICP-MS and LA-ICP-MS : Plenary Lecture", *J. Anal. At. Spectrom.*, vol. 17, pp. 1172–1185, 2002. DOI: 10.1039/B203028B.

[19] K. Zimmermann, M. V. Okhapkin, O. A. Herrera-Sancho, and E. Peik, "Laser ablation loading of a radiofrequency ion trap", *Applied Physics B*, vol. 107, pp. 883–889, 2012. DOI: 10.1007/s00340-012-4884-1.

[20] S. Sturm, I. Arapoglou, A. Egl, M. Höcker, S. Kraemer, T. Sailer, B. Tu, A. Weigel, R. Wolf, J. C. López-Urrutia, and K. Blaum, "The ALPHATRAP experiment", *The European Physical Journal Special Topics*, vol. 227, pp. 1425–1491, 2019. DOI: 10.1140/epjst/e2018-800225-2.

[21] V.-V. Elomaa, T. Eronen, U. Hager, A. Jokinen, T. Kessler, I. D. Moore, S. Rahaman, C. Weber, and J. Äystö, "Development of a carbon-cluster ion source for JYFLTRAP", *Nuclear Instruments and Methods in Physics Research Section B*, vol. 266, pp. 4425–4428, 2008. DOI: 10.1016/j.nimb.2008.05.029.

[22] C. Izzo, G. Bollen, S. Bustabad, M. Eibach, K. Gulyuz, D. J. Morrissey, M. Redshaw, R. Ringle, R. Sandler, S. Schwarz, and A. A. Valverde, "A laser ablation source for offline ion production at LEBIT", *Nuclear Instruments and Methods in Physics Research Section B*, vol. 376, pp. 60–63, 2016. DOI: 10.1016/j.nimb.2015.12.019.

[23] B. Anđelić, M. Block, P. Chhetri, J. Even, F. Giacoppo, N. Kalantar-Nayestanaki, O. Kaleja, T. Murböck, F. Schneider, and S. Raeder, "Simulation studies of the laser ablation ion source at the SHIPTRAP setup", *Hyperfine Interactions*, vol. 241, 2020. DOI: 10.1007/s10751-020-01708-0.

[24] L. Renth, P. Imgram, J. Krämer, K. König, T. Lellinger, B. Maaß, P. Müller, T. Ratajczyk, and W. Nörtershäuser, "First experiments with a laser ablation source at the COALA setup", *Hyperfine Interactions*, vol. 241, 2020. DOI: 10.1007/s10751-020-01715-1.

[25] R. F. Garcia Ruiz, A. R. Vernon, C. L. Binnersley, B. K. Sahoo, M. Bissell, J. Billowes, T. E. Cocolios, W. Gins, R. P. de Groote, K. T. Flanagan, A. Koszorus, K. M. Lynch, G. Neyens, C. M. Ricketts, K. D. A. Wendt, S. G. Wilkins, and X. F. Yang, "High-Precision Multiphoton Ionization of Accelerated Laser-Ablated Species", *Physical Review X*, vol. 8, 2018. DOI: 10.1103/PhysRevX.8.041005.

[26] E. Mané, J. Billowes, K. Blaum, P. Campbell, B. Cheal, P. Delahaye, K. T. Flanagan, D. H. Forest, H. Franberg, C. Geppert, T. Giles, A. Jokinen, M. Kowalska, R. Neugart, G. Neyens, W. Nörtershäuser, I. Podadera, G. Tungate, P. Vingerhoets, and D. T. Yordanov, "An ion cooler-buncher for high-sensitivity collinear laser spectroscopy at ISOLDE", *The European Physical Journal A*, vol. 42, pp. 503–507, 2009. DOI: 10.1140/epja/i2009-10828-0.

[27] T. Sun, S. Schwarz, G. Bollen, D. Lawton, R. Ringle, and P. Schury, "Commissioning of the ion beam buncher and cooler for lebit", *The European Physical Journal A*, vol. 25, pp. 61–62, 2005. DOI: 10.1140/epjad/i2005-06-126-9.

[28] M. Tajima, A. Takamine, M. Wada, and H. Ueno, "Offline ion source for laser spectroscopy of RI at the SLOWRI", *Nuclear Instruments and Methods in Physics*

Research Section B, vol. 486, pp. 48–54, 2021. DOI: 10.1016/j.nimb.2020.10.013.

[29] T. Brunner, D. Fudenberg, A. Sabourov, V. L. Varentsov, G. Gratta, and D. Sinclair, "A setup for Ba-ion extraction from high pressure Xe gas for double-beta decay studies with EXO", *Nuclear Instruments and Methods in Physics Research Section B*, vol. 317, pp. 473–475, 2013. DOI: 10.1016/j.nimb.2013.05.086.

[30] T. Brunner, D. Fudenberg, V. Varentsov, A. Sabourov, G. Gratta, J. Dilling, R. DeVoe, D. Sinclair, W. Fairbank, J. B. Albert, D. J. Auty, P. S. Barbeau, D. Beck, C. Benitez-Medina, M. Breidenbach, G. F. Cao, C. Chambers, B. Cleveland, M. Coon, A. Craycraft, T. Daniels, S. J. Daugherty, T. Didberidze, M. J. Dolinski, M. Dunford, L. Fabris, J. Farine, W. Feldmeier, P. Fierlinger, R. Gornea, K. Graham, M. Heffner, M. Hughes, M. Jewell, X. S. Jiang, T. N. Johnson, S. Johnston, A. Karelin, L. J. Kaufman, R. Killick, T. Koffas, S. Kravitz, R. Krücken, A. Kuchenkov, K. S. Kumar, D. S. Leonard, F. Leonard, C. Licciardi, Y. H. Lin, J. Ling, R. MacLellan, M. G. Marino, B. Mong, D. Moore, A. Odian, I. Ostrovskiy, C. Ouellet, A. Piepke, A. Pocar, F. Retiere, P. C. Rowson, M. P. Rozo, A. Schubert, E. Smith, V. Stekhanov, M. Tarka, T. Tolba, D. Tosi, K. Twelker, J.-L. Vuilleumier, J. Walton, T. Walton, M. Weber, L. J. Wen, U. Wichoski, L. Yang, and Y.-R. Yen, "An RF-only ion-funnel for extraction from high-pressure gases", *International Journal of Mass Spectrometry*, vol. 379, pp. 110–120, 2015. DOI: 10.1016/j.ijms.2015.01.003.

[31] V. Varentsov and M. Wada, "Computer experiments on ion beam cooling and guiding in fair-wind gas cell and extraction RF-funnel system", *Nuclear Instruments and Methods in Physics Research Section A*, vol. 532, pp. 210–215, 2004. DOI: 10.1016/j.nima.2004.06.078.

[32] G. Savard, A. F. Levand, and B. J. Zabransky, "The CARIBU gas catcher", *Nuclear Instruments and Methods in Physics Research Section B*, vol. 376, pp. 246–250, 2016. DOI: 10.1016/j.nimb.2016.02.050.

[33] L. Querci, V. Varentsov, D. Günther, and B. Hattendorf, "An Rf-only ion funnel interface for ion cooling in laser ablation time of flight mass spectrometry", *Spec-*

trochimica Acta Part B: Atomic Spectroscopy, vol. 146, pp. 57–68, 2018. DOI: 10.1016/j.sab.2018.05.004.

[34] V. Varentsov, "Proposal for a new Laser ablation ion source for LaSpec and MATS testing", *ResearchGate*, 2016. DOI: 10.13140/RG.2.2.10904.39686.

[35] K. Kreim, M. L. Bissell, J. Papuga, K. Blaum, M. de Rydt, R. F. Garcia Ruiz, S. Goriely, H. Heylen, M. Kowalska, R. Neugart, G. Neyens, W. Nörtershäuser, M. M. Rajabali, R. Sánchez Alarcón, H. H. Stroke, and D. T. Yordanov, "Nuclear charge radii of potassium isotopes beyond $N = 28$", *Physics Letters B*, vol. 731, pp. 97–102, 2014. DOI: 10.1016/j.physletb.2014.02.012.

[36] R. F. Garcia Ruiz, M. L. Bissell, K. Blaum, A. Ekström, N. Frömmgen, G. Hagen, M. Hammen, K. Hebeler, J. D. Holt, G. R. Jansen, M. Kowalska, K. Kreim, W. Nazarewicz, R. Neugart, G. Neyens, W. Nörtershäuser, T. Papenbrock, J. Papuga, A. Schwenk, J. Simonis, K. A. Wendt, and D. T. Yordanov, "Unexpectedly large charge radii of neutron-rich calcium isotopes", *Nature Physics*, vol. 12, pp. 594–598, 2016. DOI: 10.1038/NPHYS3645.

[37] F. C. Charlwood, J. Billowes, P. Campbell, B. Cheal, T. Eronen, D. H. Forest, S. Fritzsche, M. Honma, A. Jokinen, I. D. Moore, H. Penttilä, R. Powis, A. Saastamoinen, G. Tungate, and J. Äystö, "Ground state properties of manganese isotopes across the $N = 28$ shell closure", *Physics Letters B*, vol. 690, pp. 346–351, 2010. DOI: 10.1016/j.physletb.2010.05.060.

[38] K. Minamisono, D. M. Rossi, R. Beerwerth, S. Fritzsche, D. Garand, A. Klose, Y. Liu, B. Maaß, P. F. Mantica, A. J. Miller, P. Müller, W. Nazarewicz, W. Nörtershäuser, E. Olsen, M. R. Pearson, P.-G. Reinhard, E. E. Saperstein, C. Sumithrarachchi, and S. V. Tolokonnikov, "Charge Radii of Neutron Deficient ^{52,53}Fe Produced by Projectile Fragmentation", *Physical Review Letters*, vol. 117, p. 252 501, 2016. DOI: 10.1103/PhysRevLett.117.252501.

[39] A. Klein, B. A. Brown, U. Georg, M. Keim, P. Lievens, R. Neugart, M. Neuroth, R. E. Silverans, L. Vermeeren, and I. Collaboration, "Moments and mean square charge radii of short-lived argon isotopes", *Nuclear Physics A*, vol. 607, pp. 1–22, 1996. DOI: 10.1016/0375-9474(96)00192-3.

[40] J. A. Behr, A. Gorelov, T. Swanson, O. Häusser, K. P. Jackson, M. Trinczek, U. Giesen, J. M. D'Auria, R. Hardy, T. Wilson, P. Choboter, F. Leblond, L. Buchmann, M. Dombsky, C. D. P. Levy, G. Roy, B. A. Brown, and J. Dilling, "Magneto-optic Trapping of β-Decaying $^{38}\mathrm{K}^{m}$, $^{37}\mathrm{K}$ from an on-line Isotope Separator", *Physical Review Letters*, vol. 79, pp. 375–378, 1997. DOI: 10.1103/PhysRevLett.79.375.

[41] D. M. Rossi, K. Minamisono, H. B. Asberry, G. Bollen, B. A. Brown, K. Cooper, B. Isherwood, P. F. Mantica, A. Miller, D. J. Morrissey, R. Ringle, J. A. Rodriguez, C. A. Ryder, A. Smith, R. Strum, and C. Sumithrarachchi, "Charge radii of neutron-deficient $^{36}\mathrm{K}$ and $^{37}\mathrm{K}$", *Physical Review C*, vol. 92, 2015. DOI: 10.1103/PhysRevC.92.014305.

[42] L. Vermeeren, P. Lievens, R. E. Silverans, U. Georg, M. Keim, A. Klein, R. Neugart, M. Neuroth, F. Buchinger, and t. I. Collaboration, "The mean square nuclear charge radius of $^{39}\mathrm{Ca}$", *Journal of Physics G*, vol. 22, pp. 1517–1520, 1996. DOI: 10.1088/0954-3899/22/10/014.

[43] A. J. Miller, K. Minamisono, A. Klose, D. Garand, C. Kujawa, J. D. Lantis, Y. Liu, B. Maaß, P. F. Mantica, W. Nazarewicz, W. Nörtershäuser, S. V. Pineda, P.-G. Reinhard, D. M. Rossi, F. Sommer, C. Sumithrarachchi, A. Teigelhöfer, and J. Watkins, "Proton superfluidity and charge radii in proton-rich calcium isotopes", *Nature Physics*, vol. 15, pp. 432–436, 2019. DOI: 10.1038/s41567-019-0416-9.

[44] K. Blaum, W. Geithner, J. Lassen, P. Lievens, K. Marinova, and R. Neugart, "Nuclear moments and charge radii of argon isotopes between the neutron-shell closures $N = 20$ and $N = 28$", *Nuclear Physics A*, vol. 799, pp. 30–45, 2008. DOI: 10.1016/j.nuclphysa.2007.11.004.

[45] W. H. King, "Comments on the Article "Peculiarities of the Isotope Shift in the Samarium Spectrum"", *Journal of the Optical Society of America*, vol. 53, p. 638, 1963. DOI: 10.1364/JOSA.53.000638.

[46] Y. P. Gangrsky, K. P. Marinova, and S. G. Zemlyanoi, "J dependences of the isotope shifts in Ti I $3d^2 4s^2\, a\,^3P$ and $3d^3 4p\, y\,^3D^o$ terms", *Journal of Physics B*, vol. 28, pp. 957–964, 1995. DOI: 10.1088/0953-4075/28/6/011.

[47] Y. P. Gangrsky, K. P. Marinova, S. G. Zemlyanoi, I. D. Moore, J. Billowes, P. Campbell, K. T. Flanagan, D. H. Forest, J. A. R. Griffith, J. Huikari, R. Moore, A. Nieminen, H. Thayer, G. Tungate, and J. Äystö, "Nuclear charge radii of neutron deficient titanium isotopes ^{44}Ti and ^{45}Ti", *Journal of Physics G*, vol. 30, pp. 1089–1098, 2004. DOI: 10.1088/0954-3899/30/9/009.

[48] F. Wienholtz, D. Beck, K. Blaum, C. Borgmann, M. Breitenfeldt, R. B. Cakirli, S. George, F. Herfurth, J. D. Holt, M. Kowalska, S. Kreim, D. Lunney, V. Manea, J. Menéndez, D. Neidherr, M. Rosenbusch, L. Schweikhard, A. Schwenk, J. Simonis, J. Stanja, R. N. Wolf, and K. Zuber, "Masses of exotic calcium isotopes pin down nuclear forces", *Nature*, vol. 498, pp. 346–349, 2013. DOI: 10.1038/nature12226.

[49] D. Steppenbeck, S. Takeuchi, N. Aoi, P. Doornenbal, M. Matsushita, H. Wang, H. Baba, N. Fukuda, S. Go, M. Honma, J. Lee, K. Matsui, S. Michimasa, T. Motobayashi, D. Nishimura, T. Otsuka, H. Sakurai, Y. Shiga, P.-A. Söderström, T. Sumikama, H. Suzuki, R. Taniuchi, Y. Utsuno, J. J. Valiente-Dobón, and K. Yoneda, "Evidence for a new nuclear 'magic number' from the level structure of ^{54}Ca", *Nature*, vol. 502, pp. 207–210, 2013. DOI: 10.1038/nature12522.

[50] Á. Koszorús, X. F. Yang, W. G. Jiang, S. J. Novario, S. W. Bai, J. Billowes, C. L. Binnersley, M. L. Bissell, T. E. Cocolios, B. S. Cooper, R. P. de Groote, A. Ekström, K. T. Flanagan, C. Forssén, S. Franchoo, R. F. G. Ruiz, F. P. Gustafsson, G. Hagen, G. R. Jansen, A. Kanellakopoulos, M. Kortelainen, W. Nazarewicz, G. Neyens, T. Papenbrock, P.-G. Reinhard, C. M. Ricketts, B. K. Sahoo, A. R. Vernon, and S. G. Wilkins, "Charge radii of exotic potassium isotopes challenge nuclear theory and the magic character of $N = 32$", *Nature Physics*, vol. 17, pp. 439–443, 2021. DOI: 10.1038/s41567-020-01136-5.

[51] K.-R. Anton, S. L. Kaufman, W. Klempt, G. Moruzzi, R. Neugart, E.-W. Otten, and B. Schinzler, "Collinear laser spectroscopy on fast atomic beams", *Physical Review Letters*, vol. 40, pp. 642–645, 1978. DOI: 10.1103/PhysRevLett.40.642.

[52] E. W. Otten, “Nuclear Radii and Moments of Unstable Isotopes”, in *Treatise on Heavy Ion Science*, D. A. Bromley, Ed., Boston, MA: Springer US, 1989, ISBN: 978-1-4613-0713-6.

[53] B. Cheal and K. T. Flanagan, “Progress in laser spectroscopy at radioactive ion beam facilities”, *Journal of Physics G*, vol. 37, p. 113 101, 2010. DOI: 10.1088/0954-3899/37/11/113101.

[54] P. Müller, K. König, P. Imgram, J. Krämer, and W. Nörtershäuser, “Collinear laser spectroscopy of Ca^+: Solving the field-shift puzzle of the $4s\,^2S_{1/2} \rightarrow 4p\,^2P_{1/2,3/2}$ transitions”, *Physical Review Research*, vol. 2, 2020. DOI: 10.1103/PhysRevResearch.2.043351.

[55] K. König, “Laserbasierte Hochspannungsmetrologie mit ppm Genauigkeit”, Dissertation, TU Darmstadt, Darmstadt, 2018.

[56] A. Einstein, “Zur Elektrodynamik bewegter Körper”, *Annalen der Physik*, vol. 322, pp. 891–921, 1905. DOI: 10.1002/andp.19053221004.

[57] W. Demtröder, *Laserspektroskopie 1: Grundlagen*. Berlin/Heidelberg: Springer Berlin Heidelberg, 2011, ISBN: 9783642213052.

[58] W. D. Phillips, “Nobel Lecture: Laser cooling and trapping of neutral atoms”, *Reviews of Modern Physics*, vol. 70, pp. 721–741, 1998. DOI: 10.1103/RevModPhys.70.721.

[59] M. Block, “Direct mass measurements of the heaviest elements with Penning traps”, *International Journal of Mass Spectrometry*, vol. 349-350, pp. 94–101, 2013. DOI: 10.1016/j.ijms.2013.02.013.

[60] C. Tamm, D. Engelke, and V. Bühner, “Spectroscopy of the electric-quadrupole transition $^2S_{1/2}(F = 0) \rightarrow {}^2D_{3/2}(F = 2)$ in trapped $^{171}Yb^+$”, *Physical Review A*, vol. 61, 2000. DOI: 10.1103/PhysRevA.61.053405.

[61] R. Neugart, D. L. Balabanski, K. Blaum, D. Borremans, P. Himpe, M. Kowalska, P. Lievens, S. Mallion, G. Neyens, N. Vermeulen, and D. T. Yordanov, “Precision measurement of ^{11}Li moments: influence of halo neutrons on the ^{9}Li core”, *Physical*

Review Letters, vol. 101, p. 132 502, 2008. DOI: 10.1103/PhysRevLett.101.132502.

[62] A. Coc, C. Thibault, F. Touchard, H. T. Duong, P. Juncar, S. Liberman, J. Pinard, J. Lermé, J. L. Vialle, S. Büttgenbach, A. C. Mueller, and A. Pesnelle, "Hyperfine structures and isotope shifts of $^{207-213,220-228}$Fr; Possible evidence of octupolar deformation", *Physics Letters B*, vol. 163, pp. 66–70, 1985. DOI: 10.1016/0370-2693(85)90193-5.

[63] W. Demtröder, *Laserspektroskopie 2: Experimentelle Techniken*, 6. neu bearb. und aktualisierte Aufl. Berlin and Heidelberg: Springer, 2013, ISBN: 9783642214479. DOI: 10.1007/978-3-642-21447-9.

[64] B. Maaß, K. König, J. Krämer, A. J. Miller, K. Minamisono, W. Nörtershäuser, and F. Sommer, *A 4 Fluorescence Detection Region for Collinear Laser Spectroscopy*.

[65] S. Kaufmann, "Laser spectroscopy of nickel isotopes with a new data acquisition system at ISOLDE", Dissertation, TU Darmstadt, Darmstadt, 2019.

[66] W. Nörtershäuser and C. Geppert, "Nuclear Charge Radii of Light Elements and Recent Developments in Collinear Laser Spectroscopy", in *The Euroschool on Exotic Beams, Vol. IV*, ser. Lecture Notes in Physics, C. Scheidenberger and M. Pfützner, Eds., vol. 879, Berlin, Heidelberg: Springer Berlin Heidelberg, 2014, pp. 233–292, ISBN: 978-3-642-45140-9. DOI: 10.1007/978-3-642-45141-6_6.

[67] W. H. King, *Isotope Shifts in Atomic Spectra*, ser. Physics of Atoms and Molecules. Boston, MA and s.l.: Springer US, 1984, ISBN: 1489917888. DOI: 10.1007/978-1-4899-1786-7.

[68] M. Wang, G. Audi, F. G. Kondev, W. J. Huang, S. Naimi, and X. Xu, "The AME2016 atomic mass evaluation (II). Tables, graphs and references", *Chinese Physics C*, vol. 41, p. 030 003, 2017. DOI: 10.1088/1674-1137/41/3/030003.

[69] M. Hammen, W. Nörtershäuser, D. L. Balabanski, M. L. Bissell, K. Blaum, I. Budinčević, B. Cheal, K. T. Flanagan, N. Frömmgen, G. Georgiev, C. Geppert, M. Kowalska, K. Kreim, A. Krieger, W. Nazarewicz, R. Neugart, G. Neyens, J. Papuga, P.-G. Reinhard, M. M. Rajabali, S. Schmidt, and D. T. Yordanov, "From

Calcium to Cadmium: Testing the Pairing Functional through Charge Radii Measurements of $^{100-130}$Cd", *Physical Review Letters*, vol. 121, p. 102 501, 2018. DOI: 10.1103/PhysRevLett.121.102501.

[70] J. C. Berengut, C. Delaunay, A. Geddes, and Y. Soreq, "Generalized King linearity and new physics searches with isotope shifts", *Physical Review Research*, vol. 2, 2020. DOI: 10.1103/PhysRevResearch.2.043444.

[71] C. Shi, F. Gebert, C. Gorges, S. Kaufmann, W. Nörtershäuser, B. K. Sahoo, A. Surzhykov, V. A. Yerokhin, J. C. Berengut, F. Wolf, J. C. Heip, and P. O. Schmidt, "Unexpectedly large difference of the electron density at the nucleus in the $4p\,^2\mathrm{P}_{1/2,3/2}$ fine-structure doublet of Ca^+", *Applied Physics B*, vol. 123, p. 507, 2017. DOI: 10.1007/s00340-016-6572-z.

[72] W. Demtröder, *Atome, Moleküle und Festkörper*, 5., neu bearbeitete und aktualisierte Auflage, ser. Springer-Lehrbuch. Berlin and Heidelberg: Springer Spektrum, 2016, vol. / Wolfgang Demtröder ; 3, ISBN: 978-3-662-49094-5.

[73] N. J. Stone, "Table of nuclear magnetic dipole and electric quadrupole moments", *Atomic Data and Nuclear Data Tables*, vol. 90, pp. 75–176, 2005. DOI: 10.1016/j.adt.2005.04.001.

[74] R. Neugart and G. Neyens, "Nuclear Moments", in *The Euroschool Lectures on Physics with Exotic Beams, Vol. II*, ser. Lecture Notes in Physics, J. Al-Khalili and E. Roeckl, Eds., vol. 700, Springer Berlin Heidelberg, 2006, pp. 135–189, ISBN: 978-3-540-33786-7. DOI: 10.1007/3-540-33787-3{\textunderscore}4.

[75] K. J. R. Rosman and P. D. P. Taylor, "Isotopic Compositions of the Elements 1997", *Journal of Physical and Chemical Reference Data*, vol. 27, pp. 1275–1287, 1998. DOI: 10.1063/1.556031.

[76] G. Fricke and Heilig, *Numerical data and functional relationships in science and technology: New series*, [Elektronische Ressource]. Berlin: Springer, 2004, ISBN: 978-3-540-42829-9.

[77] E. M. Burbidge, G. R. Burbidge, W. A. Fowler, and F. Hoyle, "Synthesis of the Elements in Stars", *Reviews of Modern Physics*, vol. 29, pp. 547–650, 1957. DOI: 10.1103/RevModPhys.29.547.

[78] A. V. Rode, K. Baldwin, A. Wain, N. R. Madsen, D. Freeman, P. Delaporte, and B. Luther-Davies, "Ultrafast laser ablation for restoration of heritage objects", *Applied Surface Science*, vol. 254, pp. 3137–3146, 2008. DOI: 10.1016/j.apsusc.2007.10.106.

[79] C. W. Schneider and T. Lippert, "Laser Ablation and Thin Film Deposition", in *Laser Processing of Materials: Fundamentals, Applications and Developments*, P. Schaaf, Ed., Berlin, Heidelberg: Springer Berlin Heidelberg, 2010, pp. 89–112, ISBN: 978-3-642-13281-0. DOI: 10.1007/978-3-642-13281-0{\textunderscore}5.

[80] S. Amoruso, R. Bruzzese, N. Spinelli, and R. Velotta, "Characterization of laser-ablation plasmas", *Journal of Physics B*, vol. 32, R131–R172, 1999. DOI: 10.1088/0953-4075/32/14/201.

[81] K.-H. Leitz, B. Redlingshöfer, Y. Reg, A. Otto, and M. Schmidt, "Metal Ablation with Short and Ultrashort Laser Pulses", *Physics Procedia*, vol. 12, pp. 230–238, 2011. DOI: 10.1016/j.phpro.2011.03.128.

[82] J. H. Yoo, O. V. Borisov, X. Mao, and R. E. Russo, "Existence of phase explosion during laser ablation and its effects on inductively coupled plasma-mass spectroscopy", *Analytical chemistry*, vol. 73, pp. 2288–2293, 2001. DOI: 10.1021/ac001333h.

[83] Z. Zhang, P. A. VanRompay, J. A. Nees, and P. P. Pronko, "Multi-diagnostic comparison of femtosecond and nanosecond pulsed laser plasmas", *Journal of Applied Physics*, vol. 92, pp. 2867–2874, 2002. DOI: 10.1063/1.1497449.

[84] T. Moscicki, J. Hoffman, and Z. SzymaDski, "Modelling of plasma formation during nanosecond laser ablation", *Archives of Mechanics*, vol. 63, pp. 99–116, 2011.

[85] A. Chen, Y. Jiang, T. Wang, J. Shao, and M. Jin, "Comparison of plasma temperature and electron density on nanosecond laser ablation of Cu and nano-Cu", *Physics of Plasmas*, vol. 22, p. 033 301, 2015. DOI: 10.1063/1.4913987.

[86] H. Dachraoui, W. Husinsky, and G. Betz, "Ultra-short laser ablation of metals and semiconductors: evidence of ultra-fast Coulomb explosion", *Applied Physics A*, vol. 83, pp. 333–336, 2006. DOI: 10.1007/s00339-006-3499-y.

[87] R. Jordan, D. Cole, J. G. Lunney, K. Mackay, and D. Givord, "Pulsed laser ablation of copper", *Applied Surface Science*, vol. 86, pp. 24–28, 1995. DOI: 10.1016/0169-4332(94)00370-X.

[88] S. Amoruso, V. Berardi, R. Bruzzese, N. Spinelli, and X. Wang, "Kinetic energy distribution of ions in the laser ablation of copper targets", *Applied Surface Science*, vol. 127-129, pp. 953–958, 1998. DOI: 10.1016/S0169-4332(97)00772-1.

[89] S. Amoruso, A. Sambri, M. Vitiello, and X. Wang, "Propagation of LaMnO3 laser ablation plume in oxygen gas", *Applied Surface Science*, vol. 252, pp. 4712–4716, 2006. DOI: 10.1016/j.apsusc.2005.07.107.

[90] A. Bogaerts and Z. Chen, "Nanosecond laser ablation of Cu: modeling of the expansion in He background gas, and comparison with expansion in vacuum", *J. Anal. At. Spectrom.*, vol. 19, pp. 1169–1176, 2004. DOI: 10.1039/B402946A.

[91] O. Kaleja, B. Anđelić, K. Blaum, M. Block, P. Chhetri, C. Droese, C. Düllmann, M. Eibach, S. Eliseev, J. Even, S. Götz, F. Giacoppo, N. Kalantar-Nayestanaki, M. Laatiaoui, E. Minaya Ramirez, A. Mistry, T. Murböck, S. Raeder, L. Schweikhard, and P. G. Thirolf, "The performance of the cryogenic buffer-gas stopping cell of SHIPTRAP", *Nuclear Instruments and Methods in Physics Research Section B*, vol. 463, pp. 280–285, 2020. DOI: 10.1016/j.nimb.2019.05.009.

[92] C. Droese, S. Eliseev, K. Blaum, M. Block, F. Herfurth, M. Laatiaoui, F. Lautenschläger, E. Minaya Ramirez, L. Schweikhard, V. V. Simon, and P. G. Thirolf, "The cryogenic gas stopping cell of SHIPTRAP", *Nuclear Instruments and Methods in Physics Research Section B*, vol. 338, pp. 126–138, 2014. DOI: 10.1016/j.nimb.2014.08.004.

[93] J. Ärje, J. Äystö, H. Hyvönen, P. Taskinen, V. Koponen, J. Honkanen, K. Valli, A. Hautojärvi, and K. Vierinen, "The ion guide isotope separator on-line, IGISOL", *Nuclear Instruments and Methods in Physics Research Section A*, vol. 247, pp. 431–437, 1986. DOI: 10.1016/0168-9002(86)90404-3.

[94] J. Äystö, "Development and applications of the IGISOL technique", *Nuclear Physics A*, vol. 693, pp. 477–494, 2001. DOI: 10.1016/S0375-9474(01)00923-X.

[95] L. Wense, B. Seiferle, M. Laatiaoui, and P. G. Thirolf, "The extraction of $^{229}Th^{3+}$ from a buffer-gas stopping cell", *Nuclear Instruments and Methods in Physics Research Section B*, vol. 376, pp. 260–264, 2016. DOI: 10.1016/j.nimb.2015.12.049.

[96] A. Nieminen, P. Campbell, J. Billowes, D. H. Forest, J. A. R. Griffith, J. Huikari, A. Jokinen, I. D. Moore, R. Moore, G. Tungate, and J. Aystö, "On-line ion cooling and bunching for collinear laser spectroscopy", *Physical Review Letters*, vol. 88, p. 094 801, 2002. DOI: 10.1103/PhysRevLett.88.094801.

[97] H. Frånberg, P. Delahaye, J. Billowes, K. Blaum, R. Catherall, F. Duval, O. Gianfrancesco, T. Giles, A. Jokinen, M. Lindroos, D. Lunney, E. Mane, and I. Podadera, "Off-line commissioning of the ISOLDE cooler", *Nuclear Instruments and Methods in Physics Research Section B*, vol. 266, pp. 4502–4504, 2008. DOI: 10.1016/j.nimb.2008.05.097.

[98] F. Herfurth, J. Dilling, A. Kellerbauer, G. Bollen, S. Henry, H.-J. Kluge, E. Lamour, D. Lunney, R. Moore, C. Scheidenberger, S. Schwarz, G. Sikler, and J. Szerypo, "A linear radiofrequency ion trap for accumulation, bunching, and emittance improvement of radioactive ion beams", *Nuclear Instruments and Methods in Physics Research Section A*, vol. 469, pp. 254–275, 2001. DOI: 10.1016/S0168-9002(01)00168-1.

[99] F. Herfurth, "Segmented linear RFQ traps for nuclear physics", *Nuclear Instruments and Methods in Physics Research Section B*, vol. 204, pp. 587–591, 2003. DOI: 10.1016/S0168-583X(02)02135-3.

[100] B. R. Barquest, G. Bollen, P. F. Mantica, K. Minamisono, R. Ringle, S. Schwarz, and C. S. Sumithrarachchi, "RFQ beam cooler and buncher for collinear laser spectroscopy of rare isotopes", *Nuclear Instruments and Methods in Physics Research Section A*, vol. 866, pp. 18–28, 2017. DOI: 10.1016/j.nima.2017.05.036.

[101] private communication with Victor Varentsov 2020.

[102] V. Varentsov, “A New Approach to the Extraction System Design”, *ResearchGate*, 2001. DOI: 10.13140/RG.2.2.30119.55200.

[103] V. L. Varentsov and A. A. Ignatiev, “Numerical investigations of internal supersonic jet targets formation for storage rings”, *Nuclear Instruments and Methods in Physics Research Section A*, vol. 413, pp. 447–456, 1998. DOI: 10.1016/S0168-9002(98)00354-4.

[104] M. Allers, A. T. Kirk, and S. Zimmermann, “A simple centripetal force model for explaining the focusing effect of ion funnels”, *International Journal of Mass Spectrometry*, vol. 432, pp. 14–17, 2018. DOI: 10.1016/j.ijms.2018.07.002.

[105] K. Giles, S. D. Pringle, K. R. Worthington, D. Little, J. L. Wildgoose, and R. H. Bateman, “Applications of a travelling wave-based radio-frequency-only stacked ring ion guide”, *Rapid communications in mass spectrometry : RCM*, vol. 18, pp. 2401–2414, 2004. DOI: 10.1002/rcm.1641.

[106] A. V. Tolmachev, T. Kim, H. R. Udseth, R. D. Smith, T. H. Bailey, and J. H. Futrell, “Simulation-based optimization of the electrodynamic ion funnel for high sensitivity electrospray ionization mass spectrometry”, *International Journal of Mass Spectrometry*, vol. 203, pp. 31–47, 2000. DOI: 10.1016/S1387-3806(00)00265-7.

[107] J. S. Page, A. V. Tolmachev, K. Tang, and R. D. Smith, “Theoretical and experimental evaluation of the low m/z transmission of an electrodynamic ion funnel”, *Journal of the American Society for Mass Spectrometry*, vol. 17, pp. 586–592, 2006. DOI: 10.1016/j.jasms.2005.12.013.

[108] R. T. Kelly, A. V. Tolmachev, J. S. Page, K. Tang, and R. D. Smith, “The ion funnel: Theory, implementations, and applications”, *Mass spectrometry reviews*, vol. 29, pp. 294–312, 2010. DOI: 10.1002/mas.20232.

[109] Z. N. Chen, Ed., *Handbook of Antenna Technologies*. Singapore: Springer Singapore, 2014, ISBN: 978-981-4560-75-7. DOI: 10.1007/978-981-4560-75-7.

[110] K. König, J. Krämer, C. Geppert, P. Imgram, B. Maaß, T. Ratajczyk, and W. Nörtershäuser, "A new Collinear Apparatus for Laser Spectroscopy and Applied Science (COALA)", *The Review of scientific instruments*, vol. 91, p. 081 301, 2020.

[111] T. Lellinger, "Ion production by pulsed laser ablation in a helium atmosphere", Master-Thesis, TU Darmstadt, Darmstadt, 2019.

[112] T. Ratajczyk, P. Bollinger, T. Lellinger, V. Varentsov, and W. Nörtershäuser, "Towards a He-buffered laser ablation ion source for collinear laser spectroscopy", *Hyperfine Interactions*, vol. 241, p. 883, 2020. DOI: 10.1007/s10751-020-1698-0.

[113] L. Tunna, A. Kearns, W. O'Neill, and C. Sutcliffe, "Micromachining of copper using Nd:YAG laser radiation at 1064, 532, and 355 nm wavelengths", *Optics & Laser Technology*, vol. 33, pp. 135–143, 2001. DOI: 10.1016/S0030-3992(00)00126-2.

[114] H. Unbehauen, *Klassische Verfahren zur Analyse und Synthese linearer kontinuierlicher Regelsysteme, Fuzzy-Regelsysteme: Mit 25 Tabellen*, 15., überarb. und erw. Aufl., ser. Studium Automatisierungstechnik. Wiesbaden: Vieweg + Teubner, 2008, vol. / Heinz Unbehauen ; 1, ISBN: 9783834804976.

[115] K. König, P. Imgram, J. Krämer, B. Maaß, K. Mohr, T. Ratajczyk, F. Sommer, and W. Nörtershäuser, "On the performance of wavelength meters: Part 2—frequency-comb based characterization for more accurate absolute wavelength determinations", *Applied Physics B*, vol. 126, 2020. DOI: 10.1007/s00340-020-07433-4.

[116] Eite Tiesinga, Peter J. Mohr, David B. Newell, and Barry N. Taylo, *The 2018 CODATA Recommended Values of the Fundamental Physical Constants*, J. Baker, M. Douma, and S. Kotochigova, Ed., Gaithersburg, MD 20899, 2020.

[117] D. R. Lide, Ed., *CRC handbook of chemistry and physics: A ready-reference book of chemical and physical data*, 89th ed. 2008-2009. Boca Raton, Fla.: CRC Taylor & Francis, 2008, ISBN: 9781420066791.

[118] K. Wendt, S. A. Ahmad, F. Buchinger, A. C. Mueller, R. Neugart, and E.-W. Otten, "Relativistic J-dependence of the isotope shift in the $6s$-$6p$ doublet of Ba II", *The European Physical Journal A*, vol. 318, pp. 125–129, 1984. DOI: 10.1007/BF01413460.

[119] K. König, F. Sommer, J. Lantis, K. Minamisono, W. Nörtershäuser, S. Pineda, and R. Powel, "Isotope-shift measurements and King-fit analysis in nickel isotopes", *Physical Review C*, vol. 103, 2021. DOI: 10.1103/PhysRevC.103.054305.

[120] F. Gebert, Y. Wan, F. Wolf, C. N. Angstmann, J. C. Berengut, and P. O. Schmidt, "Precision Isotope Shift Measurements in Calcium Ions Using Quantum Logic Detection Schemes", *Physical Review Letters*, vol. 115, p. 053 003, 2015. DOI: 10.1103/PhysRevLett.115.053003.

[121] H. D. Wohlfahrt, E. B. Shera, M. V. Hoehn, Y. Yamazaki, and R. M. Steffen, "Nuclear charge distributions in $1f_{7/2}$-shell nuclei from muonic x-ray measurements", *Physical Review C*, vol. 23, pp. 533–548, 1981. DOI: 10.1103/PhysRevC.23.533.

[122] M. Aldenius, S. Johansson, and M. T. Murphy, "Accurate laboratory ultraviolet wavelengths for quasar absorption-line constraints on varying fundamental constants", *Monthly Notices of the Royal Astronomical Society*, vol. 370, pp. 444–452, 2006. DOI: 10.1111/j.1365-2966.2006.10491.x.

[123] G. Nave, "Wavelengths of Fe II lines for studies of time variation of the fine-structure constant", *Monthly Notices of the Royal Astronomical Society*, vol. 420, pp. 1570–1574, 2012. DOI: 10.1111/j.1365-2966.2011.20143.x.

[124] E. B. Saloman, "Energy Levels and Observed Spectral Lines of Neutral and Singly Ionized Titanium, Ti I and Ti II", *Journal of Physical and Chemical Reference Data*, vol. 41, pp. 013101-013101–116, 2012. DOI: 10.1063/1.3656882.

[125] S. Huldt, S. Johansson, U. Litzén, and J.-F. Wyart, "The Spectrum and Term System of Singly Ionized Titanium, Ti II", *Physica Scripta*, vol. 25, pp. 401–412, 1982. DOI: 10.1088/0031-8949/25/2/025.

[126] D. C. Morton, "Atomic Data for Resonance Absorption Lines. III. Wavelengths Longward of the Lyman Limit for the Elements Hydrogen to Gallium", *The Astrophysical Journal Supplement Series*, vol. 149, pp. 205–238, 2003. DOI: 10.1086/377639.

[127] I. Zapadlik, S. Johansson, and U. Litzen, "Improved Wavelengths and Extended Analysis in Ti II", *Laboratory and Astronomical High Resolution Spectra*, vol. 81, pp. 237–238, 1995.

[128] M. Aldenius, "Laboratory wavelengths for cosmological constraints on varying fundamental constants", *Physica Scripta*, vol. T134, p. 014 008, 2009. DOI: 10.1088/0031-8949/2009/T134/014008.

[129] P. Imgram, K. König, J. Krämer, T. Ratajczyk, B. Maaß, P. Müller, F. Sommer, and W. Nörtershäuser, "High-precision collinear laser spectroscopy at the Collinear Apparatus for Laser Spectroscopy and Applied Physics (COALA)", *Hyperfine Interactions*, vol. 241, 2020. DOI: 10.1007/s10751-019-1690-8.

[130] A. Kanellakopoulos, X. F. Yang, M. L. Bissell, M. L. Reitsma, S. W. Bai, J. Billowes, K. Blaum, A. Borschevsky, B. Cheal, C. S. Devlin, R. F. Garcia Ruiz, H. Heylen, S. Kaufmann, K. König, Á. Koszorús, S. Lechner, S. Malbrunot-Ettenauer, R. Neugart, G. Neyens, W. Nörtershäuser, T. Ratajczyk, L. V. Rodríguez, S. Sels, S. J. Wang, L. Xie, Z. Y. Xu, and D. T. Yordanov, "Nuclear moments of germanium isotopes near $N = 40$", *Physical Review C*, vol. 102, 2020. DOI: 10.1103/PhysRevC.102.054331.

[131] K. König, J. Krämer, P. Imgram, B. Maaß, W. Nörtershäuser, and T. Ratajczyk, "Transition frequencies and hyperfine structure in $^{113,115}In^{+}$: Application of a liquid-metal ion source for collinear laser spectroscopy", *Physical Review A*, vol. 102, 2020. DOI: 10.1103/PhysRevA.102.042802.

[132] K. Mohr, Z. Andelkovic, A. Wekesa Barasa, A. Bußß, V. Hannen, W. Nörtershäuser, T. Ratajczyk, and R. Sánchez, "Towards laser spectroscopy of $^{24}Mg^{+}$ ions at CRYRING@ESR", *X-Ray Spectrometry*, vol. 49, pp. 169–172, 2020. DOI: 10.1002/xrs.3082.

[133] A. Egl, I. Arapoglou, M. Höcker, K. König, T. Ratajczyk, T. Sailer, B. Tu, A. Weigel, K. Blaum, W. Nörtershäuser, and S. Sturm, "Application of the Continuous Stern-Gerlach Effect for Laser Spectroscopy of the $^{40}Ar^{13+}$ Fine Structure in a Penning Trap", *Physical Review Letters*, vol. 123, p. 123 001, 2019. DOI: 10.1103/PhysRevLett.123.123001.

[134] K. König, C. Geppert, J. Krämer, B. Maaß, E. W. Otten, T. Ratajczyk, and W. Nörtershäuser, "First high-voltage measurements using Ca^+ ions at the ALIVE experiment", *Hyperfine Interactions*, vol. 238, 2017.

Curriculum Vitae

Academic Education

PhD (Physics) at Technical University of Darmstadt *01/2017 – 07/2021*

- Thesis: "Isotope shift measurements in Ti^{+} transitions using laser-ablated and thermalized ions" under supervision of Prof. Dr. Wilfried Nörtershäuser
- Participation in collaborative measurement campaigns at international accelerator facilities including CERN (SUI) and GSI/FAIR (GER)
- Member of the Helmholtz Graduate School for Hadron and Ion Research

Master of Science (Physics), Technical University of Darmstadt *08/2014 – 10/2016*

- Thesis: "A Lasersystem for ALIVE and first High-Voltage Measurements" under supervision of Prof. Dr. Wilfried Nörtershäuser

Year Abroad, Lunds Universitet, Sweden *08/2013 – 06/2014*

Bachelor of Science (Physics), Technical University of Darmstadt *10/2009 – 08/2013*

- Thesis: "Temperature-depended spectroscopy of a Yb^{3+} – doped fiber" under supervision of Prof. Dr. Thomas Walther

School Education

Abitur at Edertalschule in Frankenberg (Eder) *Graduation in 06/2009*

List of Publications

2020

- T. Ratajczyk, P. Bollinger, T. Lellinger, V. Varentsov, and W. Nörtershäuser, "Towards a He-buffered laser ablation ion source for collinear laser spectroscopy", *Hyperfine Interactions*, vol. 241, p. 883, 2020. DOI: 10.1007/s10751-020-1698-0

- L. Renth, P. Imgram, J. Krämer, K. König, T. Lellinger, B. Maaß, P. Müller, T. Ratajczyk, and W. Nörtershäuser, "First experiments with a laser ablation source at the COALA setup", *Hyperfine Interactions*, vol. 241, 2020. DOI: 10.1007/s10751-020-01715-1

- P. Imgram, K. König, J. Krämer, T. Ratajczyk, B. Maaß, P. Müller, F. Sommer, and W. Nörtershäuser, "High-precision collinear laser spectroscopy at the Collinear Apparatus for Laser Spectroscopy and Applied Physics (COALA)", *Hyperfine Interactions*, vol. 241, 2020. DOI: 10.1007/s10751-019-1690-8

- A. Kanellakopoulos, X. F. Yang, M. L. Bissell, M. L. Reitsma, S. W. Bai, J. Billowes, K. Blaum, A. Borschevsky, B. Cheal, C. S. Devlin, R. F. Garcia Ruiz, H. Heylen, S. Kaufmann, K. König, Á. Koszorús, S. Lechner, S. Malbrunot-Ettenauer, R. Neugart, G. Neyens, W. Nörtershäuser, T. Ratajczyk, L. V. Rodríguez, S. Sels, S. J. Wang, L. Xie, Z. Y. Xu, and D. T. Yordanov, "Nuclear moments of germanium isotopes near $N = 40$", *Physical Review C*, vol. 102, 2020. DOI: 10.1103/PhysRevC.102.054331

- K. König, P. Imgram, J. Krämer, B. Maaß, K. Mohr, T. Ratajczyk, F. Sommer, and W. Nörtershäuser, "On the performance of wavelength meters: Part 2—frequency-comb based characterization for more accurate absolute wavelength determinations", *Applied Physics B*, vol. 126, 2020. DOI: 10.1007/s00340-020-07433-4

- K. König, J. Krämer, P. Imgram, B. Maaß, W. Nörtershäuser, and T. Ratajczyk, "Transition frequencies and hyperfine structure in ^{113,115}In^{+}: Application of a liquid-metal ion source for collinear laser spectroscopy", *Physical Review A*, vol. 102, 2020. DOI: 10.1103/PhysRevA.102.042802

- K. König, J. Krämer, C. Geppert, P. Imgram, B. Maaß, T. Ratajczyk, and W. Nörtershäuser, "A new Collinear Apparatus for Laser Spectroscopy and Applied Science (COALA)", *The Review of scientific instruments*, vol. 91, p. 081 301, 2020

- K. Mohr, Z. Andelkovic, A. Wekesa Barasa, A. Buß, V. Hannen, W. Nörtershäuser, T. Ratajczyk, and R. Sánchez, "Towards laser spectroscopy of ^{24}Mg^{+} ions at CRYRING@ESR", *X-Ray Spectrometry*, vol. 49, pp. 169–172, 2020. DOI: 10.1002/xrs.3082

2019

- A. Egl, I. Arapoglou, M. Höcker, K. König, T. Ratajczyk, T. Sailer, B. Tu, A. Weigel, K. Blaum, W. Nörtershäuser, and S. Sturm, "Application of the Continuous Stern-Gerlach Effect for Laser Spectroscopy of the ^{40}Ar^{13+} Fine Structure in a Penning Trap", *Physical Review Letters*, vol. 123, p. 123 001, 2019. DOI: 10.1103/PhysRevLett.123.123001

- P. Imgram, K. König, J. Krämer, T. Ratajczyk, R. A. Müller, A. Surzhykov, and W. Nörtershäuser, "Collinear laser spectroscopy at ion-trap accuracy: Transition frequencies and isotope shifts in the $6s\,^2\mathrm{S}_{1/2} \rightarrow 6p\,^2\mathrm{P}_{1/2,3/2}$ transitions in Ba^{+}", *Physical Review A*, vol. 99, 2019. DOI: 10.1103/PhysRevA.99.012511

2018

- J. Krämer, K. König, C. Geppert, P. Imgram, B. Maaß, J. Meisner, E. W. Otten, S. Passon, T. Ratajczyk, J. Ullmann, and W. Nörtershäuser, "High-voltage measurements on the 5 ppm relative uncertainty level with collinear laser spectroscopy", *Metrologia*, vol. 55, pp. 268–274, 2018. DOI: 10.1088/1681-7575/aaabe0

2017

- K. König, C. Geppert, J. Krämer, B. Maaß, E. W. Otten, T. Ratajczyk, and W. Nörtershäuser, "First high-voltage measurements using Ca^+ ions at the ALIVE experiment", *Hyperfine Interactions*, vol. 238, 2017

Acknowledgement

The path to this thesis was leading through many different phases with nice and frustrating times and the finish fell in the special time of the pandemic. I would not have made it to the end of this path if there would not have been people supporting me, whom I owe a deep debt of gratitude.

First I have to thank Wilfred Nörtershäuser for taking me in his team and supporting me during this time. He always provided me the possibility to keep the project running and also gave me many opportunities to visit international facilities and conferences.

I also want to thank Prof. Dr. Joachim Enders for supporting me as second reviewer and Prof. Dr. Reinhold Walser and Prof. Dr. Thomas Walther for participating in my thesis defence.

The idea for the ion-funnel source and the preceding simulations came from Prof. Dr. Victor Varentsov and I want to thank him for his support and providing the simulation graphics for this thesis.

During my PhD I had a lot of support in the lab by the TIMS group and I thank Philipp and Tim for all the persistent help and the creative solutions for the numerous challenges.

A very special thanks goes also to the best office which consisted of three of my best friends Kristian, Bernhard and Felix, who I know since the beginning of my study time in Darmstadt and who besides all the tremendous support they gave me throughout this thesis also made the time really special.

The whole lasersphere group was always there to support and help out and even during lockdown and homeoffice I could always count on your help and advice, which I am very grateful for.

Offsite the university I have a very close group of friends, that is actually also very involved in physics as I met most of them during my study time. But it was always a pleasure to spend time with you in the evenings, on bike tours and all the other activities. Thanks for also supporting me in more complicated times.

A special thanks goes to my family who was always there for me in any situation an helped me trough the hardest times. It was always a pleasure to visit Ratabecks in Wiesenfeld and gain new energy and also release stress outside, often with my neighbour and corona buddy Verena. It was also always a treat to spend time with my dad either in Darmstadt or Limburg and to have some long discussions.